

SURFACE MICROMACHINED TUNABLE
OPTOELECTRONIC DEVICES

A DISSERTATION
SUBMITTED TO THE DEPARTMENT OF ELECTRICAL ENGINEERING
AND THE COMMITTEE ON GRADUATE STUDIES
OF STANFORD UNIVERSITY
IN PARTIAL FULFILLMENT OF THE REQUIREMENTS
FOR THE DEGREE OF
DOCTOR OF PHILOSOPHY

Chien-chung Lin

June 2002

©Copyright by Chien-chung Lin 2002
All Rights Reserved

I certify that I have read this dissertation and that in my opinion it is fully adequate, in scope and quality, as a dissertation for the degree of Doctor of Philosophy.

Prof. James S. Harris, Jr. (Principal Advisor)

I certify that I have read this dissertation and that in my opinion it is fully adequate, in scope and quality, as a dissertation for the degree of Doctor of Philosophy.

Prof. David A. B. Miller

I certify that I have read this dissertation and that in my opinion it is fully adequate, in scope and quality, as a dissertation for the degree of Doctor of Philosophy.

Prof. Olav Solgaard

Approved for the University Committee on Graduate Studies:

Abstract

In recent years there has been an explosion in data traffic due to the prevailing Internet. A technique called wavelength division multiplexing (WDM) promises to accommodate the increased traffic without replacing the existing fiber networks. Wavelength sensitive devices such as tunable filters, detectors, and lasers are key components in the WDM system. Surface micromachining is one of the most promising technologies to fabricate such devices.

A typical surface micromachined wavelength-tunable device was demonstrated by integrating a deformable membrane of dielectric mirror stack to optoelectronic devices. These devices have been applied to different fields such as communications, parameter extraction, etc. As the number of WDM channels increases, these devices have to contend with narrower channel linewidths. This is especially important for the passive devices where the linewidth is determined largely by the cavity finesse. However, the previously developed dielectric top mirror stack has both complicated fabrication and low reflectivity problems. To achieve this, a novel top mirror with high reflectivity and wide bandwidth is desired. The process of this new type of mirror must be easy enough to integrate into the generic optoelectronic devices process flow. Another important issue is how to lower the tuning voltage of devices. In this work, we focus on building a tunable optoelectronic filter with low actuation voltage, narrow linewidth, and wide tuning range.

To design an optimal structure, I establish an opto-mechanical model which can evaluate the micromachined structure easily and accurately. Through this model, we can quantify the optical diffraction loss caused by the curved surface and thus facilitate the design of high finesse tunable filters. A comprehensive mechanical method, called the “area moment method,” is used to provide an accurate surface profile of the mirror under actuation. This profile is then input into to a second-order perturbation model to estimate optical loss. The linewidth broadening effect can be directly obtained from the loss.

From the above analysis, a less stiff top movable structure is accomplished using $\text{Al}_2\text{O}_3/\text{GaAs}$ as the distributed Bragg reflector material. A tunable optical filter is grown, processed and measured. Its surface profile matches our mechanical analysis and it demonstrates 64 nm tuning range under a 12-volt swing. The tuning characteristics of this device can also be changed by additional silicon nitride etching. This new design of tunable devices will be attractive for future generation of optical communication systems.

Acknowledgement

When I started thinking about this paragraph, it really took me a while, because there are so many people I feel obliged to, and saying thank you in this article is just not enough. If I could say I came to Stanford with bare hands and leave with handful of friendship and technical experience, the first person I would like to thank is my advisor, Professor James Harris. Being his students for many years, I deeply feel I am the most fortunate graduate student on earth. He is always nice to people and very willing to sit down with you to solve your problem. His broad knowledge and profound insight are always good guidance of my research. His relentless effort and persistence on scientific innovation always encourage me during the hard time of my research. He gives students the freedom to establish their own direction and helps them become self-motivated. Through these years, I truly believe this is the best way to promote myself to a new level of learning. Besides hard working, Professor Harris also wants us to enjoy life. From skiing in Lake Tahoe to traveling in China, he has endless fun experience to open your eyes. I would say every time I talked to him, I learn a lot from him in every aspect.

Also I would like to thank Prof. Miller and Prof. Solgaard to be my reading committee members. Both of them have expertise in optoelectronic devices and micromachining technology that are very crucial to the success of this project. Most important of all, they are both very friendly to students and discussing problems with them becomes pleasant experience and benefits me a lot.

My graduate life started with a lot of things to learn, and I am lucky that former students from Harris group helped me to go through them. Chris Ebert and Chris Coldren taught me how to maintain the MBE system. Fred Sugihwo showed me how to grow a laser device and led me into the world of tunable devices. Wayne Martin solved a lot of computer and processing problems for me. During my research, Thierry Pinguet helped me with the MBE machine opening and also the solid-state laser setups. Numerous people in Harris group contributed so many in my project and I am really appreciated

their help. In addition to these works, we hang out together for beers, BBQ, and movies. I would say my fellow students in Harris group are the best! Vijit, Vincent, Xian, Mark, Wonill, Rafael Xiaojun, Evan, Junxian, Kai, thank you all!

Other friends from Ginzton lab also give me a lot of help during my long research struggle. Krishnan Parameswaran and Ming-Hsien Chou have a lot of experience in optics and I can often get my solution in aligning my measurement setups from them. Loren Eyres has always been a good source for advice and very helpful. Micah Yairi, Helen Kung, and Gordon Keeler from Miller group also provide a lot of help through exciting discussion. Technical staffs from CIS clean room play important roles to maintain process equipments ready for me. Without their efforts, none of my devices can be made.

My friends in Stanford make my days more interesting. We hang out during the weekend and have trips around the country. My special thanks to Chien-Mo, Yi-Chang, Li-Yi, Feng-Gang, Roy, Chun-Yi, Chih-Chien and Sheng-Chung. Because of them, any depression in the research can be conquered and my life in Stanford really becomes enjoyable.

Personally, I would like to thank my parents and my family. They are always my strongest support and always open their arms to greet me. Although they are in Taiwan and far apart from here, their cares come cross the ocean and never stop. Without them, I might give up long time ago.

Finally, I would like to thank our secretaries. Gail Chun-Creech, Lu Miao and Ingrid Tarien are the best secretaries I have ever seen. They deal with administrative work to make the system moving. This is a great help for graduate students. Without them, I could not accomplish so far.

Table of Contents

<u>Chapter 1 Introduction</u>	1
<u>1.1 Data transmission demand on Internet</u>	1
<u>1.2 Wavelength division multiplexing and optoelectronic devices</u>	1
<u>1.3 Surface micromachining for tunable devices</u>	2
<u>1.4 Organization</u>	3
<u>Chapter 2 Background</u>	5
<u>2.1 Introduction</u>	5
<u>2.2 Requirements for tunable filters in WDM systems</u>	5
<u>2.3 Fabry-Perot vertical cavity tunable filter</u>	6
<u>2.4 Acousto-optic tunable filter</u>	7
<u>2.5 Electro-optic tunable filter</u>	10
<u>2.6 Mach-zehnder tunable filter</u>	11
<u>2.7 Comparison and summary</u>	12
<u>Chapter 3. Mechanical analysis of the deformable membrane</u>	15
<u>3.1 Introduction</u>	15
<u>3.2 Electrostatic Attraction Force and One Dimensional Model</u>	16
<u>3.3 Top Structure Design – Plate Theory</u>	19
<u>3.3.1 Pure bending of plates</u>	19
<u>3.3.2 Symmetrical deflection of circular plates</u>	21
<u>3.3.3 Deflection of plate with non-uniform thickness</u>	24
<u>3.4 Different Top Membrane Designs</u>	25
<u>3.5 Surface deformation profile calculation</u>	28
<u>3.5.1 Mechanical analysis of deformable membrane profile under external load</u>	28
<u>3.5.2 Finite Element Analysis</u>	29
<u>3.5.3 Static Differential Equations</u>	30

<u>3.5.4 Area Moment Method and Conjugate Beams</u>	32
<u>3.5.5 Beams With Fixed End and Various Cross Section</u>	35
<u>3.5.6 Comparison of the two top plate design cases</u>	38
<u>3.5.7 Comparison of the finite element analysis and the area moment method</u>	40
<u>3.6 Summary</u>	41
<u>Chapter 4. Optical analysis of tunable optoelectronic devices</u>	42
<u>4.1 Introduction</u>	42
<u>4.2 Plane wave modeling of multiple layer structure</u>	44
<u>4.3 Application of scattering matrix to multiple semiconductor layers</u>	47
<u>4.4 Refractive index model of Al_xGa_{1-x}As system</u>	51
<u>4.5 The two-dimensional cavity analysis</u>	52
<u>4.5.1 Optical Field Distribution – The Fox-Li Model</u>	53
<u>4.5.2 Modes in an open resonator with high Fresnel number</u>	56
<u>4.5.3 Optical Diffraction Loss from Second Order Perturbation Theory</u>	57
<u>4.6 Comparison with Experimental Results</u>	60
<u>4.7 Summary</u>	61
<u>Chapter 5 Material growth and fabrication of tunable optoelectronic devices</u>	63
<u>5.1 Introduction</u>	63
<u>5.2 Material growth</u>	63
<u>5.3 In-Situ Growth Calibration</u>	67
<u>5.4 Device fabrication</u>	70
<u>Chapter 6 Surface Micromachined Wavelength Tunable Optoelectronic Devices</u>	72
<u>6.1 Introduction</u>	72
<u>6.2 Dielectric top mirror tunable devices</u>	73
<u>6.2.1 Tunable VCSEL and parameter extraction</u>	74
<u>6.2.2 Tunable PIN photodiode</u>	77
<u>6.2.3 Parameter extraction of phototransistor</u>	79

<u>6.2.4 Tunable phototransistor</u>	85
<u>6.3 Oxide top mirror tunable devices</u>	86
<u>6.3.1 Wavelength tunable filter using Al₂O₃/GaAs DBR as top mirror</u>	87
<u>6.3.2 Mechanical Measurement</u>	88
<u>6.3.3 Optical Measurement</u>	94
<u>6.3.4 Comparison between optical and mechanical measurement</u>	96
<u>6.3.5 Yield of the process</u>	97
<u>6.4 Summary</u>	98
<u>Chapter 7 Future work and summary</u>	99
<u>7.1 Future work</u>	99
<u>7.2 Summary</u>	101
<u>Appendix A Detailed Process Flow</u>	104
<u>Bibliography</u>	108

Lists of Tables

<u><i>Table 2.1: Comparison among the major tunable filter technologies.</i></u>	13
<u><i>Table. 3.1: Comparison of reflectivity between different material systems.</i></u>	18
<u><i>Table. 6.1: Comparison to other previous reports.</i></u>	97
<u><i>Table 6.2: The yield chart of the tunable filter with different top mirror shape.</i></u>	97

List of Illustrations

<u>Fig. 2.1: The modern design of the acousto-optic tunable filter [9]</u>	8
<u>Fig.2.2: The schematic diagram of the electro-optic tunable filter</u>	9
<u>Fig. 2.3: The tuning mechanism of the electro-optic filter. The solid curves are the two dispersion curves of the waveguides. The intersection point, λ_0, is the phase-matching wavelength. When the voltage is applied to the filter, the matching point will move to λ_v due to the electro-optic effect.</u>	10
<u>Fig. 2.4: The basic device layout of a Mach-Zehnder optical interferometer.</u>	11
<u>Fig. 2.5: Unbalanced Mach-Zehnder tunable filter. The central electrodes are the controller to change the refractive index of the waveguide material via electro-optic effect.</u>	12
<u>Fig. 2.6: The cascaded tunable Mach-Zehnder (MZ) filter for single channel transmission.</u>	13
<u>Fig. 3.1: Schematic diagram of the surface micromachined tunable devices.</u>	16
<u>Fig. 3-2: The theoretical fitting of the one-dimensional model.</u>	19
<u>Fig. 3.3: The illustration of the small bending of a generic plate.</u>	21
<u>Fig. 3.4: Symmetric bending of circular plates</u>	22
<u>Fig. 3.5: Top view of two different designs for movable top mirrors</u>	26
<u>Fig. 3.6: The calculated membrane deflection versus distance from the center of membrane.</u>	27
<u>Fig. 3.7: The calculated internal stress for both uniform plate and non-uniform plate. The insert is the membrane profile.</u>	27
<u>Fig. 3.8: 3-D visualization of the tunable membrane by MEMCAD</u>	29
<u>Fig. 3.9: The extracted 2-D cross section of the deformation profile of the tunable membrane shown in the previous figure.</u>	30
<u>Fig. 3.10: Cross section of the beam with external load. The σ_x denotes the internal stress caused by external load.</u>	31
<u>Fig. 3.11: Diagram of a simple-supported beam under a concentrated load: (a) illustration of the physical beam, and (b) bending moment diagram.</u>	32

<u>Fig. 3.12: Illustration of area moment method: (a) the beam AB of consideration (b) corresponding bending moment diagram.</u>	33
<u>Fig. 3.13: Schematic diagram of the reduced mechanical model.</u>	35
<u>Fig. 3.14: Modified bending moment diagram of bending moment and statically indeterminate coupling. The shaded region indicates the starting position of the central membrane.</u>	37
<u>Fig. 3.15: Calculated deformation under different electrical bias voltages.</u>	38
<u>Fig. 3.16: The two cases of the top membrane design : (i) the DBR is everywhere; (ii) the DBR is etched except over the central plate. In (i), the DBR is not removed from the supporting leg region.</u>	38
<u>Fig. 3.17: The calculated results of cases (a) and (b). It is obvious that case (b) has much less deformation in the central region (the shaded region).</u>	39
<u>Fig. 3.18: The calculated result of the finite element analysis software (MEMCAD 4.8) and the modified area moment method.</u>	40
<u>Fig. 4.1: A general scattering network with input ports, a_i and output ports b_i.</u>	43
<u>Fig. 4.2: Two scattering networks cascade to each other.</u>	45
<u>Fig. 4.3: Basic cases in the general multiple layers of optoelectronic devices. (a): interface between two materials. (b) transmission line in one material (c) combination of (a) and (b). (d) a Fabry-Perot etalon.</u>	47
<u>Fig.4.4: The reflection and transmission coefficient S_{11} and S_{12} versus phase variation. Different families of the curves corresponds to $r=0.3, 0.5, 0.9$, respectively.</u>	48
<u>Fig. 4.5: The measured and simulated spectrum of a 10 pairs AlAs/GaAs DBR. The results have been normalized.</u>	49
<u>Fig. 4.6: The simulated spectral response of a tunable filter with a 5 pairs Al_2O_3/GaAs DBR.</u>	50
<u>Fig. 4.7: Refractive index dispersion obtained from Gehrsitz et al. [32]. The solid line is the fitting curve from the theory.</u>	52
<u>Fig. 4.8: Illustration of basic conception of the Fox-Li model: (a) two semi-infinite plane mirrors with width a form a one-dimensional cavity. (b) the resonating phenomenon can be depicted as a series of optical apertures lining up with optical waves propagating through each aperture following the Huygen's principle.</u>	55

<u>Fig. 4.9: Optical field distribution using Fox-Li's model for calculation.</u>	56
<u>Fig. 4.10: The perturbed Fabry-Perot resonator with phase variation</u>	58
<u>Fig. 4.11: Single pass power loss versus applied tuning voltage. The loss is increasing towards the larger bending.</u>	59
<u>Fig. 4.12: Comparison between the theoretical calculation and experimental results of linewidth broadening of tunable phototransistors.</u>	61
<u>Fig. 5.1: Schematic Diagram of a MBE system.</u>	64
<u>Fig. 5.2: Illustration of surface chemistry of the MBE growth.</u>	65
<u>Fig. 5.3: The reflectivity of the multiple InGaAs quantum wells sample with GaAs barrier and background. The dip around 970nm is from the absorption peak of the quantum wells.</u>	68
<u>Fig. 5.4: The in-situ reflectivity plots of the tunable devices: (a) after 10 pairs of DBR grown; (b) after the main cavity grown; (c) fully finished wafer. The solid line is the calculation and dash line is the measurement.</u>	69
<u>Fig. 5.5: Simplified process flow of the tunable devices: (a) pattern the central membrane; (b) etch away the unwanted mirror material; (c) deposit the silicon nitride and partially etch the sacrificial AlGaAs layer for electrical contacts; (d) fully release of the membrane.</u>	70
<u>Fig. 5.6: The SEM micrograph of the successfully released tunable membrane: (a) the whole view of the tunable structure with four supporting legs and the central membrane; (b) the close-up view of the central membrane, the shadow underneath the membrane indicates the full release of the process.</u>	71
<u>Fig. 6.1: A generic surface micromachined tunable structure.</u>	73
<u>Fig. 6.2: The threshold current and external quantum efficiency versus the tuning wavelength.</u>	74
<u>Fig. 6.3: Inverse of external quantum efficiency vs. inverse of mirror loss.</u>	75
<u>Fig. 6.4: Logarithm of threshold current density vs. the normalized mirror loss.</u>	77
<u>Fig. 6.5: The photocurrent spectrum of tunable PIN diode under different tuning bias.</u>	78
<u>Fig. 6.6: Schematic diagram of a heterojunction phototransistor. The input photon and current components are also depicted. The shaded region is the quantum well absorbing region.</u>	80

<u>Fig. 6.7: The collector current vs. V_{CE} of a phototransistor.</u>	83
<u>Fig. 6.8: The measured and fitted AC and DC optical gain vs. J_C plot.</u>	84
<u>Fig. 6.9: The fitting curves with experimental results of other research group.</u>	84
<u>Fig. 6.10: The tuning spectral response of photocurrent of tunable HPT.</u>	86
<u>Fig. 6.11: The resonant wavelength vs. membrane tuning voltage of the tunable HPT.</u>	86
<u>Fig. 6.12: Schematic diagram of tunable filter with Al_2O_3/GaAs top mirror</u>	88
<u>Fig. 6.13: The comparison between the area moment method calculation and the mechanical deformation profile measurement.</u>	89
<u>Fig. 6.14: The one dimensional model and the measured displacement vs. tuning voltage.</u>	89
<u>Fig. 6.15: The effect of different size of DBR: (a) the uniform thickness in everywhere of the structure; (b) the central plate thicker than the leg due to DBR. The dimension of the supporting leg is 120 μm by 5 μm.</u>	90
<u>Fig. 6.16: The displacement vs. tuning voltage after different etching time of silicon nitride. The solid and dash lines are from one-dimensional theory.</u>	92
<u>Fig. 6.17: Measured spring constant versus etching time. The dash lines are the linear extrapolation of the data points. A downshift of the linear extrapolation shows possible nitride damage during the etch.</u>	92
<u>Fig. 6.18: The experimental setup of the optical measurement.</u>	93
<u>Fig. 6.19: The measured tuning spectrum of the 30 mm by 30 mm device for 10 minutes Si_3N_4 etching. Multiple peaks due to the backside reflection can be clearly observed. The last measurement (12V) possesses the largest linewidth because of the worse DBR reflectivity in that wavelength range.</u>	93
<u>Fig. 6.20: A detailed spectrum for a tunable filter. One can observe the periodicity of the multiple peaks.</u>	94
<u>Fig. 6.21: The tuning characteristics of the 20 μm by 20 μm device.</u>	96
<u>Fig. 6.22: The comparison between the optical and mechanical measurement results.</u>	96
<u>Fig. A-1: The process flow of the tunable devices: (a) After Central mask, the blow up is the SEM image (b) Deposit the silicon nitride and use MembraneL to pattern it (c) Use MembraneL to partially remove the $Al_{0.85}Ga_{0.15}As$ (d) Use Contact mask and evaporate metal for bottom contact (e) Final release of the device.</u>	107

Chapter 1 Introduction

1.1 DATA TRANSMISSION DEMAND ON INTERNET

During the past decade, the invention and explosion of the Internet has brought a tremendous impact on modern daily life. Similar to the telephone, the Internet makes the communication between people, broad expression of ideas and business much easier. The fast connection between the different continents is an intriguing opportunity for the entire global market. The copper twisted pair can provide a very convenient way to connect very short distances up to hundreds of MHz, but with the drive to 1 GHz and above, and the necessity of long connections losses and dispersion create severe problems. Once the speed requirement exceeds 10GHz, and distances exceed a number of meters optical fiber becomes the only practical choice.

The lightwave transmitted in optical fiber brings a new need for a different category of devices. These devices must sense and transfer electronic and photonic signals back and forth. These devices are called optoelectronic devices. These new devices are the key components in optical fiber transmission systems. The much broader bandwidth (or faster speed) that optical fiber provides has triggered a much larger growth in the Internet traffic. In addition to the original voice and text data, images and even animation data become more and more frequent. These types of data require an even faster transmission system and thus the need for continued expansion of bandwidth of data communication is always an issue for modern communication systems.

1.2 WAVELENGTH DIVISION MULTIPLEXING AND OPTOELECTRONIC DEVICES

To solve the increasing demand on data transmission bandwidth, there are several choices: one is called Time Division Multiplexing (TDM), and a second is called Wavelength Division Multiplexing (WDM). If we would like to boost the amount of data transmitted, the number of the channels has to be increased to accommodate this. The concepts of these two schemes are simple: in TDM, the speed or bandwidth of each

channel is increased, hence different channels lie in the time domain; while in WDM many more lower bandwidth channels are used with the different channels embedded in the frequency (wavelength) domain. One of the benefits of the WDM system is that it can utilize most of the optical system bandwidth without requiring very high data rates on individual channels. Due to its multiple wavelength nature, more available bandwidth can be occupied with modest channel bit rates. Also if we try to put in more data, we can either increase the number of channels accommodated or the data rate of each channel. Thus from a system's point of view, WDM is more flexible and agile. TDM is conceptually easier to implement because all it needs is high speed optoelectronic devices. However, if the number of channels or the total operating bandwidth has to be upgraded, the costs for the high-speed devices are relatively expensive and the channels have to be re-configured. The TDM system is thus more difficult to change.

From the comparison above, systems designers are usually more interested in WDM since system capacity can be expanded more easily than the TDM system. However, a difficulty for WDM systems is that devices operating at many different wavelengths are required. Most photodetectors are inherently and spectrally broadband devices. To make a filter or wavelength selective photodetector becomes a more important job for the full realization of WDM systems. One of the promising technologies is a resonant cavity enhanced (RCE) device whose active material (the absorbing region or quantum wells) is contained within a resonant cavity. This concept, combined with the vertical cavity structure, can provide a very good device for WDM applications.

1.3 SURFACE MICROMACHINING FOR TUNABLE DEVICES

Single fixed wavelength selective device is, however, not enough for the WDM system. Since each channel (or each wavelength) must be detected and generated, capability for tuning to different wavelengths is necessary for the device. Since only one wavelength is possible in a fixed RCE device, different fabrication or device structure design is necessary to implement each different wavelength. This greatly increases the production cost of the devices, requires a large inventory of different devices, and

decreases the manufacturing tolerances to achieve such uniform control of different wavelengths devices. These are not easy tasks, hence not commercially desirable. In the ideal case, it will be better to have devices that can easily vary their wavelength. A broadly tunable optoelectronic device can make the design and fabrication work simple because only one structure is necessary and many of the process issues can be controlled.

There have been many efforts to achieve this goal and several major technologies have been successfully applied to the devices. Here I would like to concentrate the discussion on a surface micromachined tunable approach because this technology is simple to realize and different research groups have shown a number of widely tunable optoelectronic devices based on this method.

Generally speaking, surface micromachining is one branch of the larger family of Micro Electromechanical Systems (MEMS) technology. The other counterpart is called bulk micromachining. Surface micromachining involves more processes on the surface of the wafer, including thin film deposition, dry-etching and sacrificial etching. Most of the optical components, like mirrors or lenses, are made of deposited material on the surface. Compared to bulk micromachining, which carves into the wafer to form the optical components, surface flatness is inferior in surface micromachining. However, surface micromachining is more versatile in terms of microstructure design and is easier to implement tunable device designs. The details of this will be discussed in the following chapters.

1.4 ORGANIZATION

The organization of this dissertation can be stated as follows: chapter 2 is a background study of the mechanisms used to make tunable optoelectronic devices, and specially focused on passive components. Chapter 3 focuses on the mechanical modeling of the structure design, I introduce a fast and reasonably accurate method to calculate the deformation of the microstructure during the electrostatic actuation. Chapter 4 describes optical modeling of the devices. The ordinary transmission matrix method will be reviewed and a more elaborate 2-D method based on Fox-Li's algorithm and second order perturbation theory of the cavity mode is introduced to calculate the optical

diffraction loss of the deformed mirror. The epitaxial material growth and fabrication processes are described in chapter 5. The experimental data for several micromachined tunable devices such as tunable VCSELs, phototransistors and filters are shown in chapter 6. Finally suggestions for future work on this devices and conclusion of this thesis are presented in chapter 7.

Chapter 2 Background

2.1 INTRODUCTION

In a general optical fiber network, there are two required components: transmitters and receivers. The transmitter is composed of light emitting units, such as light emitting diodes (LEDs) or lasers. They transform the electronic signals into a modulated light wave and couple this light wave into the fiber. At the receiver end, the photons will be transformed back to an electronic signal which is read out by high speed circuits. In the WDM scheme, however, more than one frequency must be generated and decoded, hence, a wavelength tunable device can be really helpful for such a system.

In the past, more efforts have been devoted to the active tunable devices such as tunable lasers, LEDs or detectors. However, according to market research, tunable passive devices will become far more important for network management. Thus more passive devices are needed in the systems than active devices. Some components, such as optical routers, optical add/drop multiplexers, wavelength conversion devices and optical cross-connects are purely passive. However, much less research has been focused on surface micromachined tunable passive devices because these network management issues were not as apparent as the wavelength tunability of the transmitters and receivers. In this chapter, I stress the basic concepts of tunable filters. Several major technologies that can be used to tune wavelength will be discussed in this chapter. Also from the background research, we identify a suitable solution for future WDM passive component structures.

2.2 REQUIREMENTS FOR TUNABLE FILTERS IN WDM SYSTEMS

Tunable filters are one of the key components in WDM systems. As mentioned previously, tunable filters serve several functions in devices and form a core technology. To satisfy the requirement of WDM system architectures, several conditions have to be met for these devices [1]: insertion loss, bandwidth, sidelobe suppression, dynamic range, tuning speed, control mechanism, size, mass-production possibility and low price. Some of these factors are subjective and there is no universal agreement on the requirement,

like the price and mass-production possibility. However, some of them have been set by international standard and have to be followed strictly. For example, the International Telecommunication Union (ITU) standard grid for 100 GHz channel spacing corresponds to 0.8 nm at 1.55 μm band and 0.4 nm for 50 GHz channel spacing. The sidelobe suppression that is required for the channel isolation has to be -20 to -30 dB for tunable filters. The dynamic tuning range has to cover the entire Erbium doped fiber amplifier (EDFA) bandwidth (about 40 nm) at 1.55 μm band. The tuning speed of tunable devices is also an important issue. For circuit switching schemes, one microsecond of tuning speed is enough. However, for future packet switching or cell-switching schemes, 10-nanosecond or less changing speeds will be required. These different technical issues, combined with the implementation possibilities, will set the limitation on every technology that possesses the tunable capability.

2.3 FABRY-PEROT VERTICAL CAVITY TUNABLE FILTER

The Fabry-Perot cavity was invented more than 100 years ago. The operating principle is quite simple: two mirrors are lined up and form a resonant cavity between them. The distance between the mirrors defines the resonant wavelength of the cavity. The device will have a reflection dip when the optical wave has the same phase (2 difference) after a round-trip. The shape of the transmission peak is a Lorentzian function of the frequency. To change the cavity length, we can either change the refractive index of the media in the cavity or physically change the position of one of the two mirrors. There are a number of electro-optical effects which can produce a change in the refractive index. In semiconductors, this is usually achieved by injecting electrical current through the device and the increased carrier density will affect the refractive index. However, this phenomenon is quite limited in expanding the tuning range (less than 10 nm). Another way to change the refractive index in the cavity is to insert a ferroelectric liquid crystal to fill the cavity. The electrodes create an electric field over the cavity and this field can change the spatial orientation of the liquid crystal molecules[2]. The performance of this device is also somewhat limited: 14 nm for tuning range and a linewidth of 0.84 nm, but a switching time of around 400 μs .

To achieve a larger tuning range, the other method, i.e. moving the mirror position, has to be implemented. This can be done in several different ways: one can use heat or the piezo-electric effect to change the distance between two fiber facets[3]. The finesse of the cavity is as high as 200 but the tuning time is quite long, on the millisecond scale. Another approach is using micromachining technology, which makes one movable mirror to vary the cavity length by electrostatic force or other actuation energy. In the past, most of the micromachined devices were made of silicon because its fabrication processes are better developed than those of III-V compound semiconductors. Since only III-V compound semiconductors can emit and detect light efficiently, it would be better to use GaAs or InP as the base material for the convenience of future integration of active and passive components. Different structures have been implemented for micromachined tunable devices such as flip-chip bonded mirrors[4], deformable membranes[5], cantilevers[6], etc.. The effective cavity length of these devices can be changed by applying electrostatic force. The tuning range can be as large as 70 nm in the 980 nm band[6] and the insertion loss is only 0.9 dB[7]. The polarization dependence of these devices is minimum if we use a vertical cavity structure and have light incident normal to the surface of the wafer. More theoretical details of Fabry-Perot resonator will be discussed in Chapter 4.

2.4 ACOUSTO-OPTIC TUNABLE FILTER

The concept of acousto-optic tunable filter was first invented by S. E. Harris, and R. W. Wallace in 1969[8]. When an acoustic wave travels in a crystal, the induced strain among the atoms changes the refractive index of the crystal. If an optical beam is incident on such a crystal, it will be diffracted differently with the acoustic wave on or off. In an anisotropic medium, like LiNbO_3 , the light might be diffracted from one polarization to another under some crystal orientations. Just like the Bragg condition in X-ray diffraction, the condition for a strong interaction between the input waves will be when the sum of the wave vectors equals the wave vector of the orthogonally polarized diffracted wave.

To have an acousto-optic filter, the incident optical wave will be diffracted into another orthogonal polarized direction by a collinearly propagating acoustic wave. For a specific input acoustic frequency, only a small range of optical frequencies can satisfy the wave vector rule above and thus have strong transmission. If the acoustic wave frequency is changed, the corresponding transmitted optical frequency will be changed,

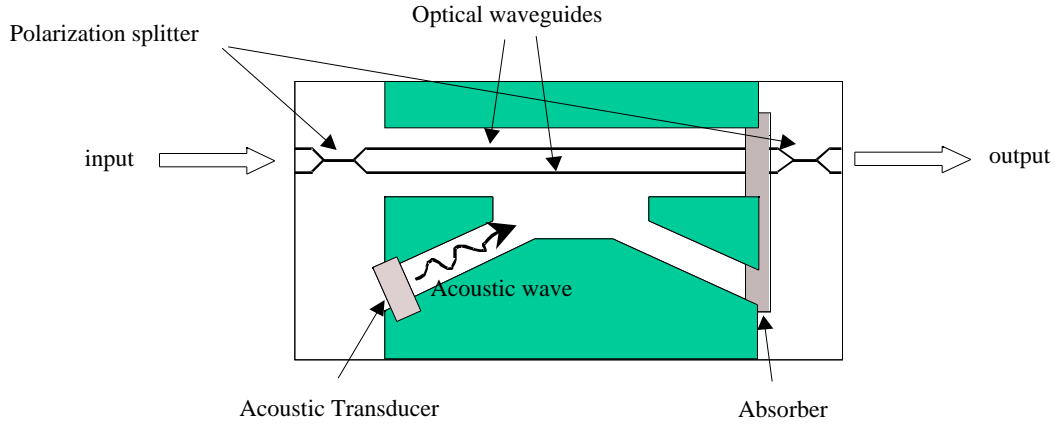


Fig. 2.1: The modern design of the acousto-optic tunable filter [9]

too. The ratio of the output power in one polarization to the input power of the orthogonal polarization is as follows[8]:

$$\frac{P_x(L)}{P_z(0)} = \frac{\omega_o}{\omega_e} L^2 \frac{\sin^2 \left(\sqrt{\frac{k^2}{4} L} \right)}{\frac{k^2}{4} L^2} \quad (2-1)$$

where L is the length of the anisotropic crystal, the propagating direction of optical wave is along y-axis, x and z are two orthogonal axes in the optical field, $P_x(L)$ and $P_z(0)$ indicates the output power at the end of crystal ($y=L$) and the beginning position of the crystal ($y=0$), respectively, ω_o is the frequency of the output optical wave, ω_e is the frequency of the input optical wave, and k is a parameter related to this anisotropic material. The k in the expression is the mis-match between the three propagating waves, including the input/output optical waves and input acoustic wave. So k will be written

as: $k = k_o - k_e - k_a$, where k_o , k_e , and k_a are the wave vectors of the output optical wave, input optical wave, and acoustic wave, respectively. It is clear that when k equals zero there will be nearly 100% transmission (assuming k_a is very small compared to other two terms) if L is $\lambda/2$. The transmittance of this filter is basically a sinc^2 function. With the capability of changing the acoustic frequency, we can achieve a very wide

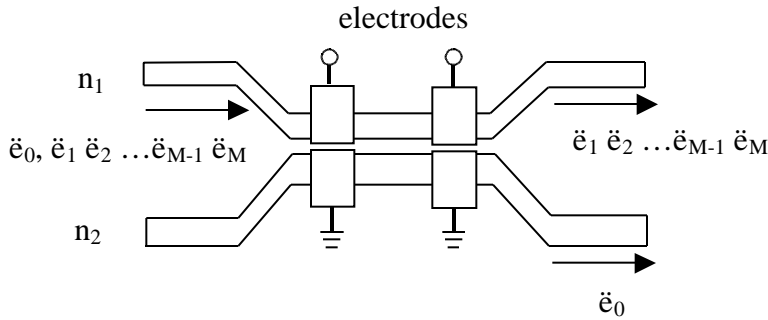


Fig.2.2: The schematic diagram of the electro-optic tunable filter

tuning range (covered from $1.3 \mu\text{m}$ to $1.6 \mu\text{m}$) at relatively high speed (in the range of μs)[1].

Modern tunable acousto-optic filters tend to have a monolithic design[10], as shown in Fig. 2.1. The generic collinear acousto-optic filter based on x-cut, y-propagating LiNbO_3 has single-mode optical fiber to let signal in and out. The acoustic wave is generated by interdigital transducers (IDT's), which are confined to an acoustic waveguide. A typical drive power of 10mW is needed for acoustic wave generation. Some other technologies have been integrated with the basic elements of this tunable filter scheme such as polarization beam splitters, proton-exchange waveguides. One of the disadvantages of this tunable filter is the polarization dependence of the input light wave. By integrating the mode converter with two polarization splitters, and the acousto-optic tunable filter can achieve less than 1 dB in polarization dependence[9].

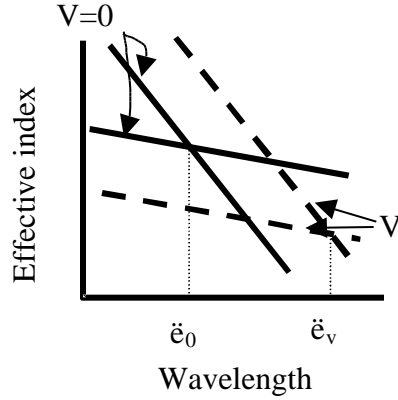


Fig. 2.3: The tuning mechanism of the electro-optic filter. The solid curves are the two dispersion curves of the waveguides. The intersection point, λ_0 , is the phase-matching wavelength. When the voltage is applied to the filter, the matching point will move to λ_v due to the electro-optic effect.

2.5 ELECTRO-OPTIC TUNABLE FILTER

The operational principle of the electro-optic tunable filter is very similar to that of the acousto-optic filter. Fig. 2.2 shows the general diagram of the filters [11]. There are two waveguides composed of material with two different refractive indices, n_1 and n_2 , and two different electrodes to apply the voltages. Without these two pairs of electrodes, the two waveguides form a directional coupler. As shown in Fig. 2.3, only the phase-matching condition at a specific wavelength, λ_0 , can cause a strong coupling between the two waveguides and the input light wave can be observed from the output port of the other waveguide. In the WDM system, if we have multiple wavelength signals coming into the upper branch of the waveguide, with suitable geometry design, only one wavelength, λ_0 , will be coupled to the other branch as shown in the illustration. When an electric field is applied to the waveguide material, the effective refractive indices of the two waveguides are changed due to the electrooptic effect of the material. This change in effective refractive index shifts the dispersion profile of the waveguide as shown in Fig. 2.3, which results in the shifting of the characteristic wavelength[11]. The transmission profile can be described by the following equation[11]:

$$|S(\lambda)|^2 = \sin^2 \left[L(\kappa^2 + \delta^2)^{1/2} \right] \left(1 + \frac{\delta^2}{\kappa^2} \right)^{-1} \quad (2-2)$$

where $S(\Delta k)$ is the so-called “cross-over efficiency”, L is the length of the interaction, Δk is the coupling coefficient, and Δk is the wavelength-dependent phase mismatch ($\Delta k = (\pi/\lambda)[n_1(\lambda) - n_2(\lambda)]$).

With two pairs of electrodes, we can actually adjust the cross-over coupling of the selected channel to be 100%. The equation (2-2) is very similar to that in acousto-optic tunable filters, which means this filter suffers the same problems as the acousto-optic filters. The polarization dependence is strong in this kind of devices since they rely on the plane wave guide. Thus integration of TE/TM polarization splitters and TE/TM mode converter/combiner are necessary to achieve independence of polarization [12].

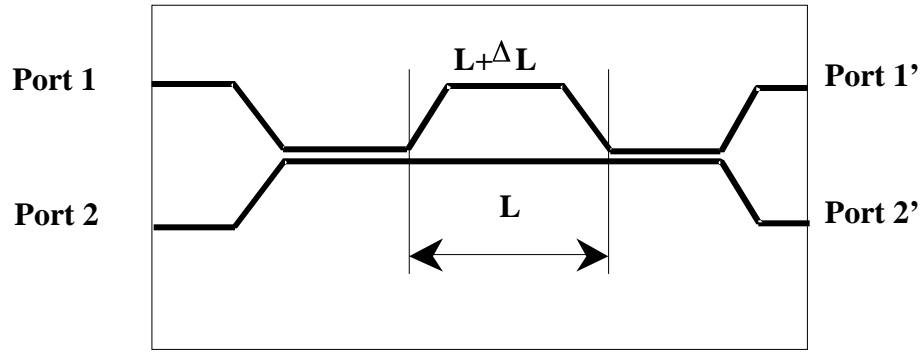


Fig. 2.4: The basic device layout of a Mach-Zehnder optical interferometer.

2.6 MACH-ZEHNDER TUNABLE FILTER

Mach-Zehnder interferometers have been applied to phase modulators, optical frequency translators and signal processing applications[13]. The basic concept of the devices is shown in Fig. 2.4. This is a 2×2 configuration. The two different input waves will travel with different optical path (L and $L + \Delta L$) inside the silica waveguide. The phase differences between these two waves will cause an interference effect at the output ports. With careful design of ΔL , the power outputs at port 1' and 2' can be related to the input power at port 1 and 2 (if only one wavelength is present in the waveguide) [13]:

$$\begin{aligned} P_{1'} &= \sin^2(k \Delta L / 2) \times P_1 + \cos^2(k \Delta L / 2) \times P_2 \\ P_{2'} &= \cos^2(k \Delta L / 2) \times P_1 + \sin^2(k \Delta L / 2) \times P_2 \end{aligned} \quad (2-3)$$

where k is the wave vector. When there are two wavelengths of signal present in the waveguide, the above equation can be modified by changing the wave vector to the difference between the two wavelengths, but the basic \sin^2 relationship is kept. This interferometer can then become a wavelength selective device. One port may have more output power of the specific wavelength than the other output port.

To make a generic Mach-Zehnder filter tunable, one could transfer to the unbalanced type of this interferometer, which can be seen in Fig. 2.5[14]. The tuning mechanism relies on the electro-optic effect of LiNbO_3 . The transmission function of this unbalanced Mach-Zehnder filter still follows the \sin/\cos expressions in eq. (2-2). However, due to this specific transmission function of the system, if the

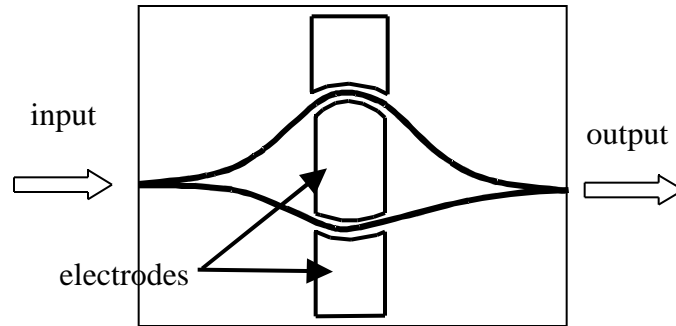


Fig. 2.5: Unbalanced Mach-Zehnder tunable filter. The central electrodes are the controller to change the refractive index of the waveguide material via electro-optic effect.

required transmission linewidth must be narrower, the free spectral range of the system will be reduced. Because of this, filtering out a single wavelength in a WDM signal requires several Mach-Zehnder filters to be cascaded in series to achieve the required performance as shown in Fig. 2.6 [14]. The switching speed between different channels is very fast, typically is less than 50 ns. The insertion loss of the device can be around 1 dB and crosstalk is less than -22 dB. The tuning range, however, is limited to 4 nm.

2.7 COMPARISON AND SUMMARY

These major technologies have already been applied to tunable filters successfully. Most of them use the interference of two input waves. Planar waveguides are general characteristics of these devices. Some of them rely on nonlinear phenomenon of the waveguide material to enhance the tunability. Only the Fabry-Perot cavity can have

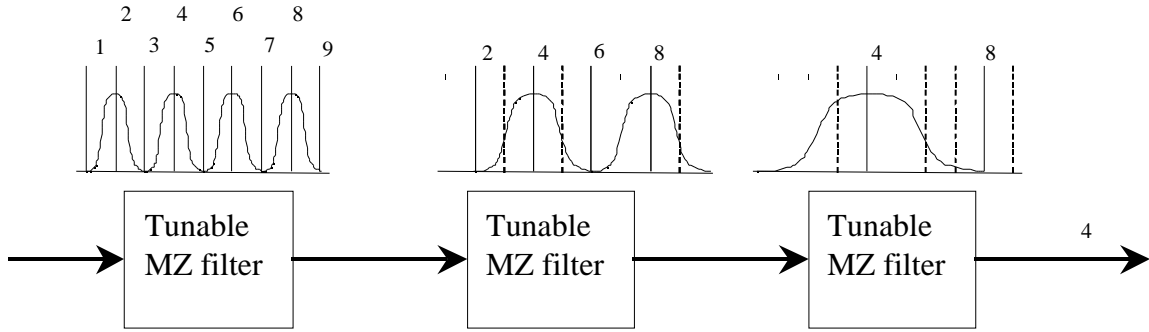


Fig. 2.6: The cascaded tunable Mach-Zehnder (MZ) filter for single channel transmission.

	Advantage	Disadvantage
Fabry-Perot filters (Vertical Cavity)	Simple structure, narrow linewidth, reasonable insertion loss, no polarization dependence	Moving component, tuning speed (10 ₋ s)
Acousto-optic filters	Wide tuning range, fast tuning speed (μs)	Polarization dep., loss, linewidth, power consumption, 2-D integration
Electro-optic filters	Very fast tuning speed (ns)	Same as above
Mach-Zehnder filters	Narrow linewidth, fast tuning speed (50 ns)	Narrow tuning range (~nm)

Table 2.1: Comparison among the major tunable filter technologies.

the light path normal to the device surface. Because the interference effect dominates the filtering action, the resultant transmission is related to a sinusoidal function. The sidelobes of this sinusoidal behavior become important when the channel spacing is reduced. Inter-channel interference will become serious if these sidelobes are not suitably suppressed. The power consumption of these different technologies varies greatly. Fabry-Perot tunable filters which consume virtually no power can be realized because the power to move the mirror is basically capacitive charging. On the other hand, filters such as acousto-optic filters or electro-optic filters, need to pump extra power through tuning mechanism components, for example, the acoustic actuation transducer, in addition to running current in the devices. These are not serious problems in the research lab developing stage, but they become more important when the commercialization of the technology is considered.

The following table (Table. 2.1) compares the advantages and disadvantages among these major technologies to realize tunable filters. Other methods, such as fiber Bragg gratings, arrayed waveguide grating, or ring resonator tunable filters are all subsets of these technologies or have inferior performance to them. From this table, the benefits of the Fabry-Perot vertical cavity scheme are very obvious. Although this structure needs a moving component and only has moderate switching speed. The advantages it brings are greater than the competing technologies. When the fabrication and packaging techniques advance, the moving component will not be a major obstacle and the switching speed can be increased by changing the mechanical design of the movable part.

In the following chapters, we introduce a more detailed description of the design, fabrication, and measurement of the micromachined tunable optoelectronic devices based on the Perot vertical cavity.

Chapter 3. Mechanical analysis of the deformable membrane

3.1 INTRODUCTION

With increasing demand on data transmission, more bandwidth is required. Large efforts have been made to increase the modulation bandwidth of both lasers and detectors in the past. However, to achieve a quantum leap in accessible bandwidth, multiple channels, instead of one, have to be realized in optical fiber systems. This is called wavelength division multiplexing (WDM). The essential components in this scheme are the wavelength tunable devices that can be used as transmitters and receivers of different channels. Continuous tuning is especially desirable to make systems more failure tolerant of any specific channel because all the components are capable of performing the function of the channels.

Surface-micromachined deformable mirrors have been used for adaptive optics and continuously wavelength tunable optoelectronic devices. In previous research, high density arrays [15] and devices, such as filters [5;7], detectors [16], and lasers [17] have been implemented. Fig. 3.1 shows the basic structure of the devices. Dielectric materials and Au/Si have both been used for highly reflective layers in these cases. To achieve higher mirror reflectivity, $\text{Al}_2\text{O}_3/\text{GaAs}$ distributed Bragg reflectors (DBRs) have been investigated. Table 3.1 shows a comparison between different types of mirrors. $\text{Al}_2\text{O}_3/\text{GaAs}$ pairs have a larger index contrast than the other materials. Unfortunately, deformable $\text{Al}_2\text{O}_3/\text{GaAs}$ DBRs are much stiffer and suffer a much high tuning voltage [7]. To overcome this problem, we have designed and fabricated a new structure that capitalizes on the high reflectivity of $\text{Al}_2\text{O}_3/\text{GaAs}$, but avoids the high tuning voltage.

In this chapter, we are going to develop a mechanical evaluation process for the design purpose of the tunable structure. This mechanical evaluation has to be easy enough to obtain the results quickly while achieving sufficient accuracy of the evaluation to be useful. A one-dimensional Hooke's model is first used to calculate the displacement versus tuning voltage relationship. This method is simple yet powerful. We secondly

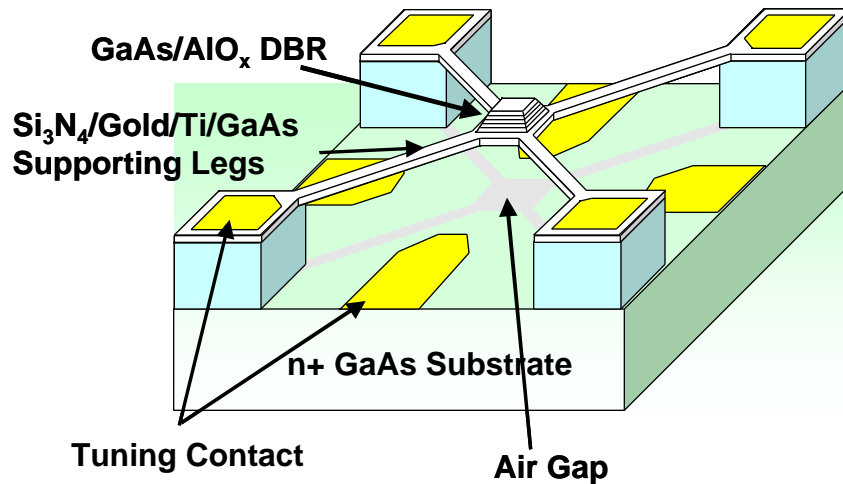


Fig. 3.1: Schematic diagram of the surface micromachined tunable devices.

apply basic bending theory of a non-uniform cross section plate to find out the internal stress of different top designs because this internal stress will affect the stiffness of the top structure during the actuation. A classical method, called the area moment method is then applied to calculate the deformation profile of the membrane under electrostatic actuation. All three methods comprise the main evaluation of the mechanical design of the devices. The mechanical design is very essential for a micromachined object because the final tuning characteristics and frequency response are completely dependent upon the mechanical layout.

3.2 ELECTROSTATIC ATTRACTION FORCE AND ONE DIMENSIONAL MODEL

In this section, the basic theory of movable membranes will be discussed. The model is based on one-dimensional Hook's law such that we do not lose physical intuition. The 1-D results are fairly accurate compared to full three dimensional calculation [18]. To visualize this one-dimensional model, we can first observe the action of the real device shown in Fig. 3.1. The real device is composed of an over-hanging central plate with designed optical multiple layers and four supporting legs extending from the posts. When the electrostatic field is applied between the top plate and substrate, the attractive force will pull the central plate towards the substrate. This process has to be

balanced by a mechanical force developed in the top structure in order to prevent it from collapsing onto the substrate. Usually this specific force originates from the tensile stressed silicon nitride film deposited on the supporting legs. The movable membrane can thus be treated as four springs tied to a central plate assuming it as a rigid body. When the electric field is applied between the top and bottom plate, the electrostatic attractive force will pull the plate toward the substrate. However, the springs act as a counter-force to keep the plate at a balanced position. Usually the four supporting legs with tensile stress material are regarded as spring sets, which will balance the electrostatic attractive force applied between the top and bottom surfaces. The forces in a one-dimensional force model can be found [18;19] :

$$F_{mechanical} = F_{stress} + F_{bend} + F_{stretch} = F_{stress} \times \left(1 + \frac{\pi^2 E}{3\sigma} \frac{h^2}{l} + \frac{\pi^2 E}{4\sigma} \frac{u^2}{l} \right) \quad (3-1)$$

$$F_{stress} = \frac{N_l b h \sigma}{l} u \quad (3-2)$$

$$k_{eff} = \frac{N_l b h \sigma}{l} \left(1 + \frac{\pi^2 E}{3\sigma} \frac{h^2}{l} + \frac{\pi^2 E}{4\sigma} \frac{u^2}{l} \right) \quad (3-3)$$

where k_{eff} is the effective Hook's constant, l is the length of the supporting legs, and F_{stress} , F_{bend} and $F_{stretch}$ represent the corresponding mechanical force components. F_{stress} is due to the deposition condition of the film. F_{bend} is the linear bending force. The third component is due to the stretching of the beam at large displacement. In our case, since the Young's modulus and material stress are about the same order and the length of the supporting legs is much larger than the thickness of the film or the displacement (1 μm to 120 μm), the second and third term in k_{eff} are basically negligible. The theory of the electrostatic force that acts on the structure has been fully discussed in previous dissertation [19] and I am going to briefly reviewed it below. Since both the plate and legs have

Material for mirrors	Refractive Index	Reflectivity	# of DBR for 99.95%
Si ₃ N ₄ /SiO ₂	2.05/1.46	0.9278(4 pairs)	12
GaAs/AlAs	3.53/2.96	0.7583(4 pairs)	22
GaAs/Al ₂ O ₃	3.53/1.55	0.9984(4 pairs)	5
Au/Si[20]	N/A	0.91	N/A
Polysilicon/SiO ₂ [21]	3.44/1.46	0.74 to 0.69	N/A

Table. 3.1: Comparison of reflectivity between different material systems

the electric field across them, the electrostatic force can be further formulated as follows [19] :

$$\begin{aligned}
F_{electrostatic} &= F_{plate} + F_{leg} \\
&= \frac{A\epsilon_0 V^2}{2(g_0 - u)^2} + 4w \int_0^l \frac{\epsilon_0 V^2}{2(g_0 - ux/l)^2} dx \\
&= \frac{A\epsilon_0 V^2}{2(g_0 - u)^2} + \frac{2wLV^2}{g_0(g_0 - u)}
\end{aligned} \tag{3-4}$$

In eq. (3-4), an important assumption is that the deformation of the legs is linear from the post to the center. In real situations, this is not true. However, most of the electrostatic force comes from the first term, which is the central plate term, so this approximation is fairly accurate compared to the fully analyzed displacement [18;19]. For this system to be stabilized, the electrostatic force and the mechanical restoring force have to be equal. So we can get a final expression as :

$$\begin{aligned}
F_{electrostatic} &= F_{mechanical} \\
\frac{A\epsilon_0 V^2}{2(g_0 - u)^2} + \frac{2wLV^2}{g_0(g_0 - u)} &= \frac{N_l b h \sigma}{l} u
\end{aligned} \tag{3-5}$$

This expression is simple yet very useful to evaluate the behavior of this deformable membrane system. Fig. 3.2 shows both the experimental measurement and calculation from this model, and as we can observe, the model fits pretty well.

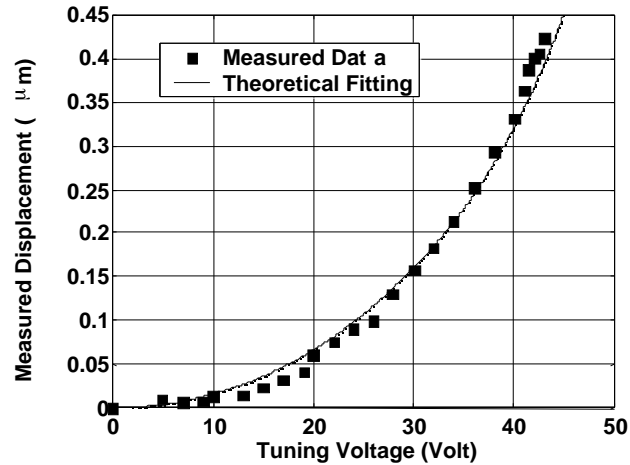


Fig. 3-2: The theoretical fitting of the one-dimensional model

3.3 TOP STRUCTURE DESIGN – PLATE THEORY

In addition to the general relationship between displacement and applied voltage, one must consider how to design the central membrane. Usually this part is simple because the central object can be treated as a rigid body. However, as the structure becomes more complex, it is possible that some part of the membrane is easier to bend, and treating the problem as a rigid body is then not suitable. This non-standard situation creates extra tension which is not necessary and to solve this problem, the central membrane has to be regarded as a plate. In this section, the basic plate theory will be reviewed and applied to the actual design of our top membrane. The generalized plate theory leads to a bendable structure whose cross-section is not always the same. The final result will demonstrate the better layout that reduces the internal stress of the structure.

3.3.1 Pure bending of plates

Before further discussion of the bending of our micromachined structure, it would be beneficial to first review some of the essence of the general plate theory. Fig. 3.3 shows a generic plate with a small deflection. The small deflection, dw , caused by external forces on the plane, can be described by the local slopes of the surface element between the two adjacent points on the plate: a and a_1 [22]:

$$dw = \frac{w}{x} dx + \frac{w}{y} dy \quad (3-6)$$

where dw is the displacement along the z axis, dx and dy are the infinitesimal length between point a and point a_1 . The curvature along the x axis, r_x , and y axis, r_y can be defined as:

$$r_i = -\frac{\partial^2 w}{\partial i^2}, \text{ where } i = x \text{ or } y \quad (3-7)$$

On the other hand, the direction between a and a_1 plus the perpendicular direction, \vec{at} , can also provide another curvature sets, r_n and r_t . The angle between \vec{an} and x axis is called α . These two sets of curvatures, $r_{x,y}$ and $r_{n,t}$, must obey the following rule [22]:

$$\frac{1}{r_n} + \frac{1}{r_t} = \frac{1}{r_x} + \frac{1}{r_y} \quad (3-8)$$

In the future discussion, it will be of our great interest to find the maximum and minimum of the surface curvature. By setting the expression of derivative of r_n , the maximum/minimum can be found as [22]:

$$\tan 2\alpha = \frac{2r_{xy}}{\frac{1}{r_x} - \frac{1}{r_y}} \quad (3-9)$$

From this expression, two angles can be solved. One of them represents the maximum of surface curvature at point a , and the other represents the minimum. These two angles are separated by $\pi/2$ and the curvatures they represent are called principal curvatures of the surface.

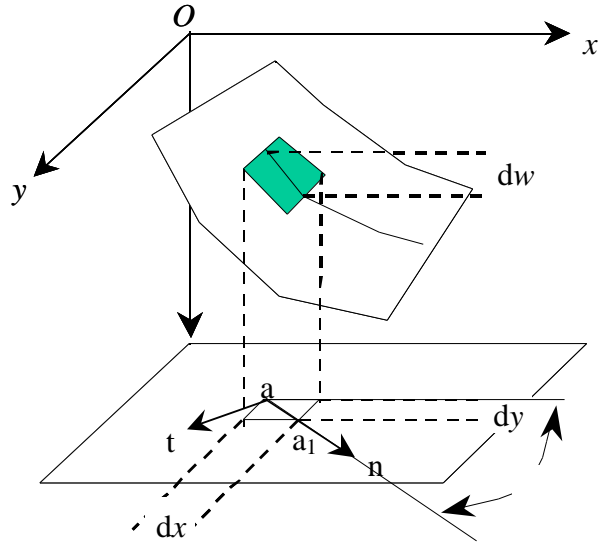


Fig. 3.3: The illustration of the small bending of a generic plate.

3.3.2 Symmetrical deflection of circular plates

We start with a circular plate with some load acting on it. As shown in Fig. 3.4, if the load is symmetrically distributed on the plate, the deformation of the plate will be symmetric, too. In Fig. 3.4, if we take point O as the origin of the coordinates at the center of the undeflected plate, and w as the displacement, and r as the radial distance from O, the maximum slope of the deflection is $-dw/dr$, and the two principal curvatures, that represent the maximum and minimum of the surface curvatures at the point A, will be as follows [22]:

$$\frac{1}{r_n} = -\frac{d^2w}{dr^2} = \frac{d\varphi}{dr} \quad (3-10)$$

$$\frac{1}{r_t} = -\frac{1}{r} \frac{dw}{dr} = \frac{\varphi}{r} \quad (3-11)$$

where r_n is the radius of one of the principal curvatures of the deflection surface at A, r_t is the radius of the second principal curvature, α_1 is the small angle between the normal to the deflection surface at A and the axis of symmetry OB. The physical bending is very

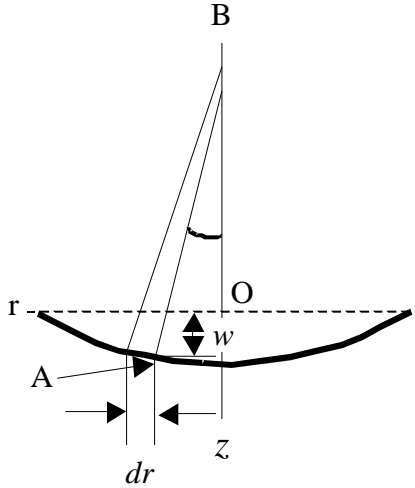


Fig. 3.4: Symmetric bending of circular plates

clear from the introduction of previous paragraph. This displacement (or curvatures) of the targeted surface is caused by the external force acting on it. The relationship of these two physical quantities (bending and force) is built on the famous Hooke's law, ie., the small elongation of the material is proportional to the force exerted on the corresponding sides of the material. This elongation of material can be directly related to the curvature of the point. On the other side, the external force is also equivalent to the bending moment because the integration of the unit stress (or force) along the structure leads to the bending moment [22]:

$$\sigma_i z dz = M_i dz, i = x, y \quad (3-12)$$

where σ_i is the specific direction (like x or y) of external stress developed on the structure, and M_i is the bending moment along the same axis of stress.

So knowing the curvatures of the deflected surface, we can solve the corresponding bending moment from the curvatures [22]:

$$M_r = -D \frac{d^2 w}{dr^2} + \frac{\nu}{r} \frac{dw}{dr} = D \frac{d\varphi}{dr} + \frac{\nu}{r} \varphi \quad (3-13)$$

$$M_t = -D \frac{1}{r} \frac{dw}{dr} + \nu \frac{d^2w}{dr^2} = D \frac{\varphi}{r} + \nu \frac{d\varphi}{dr} \quad (3-14)$$

where M_r is the bending moment per unit length along the circumferential sections of the plate, such as the section made by the conical surface with the apex at B. M_t is the bending moment per unit length along the diametric section rz of the plate and D is the rigidity of the plate material. Note that since the direction of the maximum curvature is now in the radius direction, we use “r” instead of “n” for the subscript. The rigidity can be expressed as [22]: $\frac{Eh^3}{12(1-\nu^2)}$. The external load acting on the plate will introduce a

shearing force, Q , in the structure of the plate. For example, in a uniformly loaded case, the relationship between shearing force, Q , and load intensity, q , can be determined as:
 $2\pi rQ = \pi r^2 q$.

The shearing force, Q , is determined by the external load and the internal moments, M_r and M_t , are the corresponding components in the structure. Equating the coupling components introduced by M_r and M_t and the shearing forces Q , we can obtain the following equation of equilibrium in an infinitesimal element of the plate [22]:

$$M_r + r \frac{dM_r}{dr} - M_t + Qr = 0 \quad (3-15)$$

Substituting eq. (3-13) and (3-14) for M_r and M_t , eq. (3-15) becomes:

$$\frac{d^2\varphi}{dr^2} + \frac{1}{r} \frac{d\varphi}{dr} - \frac{\varphi}{r} = -\frac{Q}{D} \quad (3-16)$$

This differential equation can then be solved for φ , and the deflection of the uniform-thickness plate, w , can be solved as integration of φ with proper boundary conditions.

3.3.3 Deflection of plate with non-uniform thickness

If the thickness of the plate is not uniform, the rigidity, D , of the plate will not be constant. So when we replace the former eq (3-15) with D , w , and r , the differentiation of D and the integration of the load intensity, q , have to be taken into account [22]:

$$D \frac{d}{dr} \frac{d\varphi}{dr} + \frac{\varphi}{r} + \frac{dD}{dr} \frac{d\varphi}{dr} + \nu \frac{\varphi}{r} = -\frac{1}{r} \int_0^r q r dr \quad (3-17)$$

where the shearing force, Q , is replaced with the term :

$$Q = \frac{1}{2\pi r} \int_0^r q 2\pi r dr \quad (3-18)$$

since q is no longer a constant quantity as the previous uniform cross section case. To make the equation dimensionless, we introduce the following notation:

$$\frac{r}{a} = x, \quad \frac{h}{h_0} = y, \quad p = \frac{6(1-\nu^2)a^3q}{Eh_0^3} \quad (3-19)$$

where a is the outer radius of the plate, h is the thickness of the plate at any point, and h_0 is the thickness of the plate at the center. Eq. (3-17) becomes :

$$\frac{d^2\varphi}{dx^2} + \left(\frac{1}{x} + \frac{d \ln y^3}{dx}\right) \frac{d\varphi}{dx} - \left(\frac{1}{x^2} - \frac{\nu}{x} \frac{d \ln y^3}{dx}\right) \varphi = -\frac{px}{y^3} \quad (3-20)$$

where x is the normalized distance from the center ($x = r/a$, a is the diameter of the plate), y is the normalized thickness variation along x , $\frac{d\varphi}{dx}$ is the derivative of deflection in the radial direction, ν is Poisson's ratio of the material, and p is a constant related to the plate geometry. A special analytical solution of this equation from reference [22] can be found, if $y = \exp(-x^2/6)$. From [22], φ has the following form:

$$\varphi = p C\varphi_1 - \frac{x}{3-\nu} e^{\frac{\beta x^2}{2}} \quad (3-21)$$

$$\varphi_1 = a_1 x + \frac{\beta^n (1+\nu)(3+\nu)\cdots(2n-1+\nu)}{2 \times 4 \times 4 \times 6 \cdots 2n \times 2n \times (2n+2)} x^{2n+1} \quad (3-22)$$

However, for our case, equation (3-20) is very complex and impossible to solve analytically. To evaluate the problem properly, equation (3-20) is solved numerically by direct substitution by a Taylor series method with proper profile of membrane shape, y . After φ is solved, the diametric internal stress, σ_t , and the membrane deflection, w , can be calculated by the following equations [22] :

$$\sigma_t = \frac{6M_t}{h^2} \quad (3-23)$$

From the above derivation, we can solve the internal stress of the specific structure. For more general non-uniform cross section, numerical methods have to be utilized to get the answer from eq. (3-20).

3.4 DIFFERENT TOP MEMBRANE DESIGNS

With this equation (3-20) solved, we are able to calculate the internal stress of different shapes of the top membrane design. There are two cases under consideration as shown in Fig. 3.5: case (a), the DBR partially covers the base GaAs mechanical supporting layer, and case (b), the DBR fully covers the base GaAs layer. From a fabrication process viewpoint, case (a) is easier to deal with, because the base plate is wider and the alignment of the mask is not critical. In case (b), the alignment of the mask has to be precise. However, it will be the level of internal stress that decides the layout we will choose. As shown in the figure, the central plate of case (a) does not have a

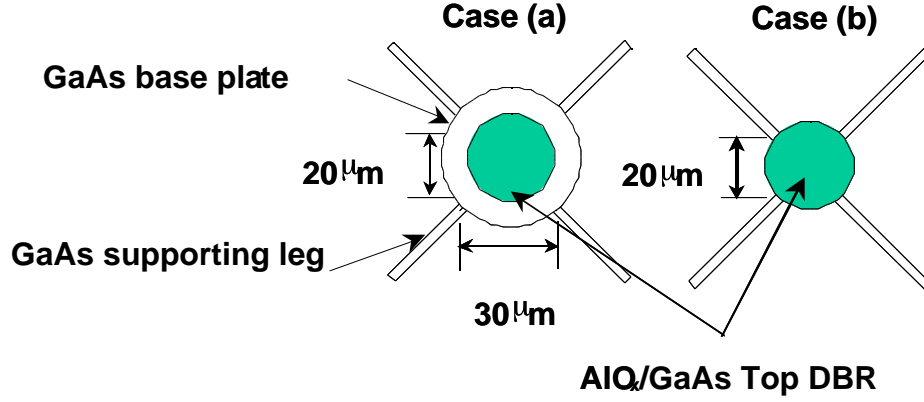


Fig. 3.5: Top view of two different designs for movable top mirrors

uniform cross section while case (b) does, regardless of the supporting legs. The internal stress of the structure will affect the tuning voltage of devices such that we may have to reduce it.

To simulate these two cases, we use the expressions in the previous section about the plate with non-uniform cross section to evaluate the internal stress of these structures. The profile of the plate is simplified by using the following expression:

$$h(x) = \frac{1}{1 + \exp\left(\frac{x - c}{\tau}\right)} \quad (3-24)$$

where c is the starting position of the DBR section and τ controls the slopes of the DBR etch. The ratio between the base plate thickness and DBR thickness is adjusted to closely fit the real situation.

Fig. 3.6 shows the deflection profile of the plate and Fig. 3.7 shows the resultant stress caused by the structures of cases (a) and (b). The profile of the membrane is also shown in the insert of Fig. 3.7. It is very clear that the uniform thickness case does not develop significant internal stress while the non-uniform case develops a large stress. This larger internal stress will make the legs stiffer and harder to bend. It can be also noted that the deflection in the non-uniform case is much larger than that in the uniform case. This will result in a larger curvature in the top mirror which significantly degrades the finesse of the cavity if the size of the light beam covers the whole top plate area. If the

light is focused on to the DBR stack only, these two cases do not make too many differences in terms of optical diffraction loss. The deflection of the plate, though, is always small compared to the length of the air cavity.

From these calculated results, it is clear that although case(a) gives us more room in processing error, case(b) possesses less internal stress and less deflection of the top membrane structure and this can lead to better performance in tuning voltage. However, if the supporting legs are taken into consideration and the local stress is concerned, case (a) will provide a gradual change in the stress distribution, while case (b) does not. So the choice of the structure is totally based on the necessity of the specific application.

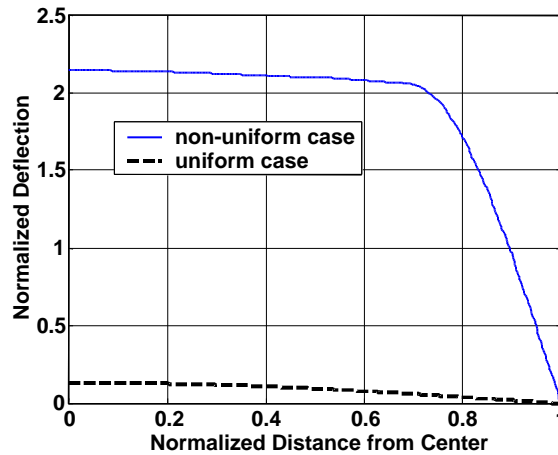


Fig. 3.6: The calculated membrane deflection versus distance from the center of membrane.

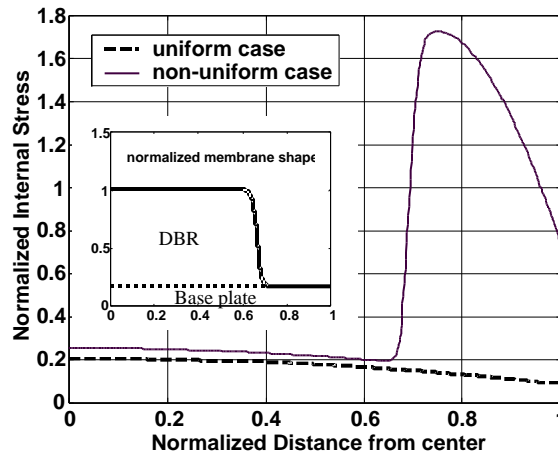


Fig. 3.7: The calculated internal stress for both uniform plate and non-uniform plate. The insert is the membrane profile.

3.5 SURFACE DEFORMATION PROFILE CALCULATION

In the previous section, we discussed the case of the top plate design and how this affects the stiffness of the structure. In order to know the bending profile of the whole structure, including the supporting legs and top membrane, more complete mechanical details must be considered. The deflection profile of the structure is especially important in the central membrane region because this deformation will redirect the incoming light out of the cavity formed by the top and bottom mirrors. Such stray lightwaves cause extra diffraction loss in the cavity and this loss becomes a problem when a high-finesse filter is needed for dense wavelength division multiplexing (DWDM) systems. Previous research [4;23] has already shown that: (a) the surface of movable structures is curved due to electrostatic actuation or internal strain and (b) a linewidth broadening effect has been observed in the filter response. While the broadening effect can be attributed to either added diffraction loss or reduced reflectivity of the top mirror, detailed theoretical analysis is necessary. There are three ways to evaluate the deformation of the whole structure: (a) finite element analysis; (b) static equilibrium differential equations; (c) area moment method [24]. Our goal is to establish a mechanical model which can handle the micromachined structure easily and accurately. Through this model, we wish to quantify the extra optical diffraction losses caused by the curved surface and thus facilitate the design of high finesse tunable filters. The profile calculated above is then input into to an optical-diffraction model, which will be introduced in the next chapter, to estimate optical loss.

3.5.1 Mechanical analysis of deformable membrane profile under external load

In this section, we briefly introduce three methods to solve for deformation profile of the top membrane. The first two methods usually are more costly because they require a lot more calculation time. The area moment method will be far less costly, but need more background in mechanics. For our purposes, a faster and easier design method is preferred because it

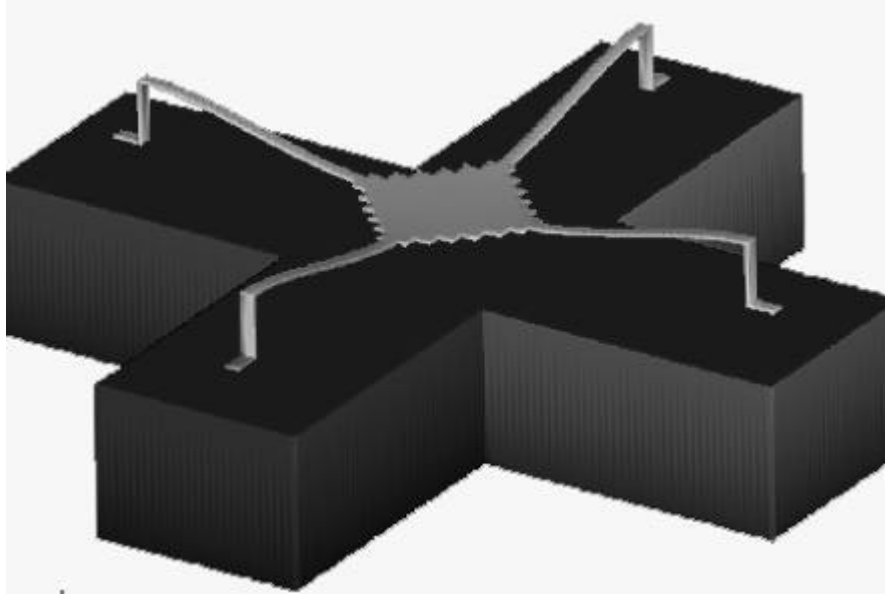


Fig. 3.8: 3-D visualization of the tunable membrane by MEMCAD

fits into engineer's needs better. Greater emphasis is placed on the area moment method in the following discussion.

3.5.2 Finite Element Analysis

Finite element analysis is the most commonly used method to solve for the deformation of micromachined structures. Its principle is to divide the whole structure into several hundreds or thousands of small units, which are called meshes. Each mesh unit follows basic mechanical equations and boundary condition from adjacent units. Once the whole meshing process is finished and the solution of each unit is solved, the solution of the whole structure is produced accordingly. Several commercially available software packages can be used for this purpose. Here we demonstrate such a calculation using MEMCAD by Coventor, Inc.. Fig. 3.8 shows the 3-D visualization of the structure and Fig. 3.9 shows the extraction of the 2-D cross section view of the calculated deformation. The origin of the plot starts from the anchored end of the supporting leg and the slope of the beam is clearly flattened at the center of the top structure.

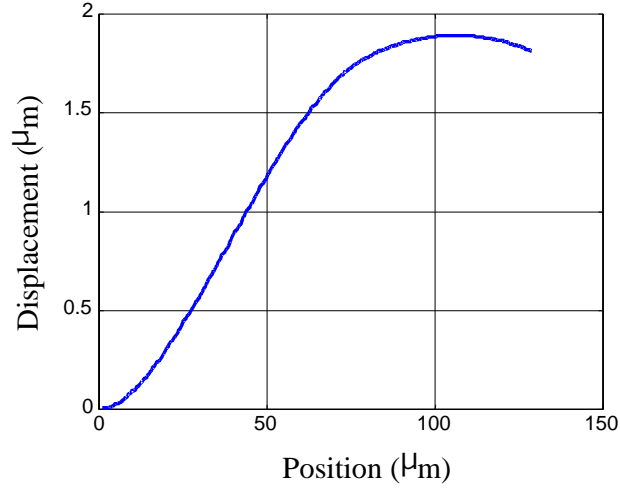


Fig. 3.9: The extracted 2-D cross section of the deformation profile of the tunable membrane shown in the previous figure.

The problem of finite element analysis is that the meshing process and calculation for each element take a long time. Also, failure of meshing process to produce a converging solution is not rare. Another concern is that most of the software programs are so computationally intense and require extensive resources.

3.5.3 Static Differential Equations

If we choose not to use finite element analysis, another approach is to utilize classical static mechanics. The classical pure bending problem of a static beam can be solved directly by writing down the static differential equations. From Hooke's law and the definition of moment of force acting on the specific cross section, we obtain the following expressions [24] (also shown in the Fig. 3.10) :

$$\sigma_x = \frac{Ey}{r} \tag{3-25}$$

$$M(\text{moment}) = \sigma_x \times ydA = \frac{EI_z}{r} \tag{3-26}$$

where σ_x is the stress in the x-axis direction, E is the Young's modulus of the material, r is the curvature of the beam at the position, y is the distance from the center z-axis, and I_z is the moment of inertia with respect to z axis.

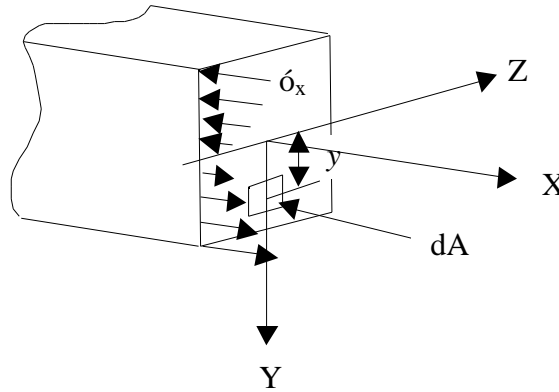


Fig. 3.10: Cross section of the beam with external load. The σ_x denotes the internal stress caused by external load.

Also for small bending, the curvature r can be approximated using second order differentiation of y towards x . So combined with the above formula, we can conclude the bending moment, M , can be related to the bending profile, $y(x)$, like [24]:

$$\frac{d^2 y}{dx^2} = -\frac{1}{r} \quad EI_z \frac{d^2 y}{dx^2} = -M \quad (3-27)$$

Fig. 3.11 shows the classical case of a simple-supported, uniform cross section beam under concentrated load. The bending moment diagram is just a triangle in this case, as shown in Fig. 3.11(b). We solve the deflection profile of the beam by the differential equation sets [24]:

$$EI_z \frac{d^2 y}{dx^2} = -\frac{P(l-a)}{l} x \dots \dots x \quad a$$

$$EI_z \frac{d^2 y}{dx^2} = -\frac{P(l-a)}{l} x + P(x-a) \dots \dots x \quad a \quad (3-28)$$

In eq. (3-28), l is the length of the beam, a is point of load, and P is the load. The solution to these equations is trivial in this case.

Generally, all the situations that can be solved by eq. (3-28) are called statically determinate. However, more constraints are needed when we deal with the fixed-end type of the problem, which means more equations need to be solved in eq. (3-28). More important, the shape of the targeted beam will affect the complexity of the right-hand-side of eq. (3-28). This complexity is against our purpose which is to find an easier way to predict the deflection profile of our structure.

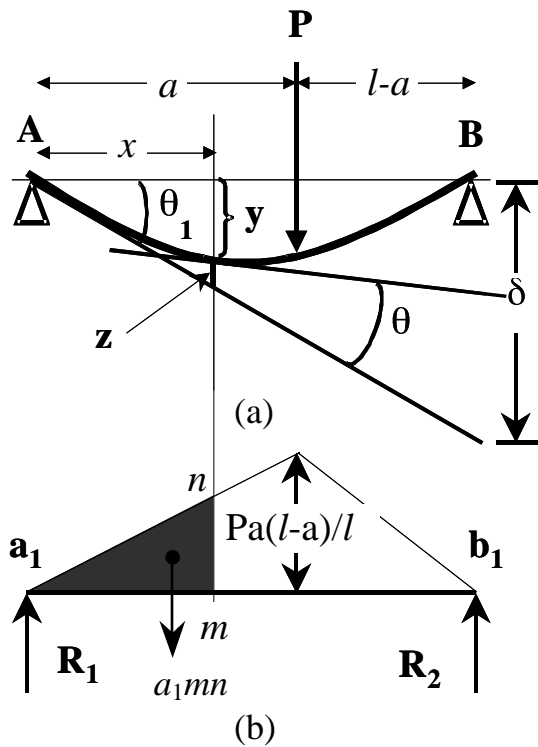


Fig. 3.11: Diagram of a simple-supported beam under a concentrated load: (a) illustration of the physical beam, and (b) bending moment diagram.

3.5.4 Area Moment Method and Conjugate Beams

In most of the cases, the differential equations are difficult to solve directly because of the sophisticated layout of the mechanical structure, but fortunately the solution can be found by using an easier method called “area moment method”. This

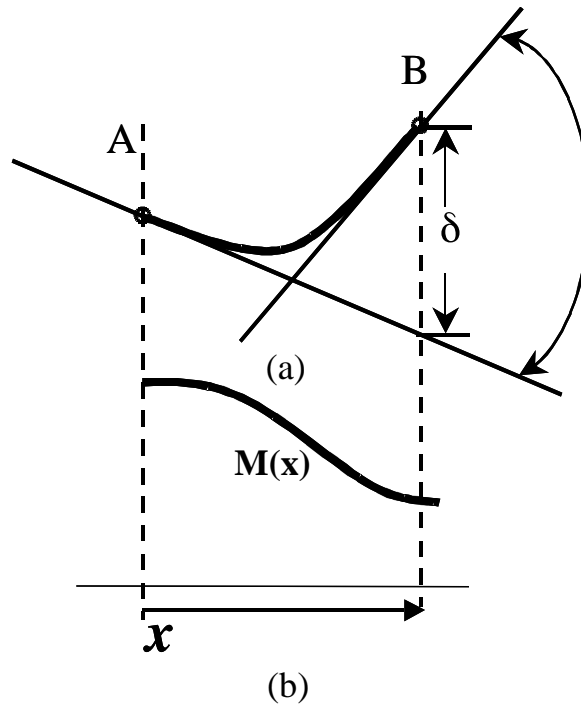


Fig. 3.12: Illustration of area moment method: (a) the beam AB of consideration (b) corresponding bending moment diagram.

method exploits the known results of the regular cases, utilizes and modifies the bending moment diagram and avoids tedious solving of differential equations.

The basic area moment method can be illustrated in Fig. 3.12. When we try to integrate the differential equations (3-28), we are actually dealing with the bending moment diagram. The right-hand sides of equation (3-28) are actually describing the profile of the bending moment, $M(x)$, along the beam. With this understanding, we can solve some parameters of concerns just by looking at the diagram. The displacement, δ , from A to B can be found as [24]:

$$\delta = \frac{\int_A^B xMdx}{EI_z}, \quad I_z = \frac{bh^3}{12}, \quad (3-29)$$

where M is the profile of bending moment diagram, and b and h are the width and height of the cross section, respectively, if it is a rectangular shape. The angle between two tangents, θ , is found as [24]:

$$\theta = \frac{\int_A^B M dx}{EI_z} \quad (3-30)$$

From equations (3-29) and (3-30), one can simply conclude that the bending displacement is the centroid of the bending moment diagram divided by EI_z , and the angle is the same formula except the centroid is replaced with the area under the profile of bending moment diagram.

If the structure is a cantilever, the deflection at every position of the beam can be solved correctly by equation (3-29) and equation (3-30). When the structure is a simple bridge supported at each end, the concept of a conjugate beam has to be introduced. In Fig. 3.11 (b), we can treat the area of the bending moment diagram as a load concentrated at the centroid of the area. The reaction at both ends, R_1 and R_2 , can be calculated and linearly superimposed. From the area moment method, z , \bar{x} , and \bar{y} are already solved. The deflection at any point of the beam, y , can be calculated by $(\bar{y} - x - z)$ for a small deflection. Once we substitute every term, the actual displacement of the beam at this point is found as [24]:

$$y = \frac{1}{EI_z} \left(R_1 x - a_1 mn \times \frac{x}{3} \right) \quad (3-31)$$

where R_1 is the reaction at the end A of the beam due to the load, and $a_1 mn$ is the shaded area under the bending moment diagram, as shown in Fig. 3.11(b). This expression treats the bending moment as a virtual load on the beam $a_1 b_1$. This imaginary beam $a_1 b_1$ is a “conjugate beam” with respect to the real beam, AB. With the concepts of conjugate beams and area moment method, we can solve various problems of uniform cross section beams without resorting to the differential equations.

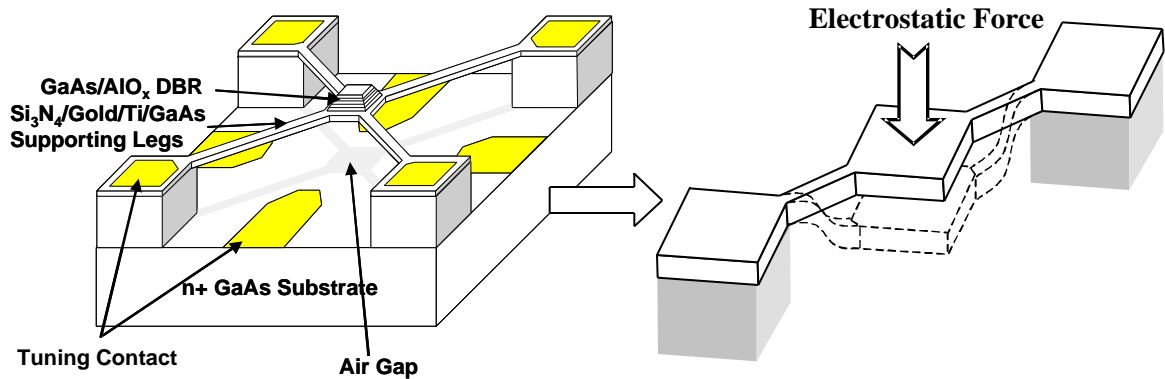


Fig. 3.13: Schematic diagram of the reduced mechanical model

3.5.5 Beams With Fixed End and Various Cross Section

Fig. 3.13 shows the general structure under consideration. The four-leg style membrane is simplified into a two-leg case. This simplification comes from the symmetry of the top membrane. The composite mechanical response under the electrical field for the four-leg structure can be found simply using superposition principle. Two aspects make the problem a little different. First, the fixed posts on two sides make this problem a “built-in” supported beam, whose slope at the post must be zero. Second, the cross section of the beam varies when approaching the center of the membrane due to the enlargement of the central plate (as shown in Fig. 3.13). This change of the width of the cross section is first constant in the supporting leg region and then linear in the central plate if the central plate is square-shaped. Different modifications are necessary for each case.

In the classical static problems, like a simply supported beam or a cantilever beam, there are external loads and supporting ends. The reactions on the supporting ends can be determined by the equations of statics. However, the built-in type of beam is a statically indeterminate problem in which the static equations (such as eq. (3-28)) are not sufficient to determine all the reactive forces at the supports because, in this case, the wall or anchor that fixes the end of the structure also provides some reaction on the beam. Additional reactive elements must be defined to fit the physical constraints, such as the bending slope of the beam [24]. These elements are called redundant constraints (or redundant coupling moments). To solve the varying cross section problem, the bending

moment can be normalized to the supporting leg of the structure [24]. All these modifications are necessary to make the calculation more accurate.

With this understanding, we can begin modeling the structure. To simplify our problem, our example will be concentrated on a four-leg style, fix-ended membrane with a uniform thickness but variable width of cross section. The possible thickness variation can be taken into account through the moment of inertia term that will be shown in the later formulation. We take x as the longitudinal direction, normalized to the whole structure such that x equals 0.5 in the center. Only half of the beam will be analyzed since the structure is symmetric. If the load is concentrated at the center, and the cross section of the beam is uniform, the bending moment will become a simple straight line in the leg portion, which will be $Px/2$ where P is the load. However, due to the change of cross sectional area and thus the moment of inertia, ($I=b(x) \times h^3/12$), grows proportionally to the width of the beam (assuming the thickness is the same). The width $b(x)$ of the cross section is:

$$b(x) = \begin{cases} b_0 & 0 < x < A \\ b_0 \frac{(C-1)}{B}(x-A) + 1 & A < x < A+B \end{cases} \quad (3-32)$$

where A is the normalized starting position of the central membrane and $A+B=0.5$ indicates the center point of the top structure, b_0 is the width of the supporting leg, and the widest cross section in the center is C times larger than the supporting leg. The displacement and angle of the deflection equations will then be modified as [24]:

$$\delta = \int_A^B \frac{xM(x)dx}{EI_z(x)}, \quad (3-33)$$

$$\theta = \int_A^B \frac{M(x)dx}{EI_z(x)} \quad (3-34)$$

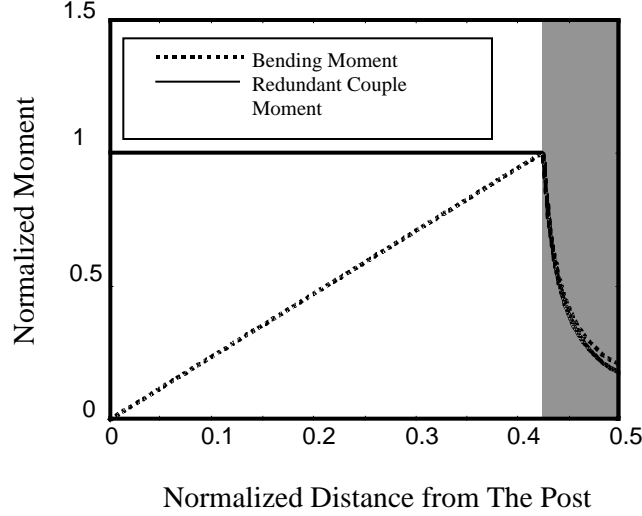


Fig. 3.14: Modified bending moment diagram of bending moment and statically indeterminate coupling. The shaded region indicates the starting position of the central membrane.

where $\frac{M(x)}{I_z(x)} = 6Px / h^3 \frac{(C-1)}{B}(x-A) + 1$. The fixed end of the beam (at $x=0$) has zero slope and we have to introduce the redundant coupling moment. This coupling moment is utilized to assure that the boundary condition (zero deflection angle at the end) will be satisfied. The magnitude of this redundant coupling moment can be found by equating the deflection angle of the original bending moment to this redundant coupling moment [24]. Again, we have to normalize this redundant coupling moment in the central region the same way we normalized the bending moment. Fig. 3.14 shows both the normalized $M(x)$ and the normalized redundant coupling moment of this structure.

Under these considerations, the deflection profile of the structure can be calculated easily and the real shape of the structure will be given by the following superposition:

$$y(x) = g_0 - \frac{u}{2} \frac{y(x)}{\max(y)} \quad (3-35)$$

where $y(x)$ is the calculated result from the area moment method, g_0 is the initial air gap and u is the measured maximum displacement of the central membrane. The factor 2 in the equation comes from the superposition of two identical sets of this structure (i.e. four

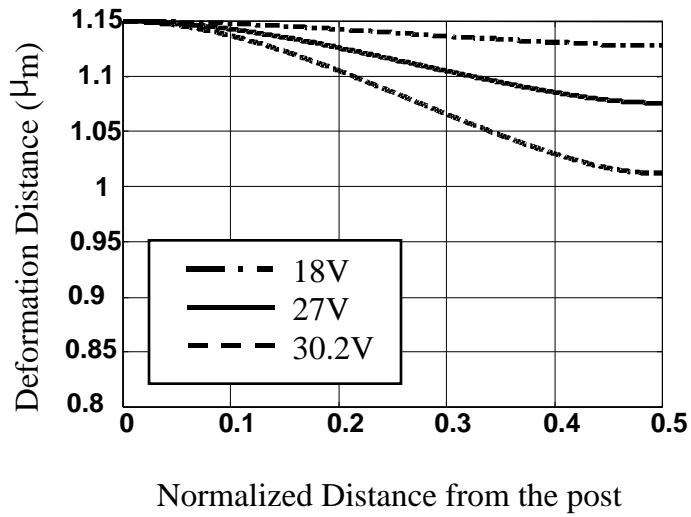


Fig. 3.15: Calculated deformation under different electrical bias voltages.

legs total). Fig. 3.15 shows the deformation under different electrical biases. The central membrane is $20\ \mu\text{m}$ by $20\ \mu\text{m}$ and the supporting legs are $5\ \mu\text{m}$ wide by $120\ \mu\text{m}$ long. As the figure shows, the slope at the center of the membrane is always zero for a symmetric structure. At the post, the slope also has to be zero to satisfy the built-in condition.

3.5.6 Comparison of the two top plate design cases

Once we have solved the deflection profile of the varying cross section beam, as a demonstration, we can compare two designs. They are: (i) the leg and the central plate have the same thickness; and (ii) the central part is thicker than the leg, as shown in Fig. 3.16. The case (i) is the design in the first generation in which the DBR is distributed

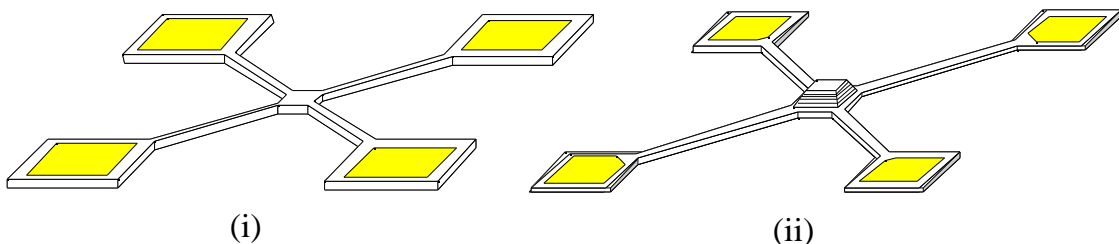


Fig. 3.16: The two cases of the top membrane design : (i) the DBR is everywhere; (ii) the DBR is etched except over the central plate. In (i), the DBR is not removed from the supporting leg region.

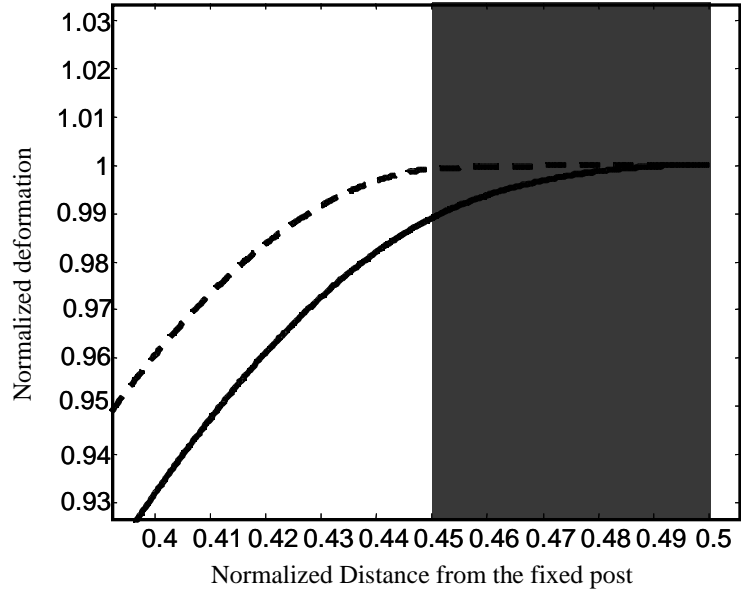


Fig. 3.17: The calculated results of cases (a) and (b). It is obvious that case (b) has much less deformation in the central region (the shaded region).

both the supporting legs and the central plate. The case (ii) is more advanced in terms of the design because the DBR is etched away from the supporting leg region, and this will cause a better tuning voltage due to thinner legs. Another important point of case (ii) is that it “decouples” the reflectivity of the central DBR to the tuning characteristics [25]. The greater the number of quarter wave pairs in the DBR, the higher the reflectivity. However, if the DBR also forms part of the supporting legs, as in case (i), the stiffness of the structure will increase when we try to raise the reflectivity by increasing the number of DBR pairs. With the DBR layers etched away from the supporting leg regions, the two physical properties of the structures (the reflectivity of the DBR and the stiffness of the membrane) are successfully “decoupled” [25]. Using the area moment calculation, we can demonstrate that there is less deformation in the center in case (ii) compared to case (i) (as shown in Fig. 3.17). The reason is simply because the central plate is much thicker than the leg in case (ii), and this will significantly increase the moment of the inertia by the cube of thickness ($I=bh^3/12$). As we can observe from eq. (3-33), the deflection, δ , is inversely proportional to the value of the moment of inertia, so in case (ii), the structure will possess much less deformation, especially in the center. Since it is possible that the deformation of the top membrane will cause additional optical diffraction loss, the

minimum amount of deformation is then highly preferred. Although case (ii) requires additional fabrication processes, we believe that case (ii) is a better approach than case (i). In the next chapter, we will use this information (the deformation of the top plate) to evaluate the additional optical diffraction loss introduced by actuation.

3.5.7 Comparison of the finite element analysis and the area moment method

Although the area moment method combined with the variable cross section concept can provide a very expedient way to evaluate the deflection profile of the structure, the accuracy of this method was still unknown. If this method is not accurate at all, we should just discard it and use one of the more complex models. To find out, we use the finite element analysis method for comparison. One of the common commercial software packages is called MEMCAD by Coventor, Inc.. Fig. 3.8 defines the model we built for this simulation. The central plate is simulated using a zigzag shaped square as shown and the boundary condition of the structure, which is the fix-ended post, can also be simulated using the “fixedAll” condition and four support studs shown in the figure. The width of the central square is four times of the width of the

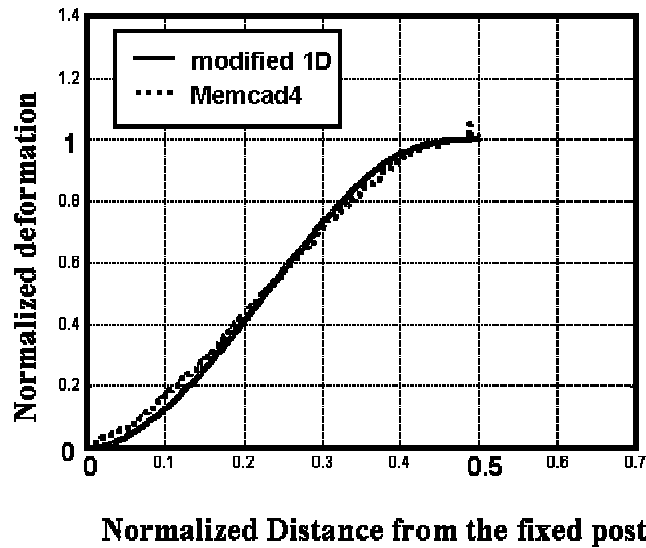


Fig. 3.18: The calculated result of the finite element analysis software (MEMCAD 4.8) and the modified area moment method.

supporting leg. The central plate composes 15 % of the x axis direction length. The final calculation can be seen in Fig. 3.18. As we can see here, the results of these two methods are very close to each other, which proves the accuracy of our modified area moment method for application as the input for an optical designs.

3.6 SUMMARY

In this chapter, we developed a mechanical model and used it to analyze our device structure, especially the top membrane structure. The purpose of the mechanical modeling is to evaluate the internal stress of the designed layout and also predict the deflection profile of the supporting legs and the top membrane structure. If reduction of tuning voltages is a major concern during the device design, we believe that the top DBR layers have to cover exactly the same area with the base GaAs plate to reduce the internal stress. However, this design also introduces extra stress at the junction of the central plate structure and supporting legs that our model does not cover. The other design, in which the DBR does not cover the whole base plate, actually provides a transition from the beam to the plate structure. This transition might be helpful to release some stress in the structure. More experiment results will be demonstrated in the later chapter to illustrate which effect dominates. Also the area moment method can provide a quick and accurate way to calculate the deflection profile. The method we adapt indicates that the thicker central membrane with perfect alignment to the GaAs base plate will give the lowest internal stress and minimum deformation in the central region. The information we gather from this mechanical analysis can be fed back to the optical diffraction loss calculation in the next chapter.

Chapter 4. Optical analysis of tunable optoelectronic devices

4.1 INTRODUCTION

The surface micromachined tunable optoelectronic devices is a wavelength sensitive element which can distinguish between the signals of different wavelength under various actuation conditions. With a movable membrane in the device, these devices can change their cavity length or the light path in the device. The movable membrane significantly increases design varieties, but it also increases the complexity of analysis. In the past, when optoelectronic devices were not wavelength sensitive, the active material such as quantum wells, determined the optical properties of the devices. With WDM requirements to accommodate more channels in the same optical fiber bandwidth to increase the data transmission traffic, wavelength selectivity of the devices has become a critical parameter. This means the linewidth of these WDM devices has to be narrow enough. In the ITU grid, the channel is 50 GHz (0.4 nm) apart in the 1.55 μ m communication band. The design of suitable devices with the required linewidth is thus an important job.

In traditional waveguide devices, the only reflecting surface is the semiconductor and air interface and this is very easy to model. As we increase the cavity finesse, in-plane waveguide devices have evolved into distributed Bragg reflector style, in which a periodic refractive index variation is introduced by etching and re-growing the devices [26]. These grating structures are more complex to analyze and people have used coupled mode theory to solve this problem. With the development of the new materials growth technology, new concepts for optoelectronic devices have evolved. Vertical cavity devices first appeared in the 1980's [27], and they provided a different way of fabricating devices. Instead of having the light path in the plane of the devices, the vertical cavity devices have light oscillating perpendicular to the surface of the devices. Thus the multiple epitaxial layers that compose these devices lying directly in the light path.

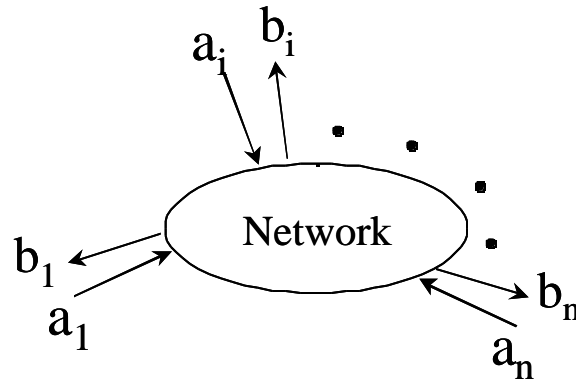


Fig. 4.1: A general scattering network with input ports, a_i , and output ports b_i .

The natural vertical structure makes these devices far easier for two dimensional integration and the optical mode shape is almost a perfect Gaussian while the in-plane waveguide devices always have an elliptical beam shape. These advantages make vertical devices very promising for the future WDM systems. The mirrors in these devices also rely on distributed Bragg reflectors, however, the refractive index difference between layers are usually large, such that scattering matrix theory can be utilized to calculate the exact reflectivity.

When micromachined tunable devices were invented, another issue arose for the optical modeling of the devices: the effect of mechanical parts. The tilting and deformation caused by mechanically movable parts are usually small but the diffraction effect of these structure was not fully understood and analyzed.

Our purpose in this chapter is to start with the scattering matrix theory, which is basically a one-dimensional model to solve the general resonant properties of multiple layers of the vertical cavity devices, and then apply a two-dimensional model, the Fox-Li method, to calculate the field distribution of the cavity due to limited size of the mirrors. The two-dimensional model also provides the information to calculate the diffraction loss of the deformed surface of the top mirror when we apply second order perturbation theory. Finally the experimental results will be compared to evaluate the relative influence caused by this deformation.

4.2 PLANE WAVE MODELING OF MULTIPLE LAYER STRUCTURE

To evaluate the reflectivity of the multiple semiconductor or dielectric layers, one has to work with general scattering theory. In this theory, the multiple layer structure of the device can be mapped to a scattering network illustrated in Fig. 4.1. The input and output of this network can be treated as the incoming light and reflected light components. So from analyzing this network, one can calculate the reflectivity or transmission of the device structure. In a generic network with various input and output ports, the output results are always the linear combination of the inputs [26]:

$$b_i = \sum_j S_{ij} a_j \quad (4-1)$$

where the S_{ij} are called the scattering coefficients, a_j and b_i are the inputs and outputs of the network. So if we have a system with incident and reflected light, we have a two port system which can be described by a scattering matrix as follows:

$$\begin{bmatrix} b_1 \\ b_2 \end{bmatrix} = \begin{bmatrix} S_{11} & S_{12} \\ S_{21} & S_{22} \end{bmatrix} \begin{bmatrix} a_1 \\ a_2 \end{bmatrix} \quad (4-2)$$

If this matrix represents the interface between two dielectrics with refractive indices n_1 and n_2 , the physical meaning of these matrix elements is easy to understand. They represent the reflectivity and transmission from port 1 to port 2 and vice versa. The exact expression can be found as:

$$S_{11} = \left. \frac{b_1}{a_1} \right|_{a_2=0} = -r_1 = \frac{n_1 - n_2}{n_1 + n_2} \quad (4-3)$$

$$S_{22} = \left. \frac{b_2}{a_2} \right|_{a_1=0} = r_2 \quad (4-4)$$

$$S_{12} = S_{21} = t = \sqrt{1 - r_1^2} \quad (4-5)$$

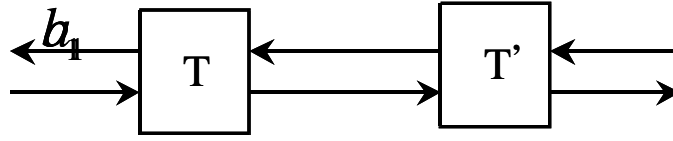


Fig. 4.2: Two scattering networks cascade to each other.

Another notation used to express this scattering network is the transmission matrix, in which the input and output from one given port are represented by the complementary output and input at other ports. The transmission matrix can be related to scattering matrix since they are the different formulation of the same system:

$$\begin{matrix} a_1 \\ b_1 \end{matrix} = \begin{matrix} T_{11} & T_{12} \\ T_{21} & T_{22} \end{matrix} \begin{matrix} a_2 \\ b_2 \end{matrix} \quad (4-6)$$

Obviously, the transmission matrix can be obtained directly from the scattering matrix as follows:

$$\begin{matrix} T_{11} = \frac{1}{S_{21}}, & T_{12} = -\frac{S_{22}}{S_{21}}, \\ T_{21} = \frac{S_{11}}{S_{21}}, & T_{22} = -\frac{S_{11}S_{22} - S_{12}S_{21}}{S_{21}} \end{matrix} \quad (4-7)$$

While the scattering matrix components represent the reflectivity and transmission ratio directly, the advantage of the transmission matrix notation is that we can treat every layer individually and then cascade all the transmission matrices together to obtain the final matrix for the system. For example, in the two networks which share one port, as shown in Fig. 4.2, the total matrix of this system can be realized by :

$$\begin{matrix} a_1 \\ b_1 \end{matrix} = \begin{matrix} T_{11} & T_{12} & T'_{11} & T'_{12} \\ T_{21} & T_{22} & T'_{21} & T'_{22} \end{matrix} \begin{matrix} a'_2 \\ b'_2 \end{matrix} \quad (4-8)$$

Once we adapt the scattering matrix concept, every interface and interior of the epitaxial layers of optoelectronic devices can be treated as one individual transmission matrix. To generalize all the situations that we usually meet in optoelectronic devices, several conditions are summarized below [26]: (The illustration is shown in Fig. 4.3.)

(a) interface between two layers: This is a classical case and the transmission

matrix is like: $\begin{matrix} 1 & r_{12} \\ t_{12} & r_{12} \end{matrix}$, $r_{12}^2 + t_{12}^2 = 1$, where r_{12} and t_{12} are the interfacial reflectivity and transmission, respectively.

(b) inside the individual layer: When the wave propagates inside the medium, there will be a phase variation along the traveling path, and this change can be

expressed by a transmission matrix: $\begin{matrix} e^{j\phi} & 0 \\ 0 & e^{-j\phi} \end{matrix}$, $\phi = \beta_2 L$, where ϕ is the extra phase added onto the optical waves after traveling distance L .

(c) two layers of materials with a traveling distance L : The combination of the above two situations. The reference plane is set to be L from the actual interface between the two materials. The transmission matrix is:

$$\begin{matrix} 1 & e^{j\phi} & r_{12}e^{-j\phi} \\ t_{12} & r_{12}e^{j\phi} & e^{-j\phi} \end{matrix}, r_{12}^2 + t_{12}^2 = 1 \quad (4-9)$$

With these three cases built, the reflectivity of a Fabry-Perot etalon can be implemented. Using the scattering networks concept, three matrices can be written: two at the interface, and one inside the etalon. The reflectivity and transmission at the two interfaces can be denoted by r_1 , and r_2 , t_1 and t_2 , respectively. The resulting scattering matrix components will become [26]:

$$S_{11} = -r_1 + \frac{t_1^2 r_2 e^{-2j\beta L}}{1 - r_1 r_2 e^{-2j\beta L}} \quad (4-10)$$

$$S_{21} = \frac{t_1 t_2 e^{-j\beta L}}{1 - r_1 r_2 e^{-2j\beta L}} = S_{12} \quad (4-11)$$

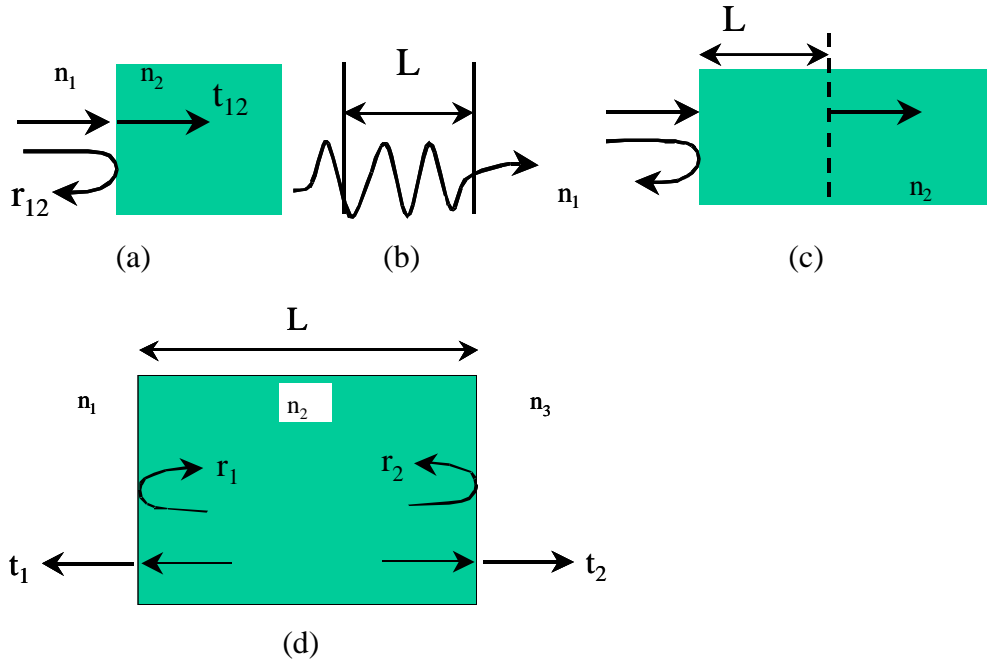


Fig. 4.3: Basic cases in the general multiple layers of optoelectronic devices. (a): interface between two materials. (b) transmission line in one material (c) combination of (a) and (b). (d) a Fabry-Perot etalon.

$$S_{22} = -r_2 + \frac{t_2^2 r_1 e^{-2j\beta L}}{1 - r_1 r_2 e^{-2j\beta L}} \quad (4-12)$$

Fig. 4.4 shows the absolute value of reflection and transmission coefficients (S_{11} and S_{12} , respectively) when the two sides of the etalon have the same material and there is no loss in the cavity. In this case, $r_1 = r_2$ and $t_1 = t_2$ and $|S_{11}|^2 + |S_{12}|^2 = 1$. The maximum peak in the reflection or valley in the transmission occurs at the axial resonances or modes of the cavity where the phase variation, $2L$, equals even integral number of λ . It is also clear from the plot that the reflection and transmission plots demonstrate sharper transition when the facet reflectivity r_1 and r_2 becomes larger.

4.3 APPLICATION OF SCATTERING MATRIX TO MULTIPLE SEMICONDUCTOR LAYERS

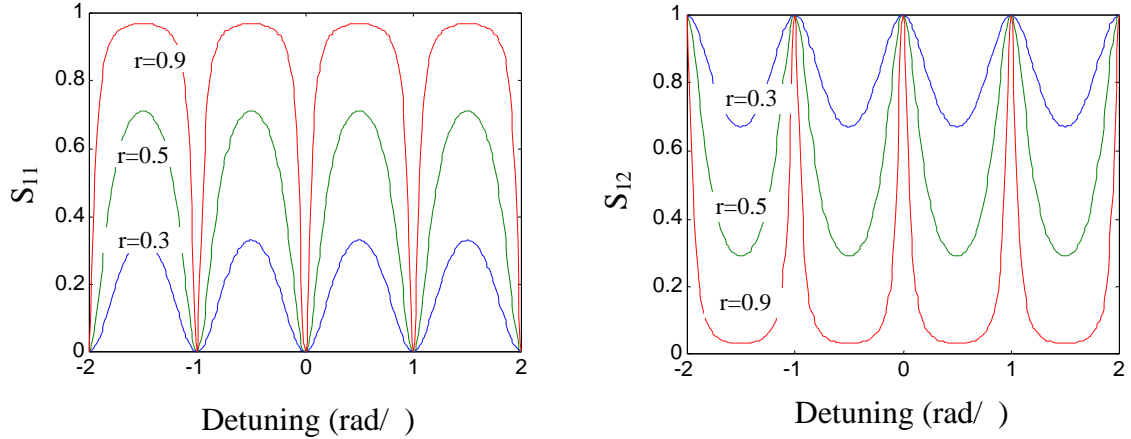


Fig.4.4: The reflection and transmission coefficient S_{11} and S_{12} versus phase variation. Different families of the curves corresponds to $r=0.3, 0.5, 0.9$, respectively.

The advance in materials growth technology has enabled the realization of nearly perfect multiple semiconductor layers in devices. To simulate the optical properties of these structures, we have to rely on the scattering matrices developed in the previous section. Here we are going to apply this theory to the real case and demonstrate a series spectral simulation of tunable optoelectronic devices.

One of the most important structures in modern optoelectronic devices is the distributed Bragg reflector (DBR). DBRs have been applied in vertical cavity devices to enhance the cavity finesse. The high reflectivity formed by multiple pairs makes it a very suitable candidate for laser mirrors. In vertical cavity surface emitting lasers (VCSELs) (for example, [28]), or resonant cavity enhanced (RCE) photodetectors [29], the DBRs greatly increase device performance by containing the optical field in the cavity due to its high reflectivity.

A single DBR pair consists of one high refractive index material and one low refractive index material. The thickness of these two layers is each one-quarter wavelength long. When the light propagating in the media is exactly at this dedicated wavelength, it is called the Bragg condition. Applying the scattering matrix to this structure by replicating m times, we can find the analytical solution for reflectivity at the Bragg condition [26]:

$$r_g = \frac{1 - (n_1/n_2)^{2m}}{1 + (n_1/n_2)^{2m}} \quad (4-13)$$

To calculate the result for propagating waves whose wavelength is away from the Bragg condition, we have to express the whole matrix in a more general way [26]. If we denote the transmission matrix for one DBR pair as T , and the total transmission matrix of the whole structure as T_g , we have the following relationship: $[T_g] = [T]^m$. Since the simple transmission matrix, T , can be easily solved, the composite matrix T_g can be related to the T components as [26]:

$$T_{g11} = \frac{\sinh m\xi}{\sinh \xi} T_{11} - \frac{\sinh m\xi \cosh \xi - \cosh m\xi \sinh \xi}{\sinh \xi} \quad (4-14)$$

$$T_{g12} = \frac{\sinh m\xi}{\sinh \xi} T_{12} \quad (4-15)$$

$$r_g = \frac{T_{g21}}{T_{g11}} = \frac{T_{21}/T_{11}}{1 - \frac{\sinh(m-1)\xi}{T_{11} \sinh m\xi}} \quad (4-16)$$

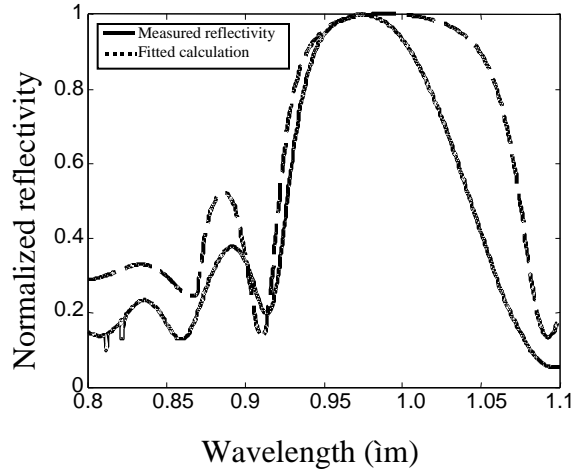


Fig. 4.5: The measured and simulated spectrum of a 10 pairs AlAs/GaAs DBR. The results have been normalized.

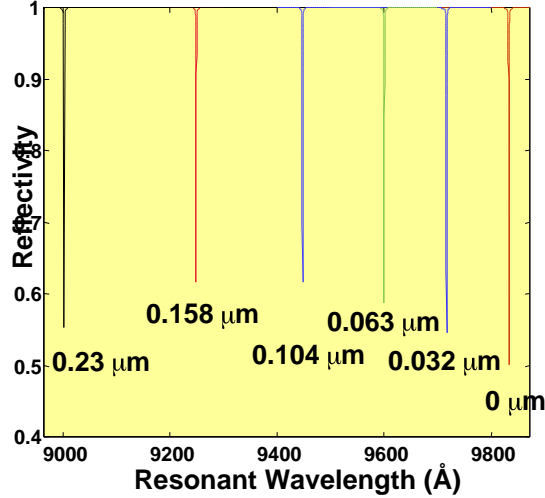


Fig. 4.6: The simulated spectral response of a tunable filter with a 5 pairs $\text{Al}_2\text{O}_3/\text{GaAs}$ DBR.

where β is the discrete propagation constant relating the electric field vector at one plane to the field vector at the next. The exponent of the discrete propagation constant can be treated as the eigenvalue of this DBR structure.

Fig. 4.5 shows the implementation of this scattering matrix and the measured reflectivity of an AlGaAs/GaAs epitaxial growth. Usually the epitaxial growth rate fluctuates due to the recess of the material surface or the depletion of the material in the growth system. So the final resultant epilayer thickness is different from the originally designed value. In this case (in Fig. 4.5), the layer thickness is averagely increased by 5% to the original value. After taking this into account, we can calculate the corresponding DBR reflectivity spectrum. As we can observe here, the peak and valley are fitted very well. The abnormal decrease of the measured spectrum in the long wavelength region is an experimental artifact due to the drop of efficiency in the optical grating of the spectrometer and quantum efficiency of the silicon detector.

In a generic vertical cavity device, the thickness of each layer is not just one-quarter wavelength. Many other layers are added in the device because of different reasons, such as the resonant cavity layer or the current spreading layer. The optical simulation still follows the same steps described above, but without the analytical solution of reflectivity of the structure. With semiconductor DBR mirrors present in a device structure, careful design of the cavity length is required such that one can achieve the resonant cavity mode in the “stop” or highly reflecting band of DBR reflectors. In

VCSELs or RCE devices, there will be quantum wells inside the cavity and this resonant mode has to match the quantum well absorption peak to achieve high efficiency in light detection or lasing condition. In the surface micromachined tunable filter, we have an air gap which we can vary during the simulation to see where the resonant mode will sit corresponding to different air gap thicknesses. This will provide a very good estimation for the operating range of any specific device design. Fig. 4.6 demonstrates the simulated reflectivity of the filter which possesses a 5 pairs $\text{Al}_2\text{O}_3/\text{GaAs}$ top mirror and 4 pairs $\text{Al}_2\text{O}_3/\text{GaAs}$ bottom mirror.

4.4 REFRACTIVE INDEX MODEL OF $\text{Al}_x\text{Ga}_{1-x}\text{As}$ SYSTEM

To simulate the reflectivity of the multiple semiconductor layers successfully, there is one more parameter to understand, the exact refractive index of different composition alloys in this materials system. Among all possible semiconductor combinations, the refractive index of the $\text{Al}_x\text{Ga}_{1-x}\text{As}$ system is most important for our applications. The GaAs/AlGaAs materials system has very little lattice constant mismatch, so these two materials can be grown with any combination of composition and thicknesses. Also the high/low refractive index contrast is very large compared to the InP based system. AlGaAs with very high Al content (> 90%) can be oxidized under $\text{H}_2\text{O}/\text{N}_2$ mixture to form Al_2O_3 . The oxidized layer can provide even higher refractive index contrast. These properties make the GaAs/AlGaAs material system a very promising candidate for integrated distributed Bragg reflectors.

There has been considerable research measuring and calculating the refractive index of the GaAs/AlGaAs system[30-32]. The most popular method uses the Kramers-Kronig relationship to calculate the near band edge index from absorption data. From the Kramers-Kronig relationship, we can derive the refractive index from the dielectric constant of the material. When sufficiently far away from the narrow absorption band, Stern pointed out that the real part of dielectric susceptibility is related to photonic energy differences [33]. Since the refractive index, n , is related to dielectric constant by $n^2 = \epsilon(E)/\epsilon_0$, the n below the band gap of the semiconductor can then be represented easily by [32]:

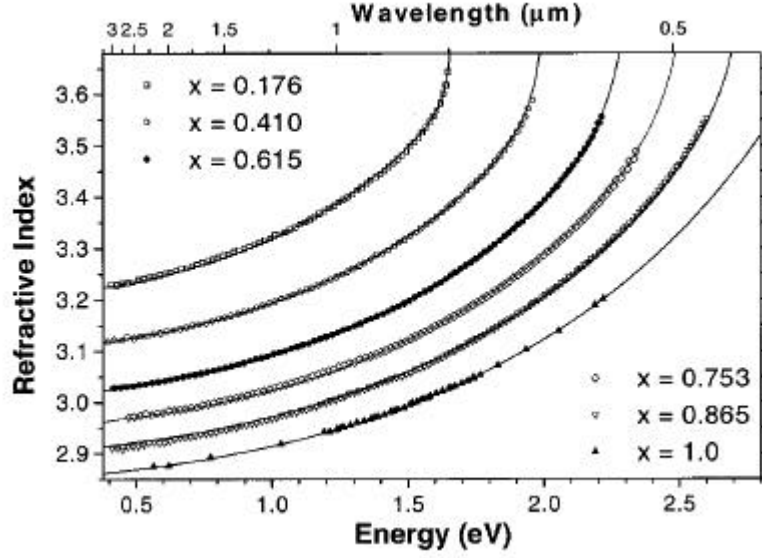


Fig. 4.7: Refractive index dispersion obtained from Gehrsitz et al. [32]. The solid line is the fitting curve from the theory.

$$n^2(x) = A(x) + C_0(x)/(E_0^2(x) - E^2) + C_1(x)/(E_1^2(x) - E^2) + R(x) \quad (4-17)$$

$$R(x) = (1 - x) \times C_2/(E_2^2(x) - E^2) + x \times C_3/(E_3^2(x) - E^2) \quad (4-18)$$

where A , C_i , E_i are determined empirically from the data. C_1 is related to the oscillator strength, E_1 is related to the absorption energy band of the material. Fig. 4.7 shows the illustration from S. Gehrsitz's paper [32] demonstrating very good agreement using this semi-empirical model with measured results.

4.5 THE TWO-DIMENSIONAL CAVITY ANALYSIS

Unless the top mirror is fabricated as a dome shape to collect the light, due to the deformation of the top surfaces, the lightwave is more easily deflected out of the cavity than the ideal cavity, in which the two mirrors are flat. The calculation from the previous chapter can provide a reliable estimation of the surface profile. This bent surface will serve as an input for the optical calculation in this section. We would like to know the

effect of this deformation on additional diffraction loss. In the previous sections, we introduced the scattering matrix theory that can be used to calculate the resonant mode. However, this theory can not be applied to analyze the diffraction loss of the cavity because it assumes the lateral size of the layers to be infinite. The Fox-Li model is used for field distribution calculations. However, to apply this to vertical cavity devices, the Vainhstein waveguide method has to be introduced [34]. We start with a normal cavity with orthogonal eigenvalues and eigenfunctions, we then calculate the walk-off situation using second order perturbation theory of an ideal cavity. Finally a comparison between the experimental and theoretical results will be shown.

4.5.1 Optical Field Distribution – The Fox-Li Model

In modern optoelectronic device design, a cavity formed by confinement of two mirrors is the most common one. This type of device, often called a Fabry-Perot cavity device, comprise most of the optoelectronic devices today, including VCSEL, RCE, distributed Bragg grating devices, etc. In these devices, the optical waves leave one of the two mirrors, travel through the cavity medium, either get absorbed or amplified or scattered and then reach the second mirror. This circulating feature helps to build up the field intensity inside the cavity and enhances the device performance. When these two mirrors are infinitely large, the cavity mode, which is the stable condition for that wavelength of light to exist in the cavity, is very easy to calculate as we showed in the previous scattering matrix section. With two mirrors of limited sizes, Fox and Li [35] showed that a stable optical mode can still exist between them with additional diffraction loss out of the cavity. Their model uses a plane wave going through hundreds of round trips between these two mirrors. At the end of the calculation, the resulting wavefront changes very little from one reflection to the other. This has been widely accepted as a viable solution for real world cavity design [35].

To simplify our problem, we start with a one-dimensional plane mirror. This mirror is infinite in one direction and finite in width in the other direction. As shown in Fig. 4.8(a), from a side view in the y direction, we have a finite cavity formed by these two mirrors. When light hits the second plane mirror, it will get absorbed, diffracted,

reflected or transmitted. Since there's no other structure which will reflect the scattered light back into the cavity, it is reasonable to assume that we have a periodic aperture as shown in Fig. 4.8(b) where the screen is completely absorbing. The lightwave travels through this periodic aperture system and every time it passes through one aperture it is like hitting on one plane mirror in the real cavity. The transmitted lightwave will follow Huygen's principle in the scalar term. The electromagnetic field at one of the apertures can be represented by an integral of the field at the previous one. The Fresnel field, u_p , due to the field in the previous aperture, A, is given by the formula [35]:

$$u_p = \frac{jk}{4\pi} \int_A \frac{e^{-jkR}}{R} (1 + \cos\theta) dS \quad (4-19)$$

where u_a is the aperture field, k is the wave vector, R is the distance from the previous aperture to the next aperture, and θ is the angle which R makes with the unit normal to the aperture.

With every trip, the phase and amplitude of the wavefront are adjusted by the boundary conditions, which are determined by each mirror surface. The wavefront approaches a steady-state shape after a number of round-trips, after which it varies only slightly. When this stage is reached, we call it an optical mode of this cavity. At this point, it is conceivable that the field distribution from one reflection to the next is pretty much the same except for a complex constant, which will be the eigenvalue of this mode in the cavity. In terms of mathematics, the relationship between the q^{th} reflection and $(q+n)^{\text{th}}$ reflection after reaching steady state will look like:

$$u_{q+n} = \gamma^n u_q \quad (4-20)$$

If we substitute eq. (4-20) into eq. (4-19), the final result of the integration equation will be:

$$\gamma u_m(x') = \int_{-a}^a K(x', x) u_m(x) dx \quad (4-21)$$

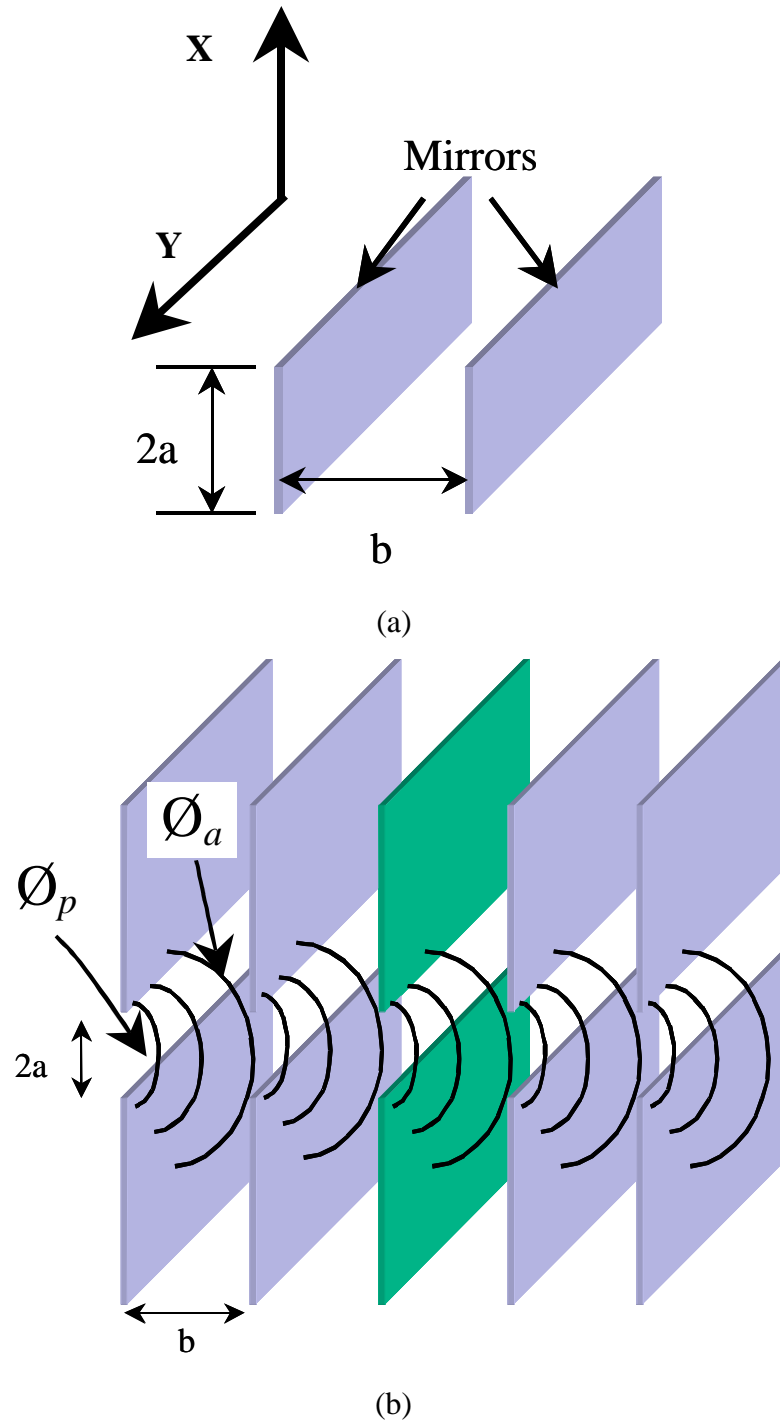


Fig. 4.8: Illustration of basic conception of the Fox-Li model: (a) two semi-infinite plane mirrors with width a form a one-dimensional cavity. (b) the resonating phenomenon can be depicted as a series of optical apertures lining up with optical waves propagating through each aperture following the Huygen's principle.

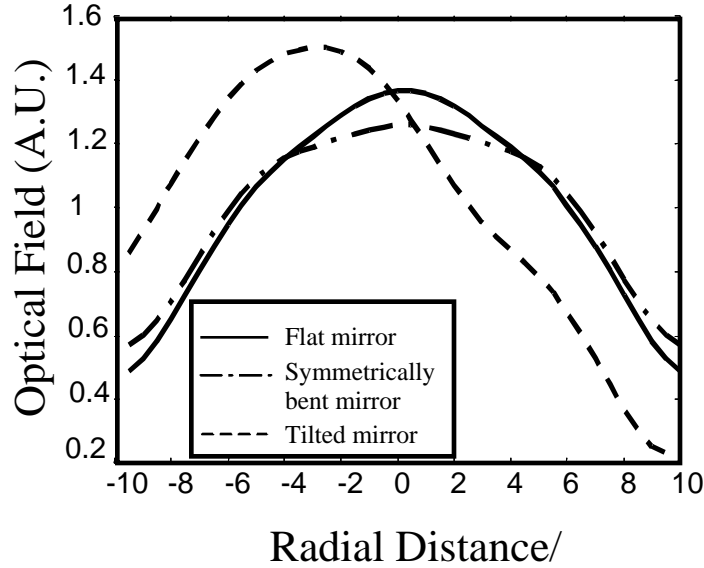


Fig. 4.9: Optical field distribution using Fox-Li's model for calculation.

where the m indicates the m th mode of the cavity. The $K(x',x)$ term is the combination of phase and radiation formula in the eq. (4-19). Fig. 4.9 shows the Fox-Li calculations for a deformable membrane with 0.01 maximum displacement from the perfectly-aligned case as well as the tilt mirror case for comparison. The size of the mirror is 20×20 , and the cavity length is 100. The plot clearly demonstrates that the introduction of symmetric deformation does not shift the mode position, while tilting the mirror causes such a shift.

4.5.2 Modes in an open resonator with high Fresnel number

Fox & Li's method is powerful when used for low Fresnel numbers, N , defined as $(\text{half of the mirror width})^2 / (\lambda \times L_{\text{cav}})$, typically less than 20 [36]. For vertical cavity devices, the Fresnel number can be as high as 100 because of the inherent short cavity. Under this condition, Fox & Li's method has to be modified using a complicated Kirchhoff integration (or near-zone field integration), but beating between the two lowest modes makes the iteration procedure inefficient [35]. A simpler method for large N is to use the asymptotic behavior of a waveguide to derive the eigenfunctions or eigenvalues of open resonators[34;37]. The theory is based on the fact that existing modes behave like

guided waves with frequency slightly higher than the critical frequency. Such waves do not leak at the open end of the resonator. On the contrary, most of the energy is reflected back into the waveguide. The resultant eigenfunctions and eigenvalues for a semi-infinite plane mirror set with width, a , can be formulated as [34]:

$$\begin{aligned} \psi_m(x) = & \begin{cases} \cos\left(\frac{m\pi x}{2a[1 + \beta(1+i)/M]}\right) & m = 1,3,5,\dots(\text{even}) \\ \sin\left(\frac{m\pi x}{2a[1 + \beta(1+i)/M]}\right) & m = 2,4,6,\dots(\text{odd}) \end{cases} \end{aligned} \quad (4-22)$$

$$\gamma_m = \exp\left(\frac{i\pi^2 m^2}{2[M + \beta(1+i)]^2}\right) \quad m = 1,2,3,4,5,\dots \quad (4-23)$$

where $\beta = 0.824$ is a constant, $M = \sqrt{8\pi N}$ and N is the Fresnel number. The normal diffraction loss of the plane mirror cavity will be $1 - |\gamma_m|^2$, which decreases exponentially with decreasing cavity length.

When the mirror is of finite dimension, the eigenfunctions and eigenvalues of this cavity are simply products in the following form [34]:

$$\psi_{mn}(x, y) = \psi_{mx}(x) \psi_{ny}(y) \quad (4-24)$$

$$\gamma_{mn} = \gamma_{mx} \gamma_{ny} \quad (4-25)$$

where ψ_{mx} , ψ_{ny} , and γ_{mx} , γ_{ny} are in the same forms shown in the previous semi-infinite case.

4.5.3 Optical Diffraction Loss from Second Order Perturbation Theory

Once the eigenfunctions and the eigenvalues are known, the extra diffraction loss can be calculated. The eigenvalue of the specific mode, m , is the ratio between the successive reflection waves, so $|\gamma_m|^2$ is the difference of these two reflections. The power loss caused by this reflection will then become $1 - |\gamma_m|^2$. When there is a small

imperfection in the mirror alignment or mirror surface, the diffraction loss can also be calculated based

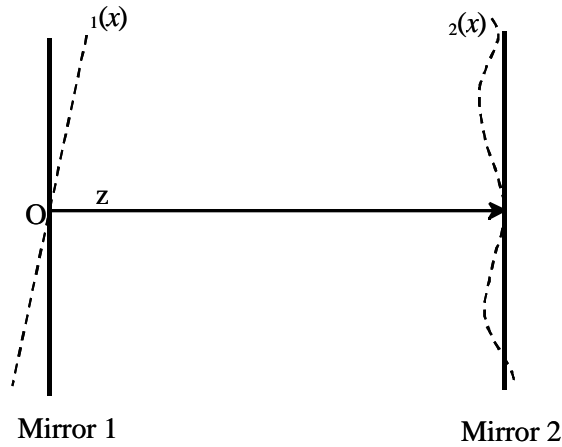


Fig. 4.10: The perturbed Fabry-Perot resonator with phase variation

on the ideal mirror eigenvalues. The modification caused by this deformation can be estimated by second-order perturbation theory [26;38-40]. We assume a semi-infinite mirror in one direction and further assume that the deformation is small enough (as shown in Fig. 4.10, two mirrors are tilted at in some small angles, ϕ_1, ϕ_2 respectively.) such that the integral equation in Fox & Li can be rewritten as [38]:

$$\gamma_m \psi_m(x) = \exp[i(\phi_1(x) + \phi_2(x))] \int_{-a}^a K(x, x') \psi_m(x') dx' \quad (4-26)$$

where γ_m is the new eigenvalue, ψ_m is the eigenfunction, $\phi_1(x)$ and $\phi_2(x)$ are the phase change due to mirror deformation and K is the integral kernel. In general, $\phi_{1,2}(x)$ can be expressed as (wave vector) \times (deformed surface profile). Since $\phi(x)$ is very small, the integral equation can be linearized by taking a Taylor's series expansion of $\exp(i\phi(x))$, eigenvalues γ_m , and eigenfunctions ψ_m .

$$\begin{aligned} \exp(i2\phi) &= 1 + i(\phi_1 + \phi_2) - \frac{(\phi_1 + \phi_2)^2}{4} \dots \\ \gamma_m &= \gamma_m^{(0)} + \gamma_m^{(1)} + \gamma_m^{(2)} \dots \\ \psi_m &= \psi_m^{(0)} + \psi_m^{(1)} + \psi_m^{(2)} \dots \end{aligned} \quad (4-27)$$

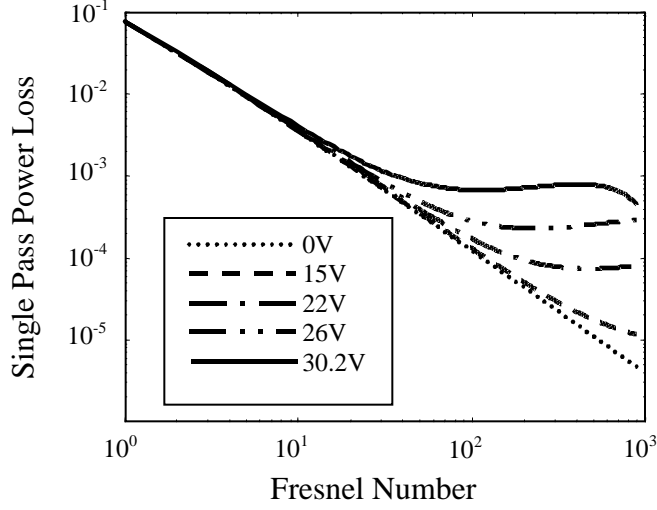


Fig. 4.11: Single pass power loss versus applied tuning voltage. The loss is increasing towards the larger bending.

If we substitute the terms in the original integral equation (eq. (4-26)) with equation (4-27) and then multiply a different mode, ψ_n , to both sides of this equation, the integration on both sides will eliminate some terms due to the orthogonality between the modes of the cavity. In our case, one of the mirrors can be treated as flat because it is the substrate bottom mirror, while the deformable mirror is the movable top mirror. β_1 will become the wave vector times surface profile of the top mirror, while β_2 will be zero. Using the expression we developed previously and applying general second-order perturbation theory, the relationships among the zero-, first- and second- order corrections of the eigenvectors can be found as [39]:

$$\gamma_m^{(1)} = i\gamma_m^{(0)} \langle \psi_m | \hat{H} | \psi_m \rangle \quad (4-28)$$

$$\gamma_m^{(2)} = \gamma_m^{(0)} \left[\frac{\langle \psi_m | \hat{H}^2 | \psi_m \rangle}{2} - \langle \psi_m | \hat{H}^2 | \psi_m \rangle + \sum_n \frac{\langle \psi_m | \hat{H} | \psi_n \rangle \langle \psi_n | \hat{H} | \psi_m \rangle}{1 - \gamma_m^{(0)}/\gamma_n^{(0)}} \right] \quad (4-29)$$

where \hat{H} is the non-zero β_1 we mentioned above and the brackets represent the symmetric operator similar to the Hermitian operator in quantum mechanics.

The single-pass total power loss is then $1 - |\gamma_m|^2$. With the deformation profile of the top membrane solved in the previous chapter (Fig. 3.14), we can input it into the second order perturbation model to calculate the diffraction loss under different tuning bias. Fig. 4.11 shows the power loss per transit versus Fresnel number, N , under different bias. We can clearly observe that higher tuning voltage causes more bulging of the loss curve and when the applied tuning voltage is too large, the curve will diverge because of the failure of second order perturbation from the large displacement of δ . For the two-dimensional case, the eigenfunction can be treated as two independent cosine functions in x and y , respectively. The eigenvalues will then become the multiplication of γ_{0x} and γ_{0y} , as described in the previous section. In our devices, because the plate is square, for the lowest order mode, $\gamma_{0x} = \gamma_{0y} = \gamma_0$. So the final power loss will be $1 - |\gamma_{0x}|^2 |\gamma_{0y}|^2 = 1 - |\gamma_0|^4$.

4.6 COMPARISON WITH EXPERIMENTAL RESULTS

The single transit power loss we calculated is not an easily measurable physical quantity and we have to find a method to quantify it. One way is to measure the linewidth broadening of passive devices. The linewidth of passive optoelectronic devices is usually determined by the finesse of the cavity, in which the loss of the cavity plays an important role. The deformation of the top mirror introduces extra diffraction loss in the cavity. Once we have information about the deformation of the membrane, the optical diffraction loss can be calculated from equation (4-26) and (4-27). This power loss is attributed to the air gap between the top and bottom mirrors and will presumably broaden the linewidth of spectral responses. In our resonant enhanced structure, the linewidth is calculated as [29]:

$$\lambda_{1/2} = \frac{\lambda^2}{2\pi \times n \times L_{cav}} \frac{1 - \sqrt{R_1 R_2} \times (\text{mirror loss})}{(R_1 R_2)^{1/4} (\text{mirror loss})^{1/2}} \quad (4-30)$$

where λ is the wavelength of the resonant cavity, n is the refractive index of the cavity (which is 1 in this case.), L_{cav} is the effective length of the cavity, and R_1, R_2 are the top and bottom reflectance, respectively. The mirror loss is the value calculated from second

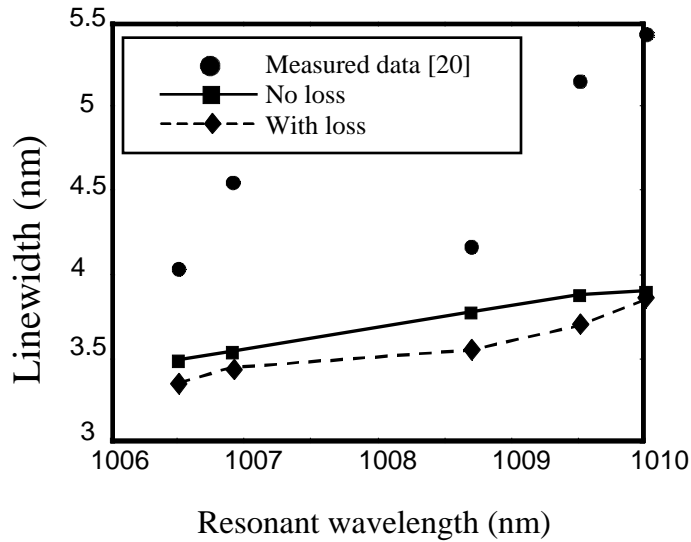


Fig. 4.12: Comparison between the theoretical calculation and experimental results of linewidth broadening of tunable phototransistors.

order perturbation theory. Eq. (4-30) is just an estimation of the extra diffraction loss caused by the deformation of the top mirror. Other sources of broadening, such as free carrier absorption are not included.

Fig. 4.12 shows the calculated result with and without deformation loss. As the plot shows, the diffraction loss caused by deformation of the central plate is limited but not negligible (about 3%). In our devices, the linewidth of the spectral response does not suffer from deformation, while the results from other group [4], had significant broadening (four times) in the spectral response due to a larger membrane deformation. The discrepancy between experiments [41] and calculation indicates that other factors, such as growth errors and free carrier absorption due to high doping might also play important roles in reducing the cavity finesse.

4.7 SUMMARY

We reviewed the transmission matrix theory for the calculation of the resonant wavelength of multiple layers of semiconductor at the beginning of this chapter. This method can not estimate the diffraction loss caused by the finite size of actual devices. To calculate this, the Fox-Li model is a very useful algorithm to evaluate the transverse field

and diffraction loss of the Fabry-Perot cavity. However, the nature of high Frenel numbers of the vertical cavity devices force us to use second order perturbation theory because of the inefficiency of the Fox-Li method in this realm. This method, combined with the linewidth calculation, can predict the theoretical broadening caused purely by the top membrane deformation. From a comparison between the experimental and theoretical results, it is clear that the deformation in our devices is small, but not negligible and other factors play important roles. The effects and controllability of these factors, such as growth error and dopant absorption, will be discussed in the next chapter.

Chapter 5 Material growth and fabrication of tunable optoelectronic devices

5.1 INTRODUCTION

The previous chapters dealt with the theoretical part of the device design. We now have to fabricate these devices. This chapter will cover a basic introduction of the material growth, device fabrication processes. Measurements of the mechanical and optical properties of the wavelength tunable optoelectronic devices will be discussed in the next chapter.

The materials growth of the device is very crucial to the whole procedure for tunable devices, although these procedures are pretty much well-known in today's technology. Different growing technology can affect the performance of the devices greatly. The quality of the multiple layers of semiconductor has to be controlled. The smoothness and sharpness of the interfaces will affect the reflectance of the mirror pairs and the cavity length. With the introduction of vertical cavity devices, the thickness of each layer becomes far more important. Different methods have been proposed to monitor or control the growth rate. The source materials that are used during growth also play important roles. Various problems associated with the crystal growth will be discussed in this chapter.

After the growth, the whole wafer will be processed using various chemical or ion plasma ion etches with proper photoresist masking layers. These processes will define the geometry and layout of the targeted structures. Also some thin film and metal depositions are necessary to provide suitable built-in stress and electrical contacts. Although most of the procedures are standard, the integration of them is a tedious task and there are significant challenges to increase the yield of such devices in a the real production line environment.

5.2 MATERIAL GROWTH

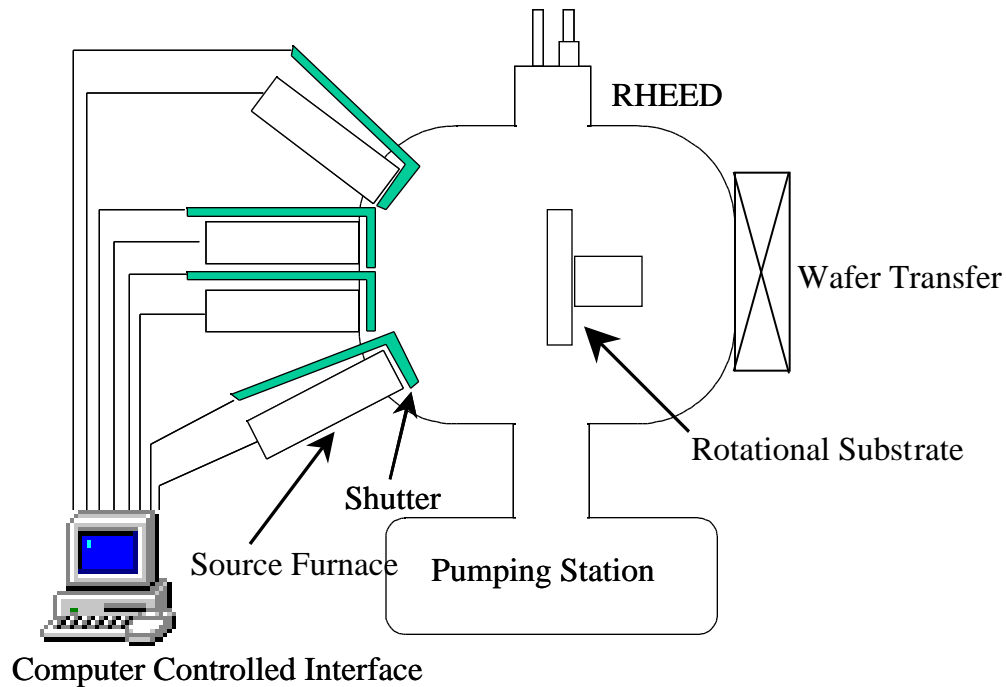


Fig. 5.1: Schematic Diagram of a MBE system.

During the last half of the century, a number of materials growth technologies have been invented and commercialized. Every time a new materials growth technique has been deployed, device innovation and fabrication advances to another higher level. As device structures have become ever more and more elaborate, the growth techniques face ever greater challenges. The invention of quantum well structures pushed the materials growth technologies toward their ultimate limits where layer thickness is reduced down to the atomic scale with atomic scale interface abruptness and smoothness with similar requirements for surface morphology. Two main technologies have arisen for this latest task: molecular beam epitaxy (MBE) and metal organic chemical vapor deposition (MOCVD). Between these two, we have chosen MBE technology because it provides sharp atomic level interfaces and the source material of MBE is safer than that of MOCVD's.

Fig. 5.1 shows a generic MBE schematic diagram. The MBE system consists of an ultra-high vacuum chamber (usually 10^{-10} to 10^{-11} torr), several furnaces, non-oil based high vacuum pumps, a RHEED system, and system sample transferring mechanism. The individual material sources are high purity elements (Ga, Al, In, As, etc.) contained by

PBN crucibles in the furnaces which are attached to this chamber. When the source temperature is elevated, the source materials evaporate as atomic or molecular beams to reach the substrate in the center of the chamber. The ultra-high vacuum provides a long mean free path for

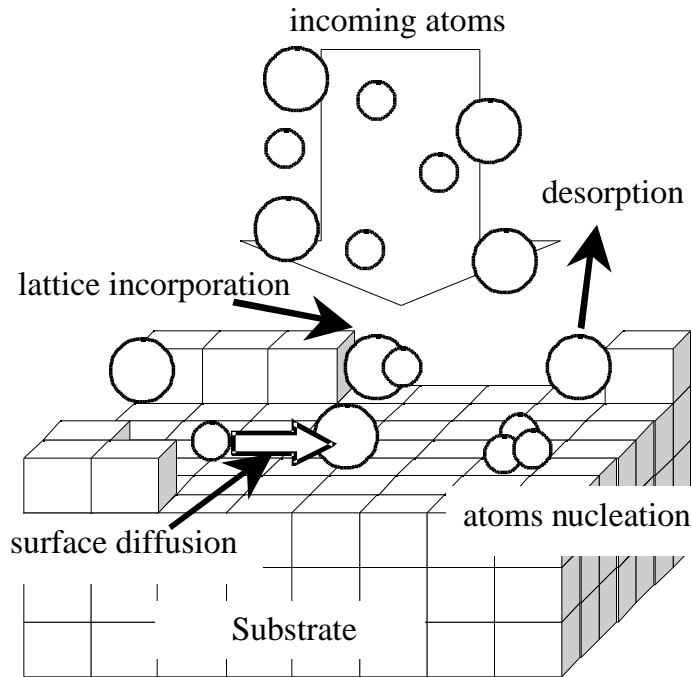


Fig. 5.2: Illustration of surface chemistry of the MBE growth

particles and this ensures the evaporated materials reach the substrate surface without any collisions or chemical reactions. The temperature of the furnace determines the evaporation rate of the material and thus the growth rate. The substrate temperature is set such that the arriving species have good surface mobility and find an appropriate lattice site where surface chemical reactions occur between will happen when particles on the surface (for example, As and Ga atoms combine to form GaAs). Fig 5. 2 illustrates the surface processes that take place during the growth [42]:

- (a) *adsorption* of the constituent atoms or molecules impinging on the substrate surface,
- (b) *surface migration* and *dissociation* of the adsorbed molecules,
- (c) *incorporation* of the constituent atoms into the crystal lattice of the substrate or the epilayer already grown,

- (d) *thermal desorption* of the species not incorporated into the crystal lattice.

When the substrate temperature is not in the correct range, surface segregation and three-dimensional growth will occur. The shutters in front of the source furnaces and the growth rate of the sources will control the layer structure thickness and composition. The shutter controls whether the species appears in a particular layer. The growth rate controls both the composition and the thickness of the layer. Usually there is an overpressure of group V elements to control the relative populations of chemisorbed group III and V precursors [43] and the growth rate of the layer is determined solely by group III material arrival. If several group III species are present at the same time, the total growth rate of the layer is the algebraic sum of each individual species because each has unity sticking coefficient and there is virtually no interaction between them with an excess column V flux. These can be interfaced to a computer through GPIB interface cards and the whole growth can be programmed and controlled automatically. The source materials used in our Varian Gen-II MBE system are Al, Ga, In and As. The dopant materials are Si for n-type and Be for p-type.

The substrate temperature influences all aspects of the epitaxial crystal growth and quality, including the incorporation and redistribution of impurities, deep levels and lattice defects [43]. These will in turn effect the electrical and optical properties of the grown epitaxial layers. Dopant incorporation can also be a strong function of substrate temperature, effecting re-evaporation, surface segregation, site incorporation and precipitation of dopant atoms. In our MBE system, beryllium and silicon are used for p-type and n-type dopants, respectively. To have a high beryllium doping concentration, the substrate temperature has to be lower (around 480 °C to 520 °C). Beryllium concentration control can be quite precise in both low and high doping, unlike its carbon counterpart. However, the redistribution of high concentration Be ($> 5 \cdot 10^{19} \text{ cm}^{-3}$) means Be diffuses out of the original grown region. This has long been a serious problem for heterojunction bipolar transistors [44]. The solution to prevent this from happening is to either lower the substrate growth temperature or use high As₄ overpressure to suppress the out-diffusion problem [45]. Other methods also include introduction of In in the layer [46] and growth on a GaAs wafer with different orientation like (311)A which can

suppress this redistribution because of its larger surface step density [47]. Si is an amphoteric dopant, which tends to occupy the gallium sublattice on a GaAs (100) surface for a very wide range of growth conditions [43]. The highest achievable electron concentration is around $7 \cdot 10^{18} \text{ cm}^{-3}$.

While the quality of the epitaxial layer affects both the optical and electrical properties of the devices, another important factor is the thickness of each layer. Thickness is particularly critical if there is any difference in lattice constant between layer and substrate or where electronic states or optical modes are determined by layer thickness. Our devices use distributed Bragg reflectors (DBRs) as the mirrors, hence the thickness of each layer must be quite precisely a quarter lambda (0.25λ) to achieve the maximum reflectivity condition. Also the length of the resonant cavity is determined by the thickness of the central cavity layer. Thus growth rate and its control are very important issues to understand during MBE operation, which we explore next.

5.3 IN-SITU GROWTH CALIBRATION

Usually we can observe the output flux of the pre-heated material source with an ion gauge in the substrate position to determine the growth rate. This method gives a good estimate during short growth periods. However, when the growth is extended to ten or twenty hours, the growth rate will drift away from the originally set value due to the recession and the change in the shape of the source material surface on the PBN crucibles. The first in-situ measurements and layer thickness corrections used optical reflectivity and computation during a growth interruption [48]. Subsequently real-time laser interferometry has been developed to monitor the growth of each epitaxial layer through the periodic variation of the reflected laser signal [49;50]. However, this method requires almost perfect alignment of the substrate holder to ensure normal incidence of the laser beam, which means no wobbling during rotation, and no vibration of the system. These two constraints make this method difficult for practical implementation. We utilize the former way to monitor the grown structure by measuring the optical reflectivity as a function of wavelength at various stages of the growth. Unfortunately this method requires a break in the growth sequence and pulling the wafer out of the growth chamber to make the measurement. This takes more time; however, the accuracy is high. The

measured reflectivity can be matched by the transmission matrix calculation result described in the previous chapter. Once we find the deviation in growth rate, suitable adjustment is made to the growth rate settings and a new phase-matching layer is added to adjust the resonant cavity mode to exactly the desired wavelength. The only concern using this method is that during the reflectivity measurement, the surface of the wafer can become oxidized if the measurement chamber is

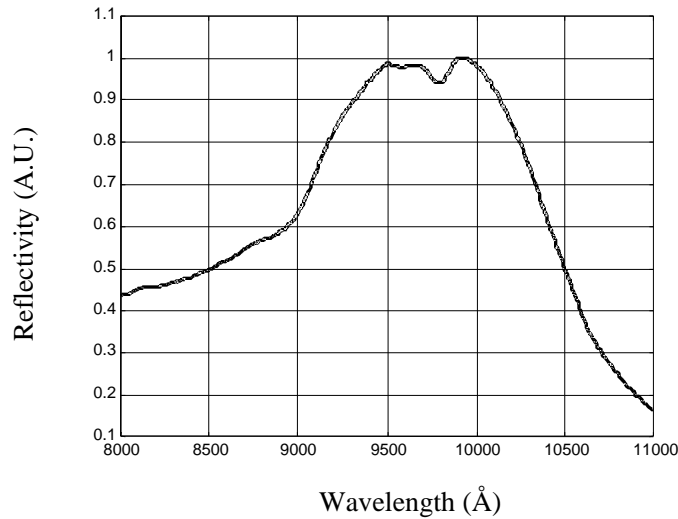


Fig. 5.3: The reflectivity of the multiple InGaAs quantum wells sample with GaAs barrier and background. The dip around 970nm is from the absorption peak of the quantum wells.

Under ultra-high vacuum, particularly if an AlAs layer is exposed. We can easily solve this problem because our measurement chamber reaches the same vacuum level as the growth chamber. Also an additional oxide blow-off under As overpressure is provided at the beginning of each stage to ensure the cleanness of the surface.

The multiple quantum well samples are calibrated using the strong exciton peak at room temperature which is easily measured by our white light reflectance method. Fig. 5.3 shows the reflectivity of a multiple InGaAs quantum well sample with GaAs barriers. The reflectance thus becomes that due to GaAs plus the absorption peak of the multiple quantum wells. In the following growth we then use this peak as a standard to match the cavity mode with the exciton peak of the quantum well. With this technique, we have successfully demonstrated the surface micromachined VCSELs [17;51;52]

Fig. 5.4 (a) to (c) shows the general outcomes of this method during a tunable vertical cavity device growth. In Fig. 5.4 (a), a 10-pair of DBR is grown and measured. The fitted line is calculated by the scattering matrix theory introduced in the previous

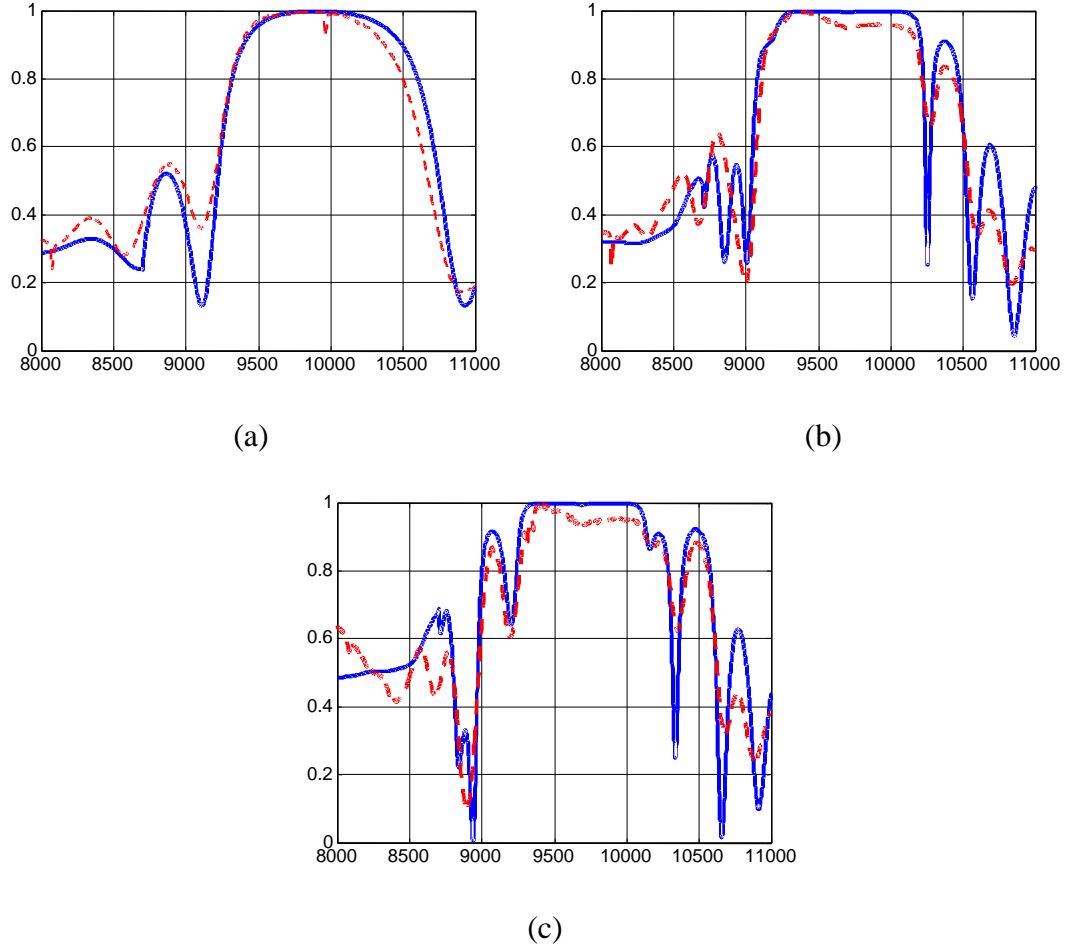


Fig. 5.4: The in-situ reflectivity plots of the tunable devices: (a) after 10 pairs of DBR grown; (b) after the main cavity grown; (c) fully finished wafer. The solid line is the calculation and dash line is the measurement.

section. Fig. 5.4 (b) is after the second stage of growth where the rest of the bottom DBR pairs, the central Fabry-Perot cavity plus the first two pairs of the top DBR have been grown. Since the top structure is not yet totally grown, we can adjust the cavity mode at this stage. Fig. 5.4 (c) shows the reflectivity of the completed device and as we can see, the cavity mode and layer thickness can be quite precisely fitted to prediction. From processing a number of wafers, we find that this thickness measurement and correction procedure generally quite accurate.

5.4 DEVICE FABRICATION

A simplified tunable device process flow is illustrated in Fig. 5.5. After growth, the sample is wet-etched to expose the $\text{Al}_{0.97}\text{Ga}_{0.03}\text{As}$ layers, which are then oxidized in an ambient of $\text{H}_2\text{O}/\text{N}_2$ mixture at 440°C for 18 minutes [53]. Only the central part of the $\text{Al}_{0.97}\text{Ga}_{0.03}\text{As}/\text{GaAs}$ layers are left for oxidation to reduce the thickness of the supporting legs. This approach, as first developed by F. Sugihwo[25], can efficiently decrease the stiffness of the legs without affecting the reflectivity of the DBR stack. Ti/Au is deposited and lifted off to form top p-type electrical contact pads. Several thousand Angstroms of high tensile Si_3N_4 are deposited put down by plasma enhanced chemical vapor deposition (PECVD). A RIE dry etch is used to define the membrane pattern and expose the $\text{Al}_{0.85}\text{Ga}_{0.15}\text{As}$ sacrificial layer. The bottom n-type contact is made by evaporating $\text{Au}/\text{Ge}/\text{Au}$ followed by rapid thermal annealing (RTA). Finally, the sacrificial etch layer of thickness 9800 \AA is removed in $\text{HCl}/\text{H}_2\text{O}$ solution to release the membrane. Fig. 5.6 shows a SEM micrograph of the released devices. The air gap and the shadow can be clearly observed. A more detailed list of all process steps and parameters is described in Appendix A.

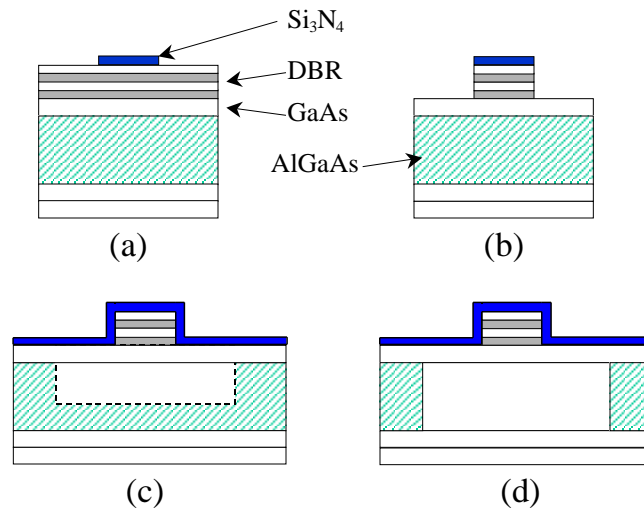
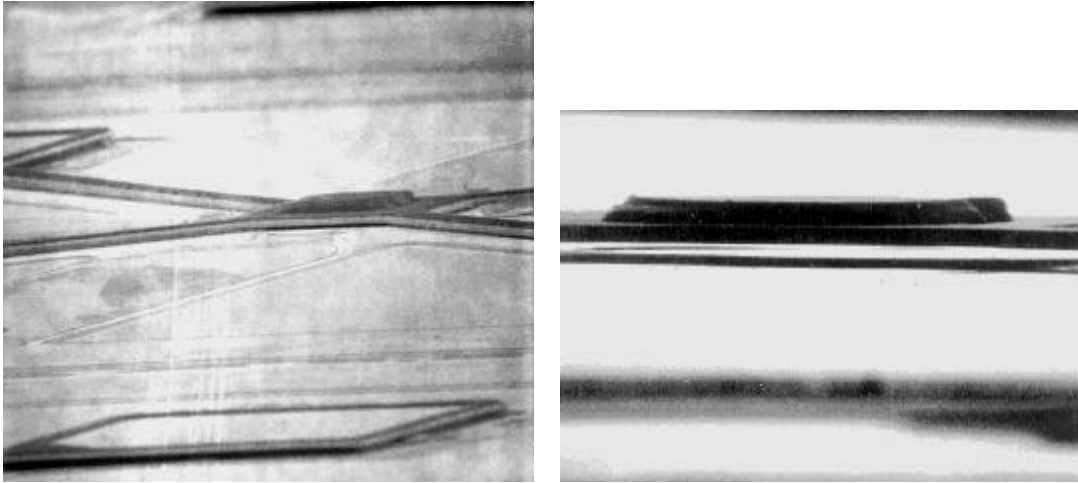


Fig. 5.5: Simplified process flow of the tunable devices: (a) pattern the central membrane; (b) etch away the unwanted mirror material; (c) deposit the silicon nitride and partially etch the sacrificial AlGaAs layer for electrical contacts; (d) fully release of the membrane.



(a)

(b)

Fig. 5.6: The SEM micrograph of the successfully released tunable membrane: (a) the whole view of the tunable structure with four supporting legs and the central membrane; (b) the close-up view of the central membrane, the shadow underneath the membrane indicates the full release of the process.

Chapter 6 Surface Micromachined Wavelength Tunable Optoelectronic Devices

6.1 INTRODUCTION

Surface micromachining technology has been available for more than 10 years. In the past, research focused on the change of optical path length that the movable component brought into the design. Various applications, like adaptive optics, anti-reflection switches, etc. utilized this powerful approach to change the phase of an incoming lightwave by individual pixels to either correct the phase aberration[15] or transmit/reflect the desirable wavelength of the signal[54]. With the emerging needs of Internet data traffic, wavelength division multiplexing (WDM) became the best solution to increase bandwidth without changing the existing optical fiber infrastructure. Wavelength tunable optoelectronic devices based on surface micromachined technology are becoming important elements for WDM communication systems because of their wavelength agility and versatility. Several results have been reported, including lasers[17;19;55;56], detectors[16;57;58], and filters[4-7;59]. These devices can be categorized into 2 general structures: (a) four-leg style deformable membrane, and (b) one-leg style cantilever. Although the cantilever approach provides lower actuation voltage and easier fabrication processes than the four-leg structure, the cavity mode performance, as we illustrate later in this chapter, is poorer than the membrane structure. Our group has focused on the four-leg membrane style devices and the remainder of this thesis describes our research efforts.

Most of the devices in the four-leg style design, as shown in Fig. 6.1, use a dielectric material for the top DBR mirror because such dielectric materials like $\text{SiO}_2/\text{Si}_3\text{N}_4$ have a larger index of refraction and thus greater DBR bandwidth of the high reflectivity region compared to semiconductor DBRs. However, the dielectric deposition conditions are quite critical and sometimes difficult to predict. These layers play a critical role because different dielectric materials and deposition conditions effect the compressive/tensile stresses which have to be balanced in order to have enough tension

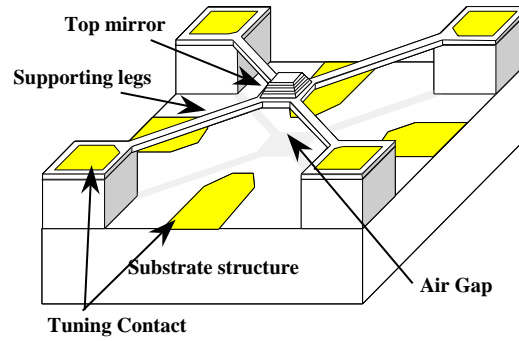


Fig. 6.1: A generic surface micromachined tunable structure.

during the release steps of the fabrication processes to prevent membrane collapse. These all cause many practical problems for the dielectric DBR pairs. To overcome this, we developed an $\text{Al}_2\text{O}_3/\text{GaAs}$ DBR as a replacement[60]. $\text{Al}_2\text{O}_3/\text{GaAs}$ has a very large refractive index contrast while thickness control is comparably easy because it is controlled by MBE deposition. The only dielectric needed in this design is the tensile stressed silicon nitride. Since only a single tensily stressed layer is utilized in the microstructure, the survival rate of the release step is greatly enhanced. In this chapter, we discuss both dielectric mirrors and $\text{Al}_2\text{O}_3/\text{GaAs}$ mirrors as they are important players in the evolution of surface miromachined tunable devices. First the tunable devices results based on the dielectric top DBR will be introduced. They will include the parameter extraction techniques developed for tunable VCSELs, tunable photodiodes and phototransistors. The second part of the chapter focuses on implementation of the $\text{Al}_2\text{O}_3/\text{GaAs}$ DBR to a tunable filter. Both mechanical and optical measurements will be demonstrated. As we demonstrate, the $\text{Al}_2\text{O}_3/\text{GaAs}$ DBR significantly improves both device fabrication and performance.

6.2 DIELECTRIC TOP MIRROR TUNABLE DEVICES

All the top mirrors of the first generation tunable devices were made with dielectric material plus conducting metal layers. These devices are very mature in turns of the fabrication processes. In this section, we describe new measurement approaches to characterize the device parameters of tunable devices. First, we used a tunable VCSEL for extraction of some important semiconductor laser parameters. Second, we developed

two tunable photodetection schemes: PIN diodes and phototransistors. The former has the benefit of integration with VCSELs because of the duality of the PIN device. The phototransistor can amplify the absorbed optical signal to increase the detection margin. The results from experiments and theory will be compared. All these devices are well understood such that they are ready for general device applications.

6.2.1 Tunable VCSEL and parameter extraction

As mentioned previously, there has been much research focused on tunable VCSELs. The importance of this key device is that it provides an easier way to implement system provisioning. It can also make the system more agile. Besides these functions, wavelength tunable VCSELs can be used as an important device to measure the internal parameters of the VCSEL itself, which is very difficult for fixed wavelength VCSELs. The dependence of external quantum efficiency upon mirror loss is generally used to extract the parameters of laser diodes. The expression used is:

$$\eta_{ext} = \eta_i \frac{\alpha_m}{\alpha_i + \alpha_m} \quad (6-1)$$

where η_{ext} is the measured external quantum efficiency, η_i is the internal quantum efficiency, α_i is the internal loss, and α_m is the mirror loss. From a plot of $1/\eta_{ext}$ vs. $1/\alpha_m$, we can then determine η_i and α_i from the slope and the intercept of curve, respectively.

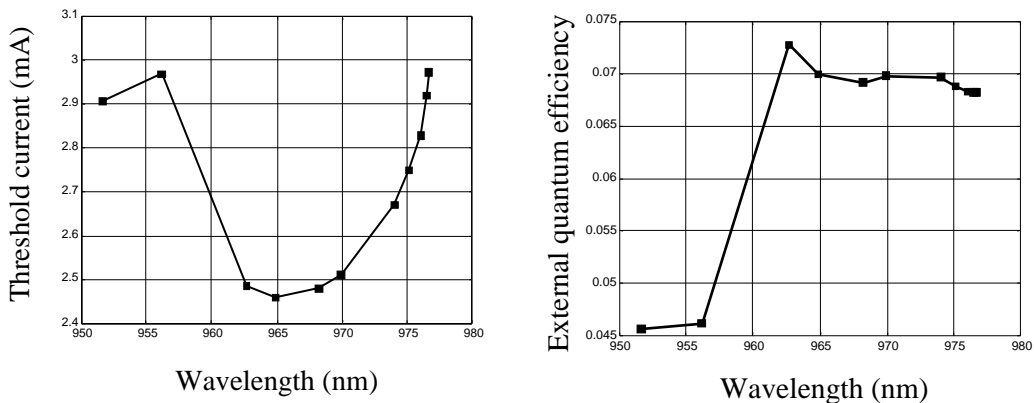


Fig. 6.2: The threshold current and external quantum efficiency versus the tuning wavelength.

For edge emitting lasers, this method is readily straightforward using various cavity lengths, L , made by cleaving the wafer stripes into different lengths. For Vertical Cavity Surface Emitting Lasers (VCSELs), because the cavity length is predetermined once the epitaxial layers are grown, implementation of this method is not straightforward. Yang, et.al. [61] changed the reflectance of the top Distributed Bragg Reflector (DBR) by systematically etching away mirror pairs and measuring the resulting change in η_{ext} . Under the assumption that cavity length does not vary, a plot of equation (6-1) can be made and the parameters can be extracted. This method is not only very time consuming, but subject to differences between individual devices and errors of under or over etching slightly in the removal of exactly 1 mirror pair in the DBR.

In this section, we describe a new method of extracting laser diode parameters using a tunable VCSEL structure [51]. The advantage of this method is that we do not need to fabricate different VCSELs. The parameters can be measured from the same laser diode such that differences caused by growth nonuniformity can be eliminated. The tunable VCSEL is similar to that shown in Fig. 6.1. When an electrostatic bias is applied between the membrane and top semiconductor surface, the width of the air gap is reduced, causing a change in the effective cavity length which shifts the lasing wavelength [19]. The external quantum efficiency

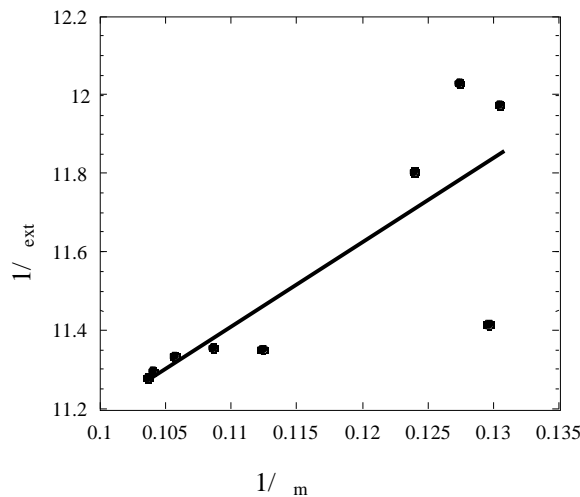


Fig. 6.3: Inverse of external quantum efficiency vs. inverse of mirror loss.

can be measured and used for extraction of internal loss and internal quantum efficiency.

The device illustrating this process was grown using a Varian GEN-II MBE. The hybrid dielectric top mirror consists of 1/4_ GaAs, stress-matched SiO₂/Si₃N₄/SiO₂ trilayer and 1500Å gold. The air gap thickness is slightly greater than 3/4_0 and the air gap acts as part of the top mirror. This device is designed as the semiconductor-extended cavity style [51]. The device tunes 25 nm, going from 976.64 nm to 951.68 nm. AlAs oxidation is used to create an 18 _m current diameter aperture [53;62]. From the L-I curve under different membrane bias, the extracted external quantum efficiency and threshold current vs. lasing wavelength are plotted in Fig. 6.2. Because the air gap thickness is 0.87 _0 at zero bias, the threshold current decreases until the gap reaches 0.75 _0, which corresponds to the peak resonance condition. Beyond this point, the threshold current again rises. The external quantum efficiency has been corrected by the ratio between the output power from the bottom mirror and the total output power as described in [26]:

$$\frac{P_{bot}}{P_{total}} = \frac{1 - R_{bot}}{(1 - R_{bot}) + (1 - R_{top})\sqrt{R_{bot}/R_{top}}} \quad (6-2)$$

We neglect the last 2 data points in Fig. 6.2 because of the mode switching [51]. Fig. 6.3 shows the dependence between 1/_ext and 1/_m. From the intercept and slope of the data in Fig. 6.3, the extracted internal loss _i is 2.36 cm⁻¹, and the internal quantum efficiency is 11%.

Knowing _i, the relationship between mirror loss and threshold current density can be used to calculate the transparency current density, J_{tr}, and the average logarithmic gain coefficient, g₀, as shown in the following equations:[63]

$$g_{th} = g_0 \ln\left(\frac{\eta_i J_{th}}{n_w J_{tr}}\right) \quad (6-3)$$

$$\ln(J_{th}) = \ln\left(\frac{n_w J_{tr}}{\eta_i}\right) + \frac{\eta_i \alpha_m}{g_0 \eta_{ext}} \quad (6-4)$$

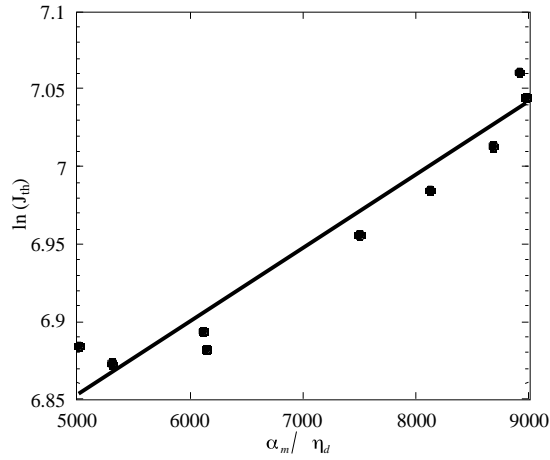


Fig. 6.4: Logarithm of threshold current density vs. the normalized mirror loss.

Plotting $\ln(J_{th})$ vs. α_m / η_d , we can extract J_{tr} and g_0 using curve fitting as shown in Fig. 6.4. The result shows that $J_{tr} = 41.22 \text{ A/cm}^2$, and $g_0 = 2317.05 \text{ cm}^{-1}$, which are close to those values reported in [61].

From the results, we find that η_i is very small compared to the 40-80 % values reported for the best VCSELs. Such data provides insight into the device structure. We believe this low efficiency is caused by the additional non-radiative leakage current running through the four membrane posts supporting the tunable membrane. This leakage current is caused by incomplete conversion of AlAs into Al-oxide. Further experiments are underway to investigate the magnitude of this leakage.

To sum up, we have demonstrated a novel technique using a tunable VCSEL structure to easily measure the important laser parameters. Good agreement is found with literature values except for internal quantum efficiency. These measurements provide information on the device structure, which in this case is a high leakage current due to incomplete oxidation of the AlAs layer underneath the membrane posts.

6.2.2 Tunable PIN photodiode

Tunable photonic detection can be easily achieved by reverse-biasing the tunable VCSEL. This turns the original VCSEL into a PIN photodiode. When the light penetrates

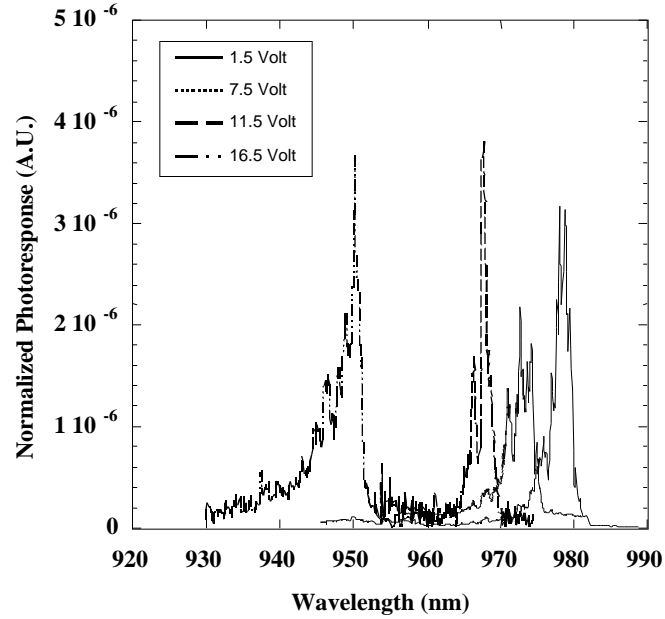


Fig. 6.5: The photocurrent spectrum of tunable PIN diode under different tuning bias.

into the cavity, the photons are absorbed by quantum wells in the device and this can generate an electron - hole pair. This electron-hole pair is pulled apart by the reverse electric field applied across the PIN junction and creates a photocurrent. The duality of this device is very attractive for systems integration. With proper designs in devices and driving circuits, one tunable unit can serve both the laser source and receiver nicely. The plot in Fig. 6.5 shows the narrow linewidth electronic signal spectrum. The tuning range is 28.5 nm (from 980 to 950 nm). In this device, the tuning range is limited mainly by the coupled-cavity design of the tunable VCSEL. If a larger tuning range is required, a different optical cavity design, such as an air-coupled cavity [19;64], has to be used, in which case the detector won't function as a laser to enable simple integration. However, no matter how efficient the photodiode is, one photon can only generate one electron-hole pair. If the input signal is weak, extra electronic amplification will then be necessary and a heterojunction bipolar phototransistor may be a good candidate.

6.2.3 Parameter extraction of phototransistor

Heterojunction bipolar phototransistors (HPT) have been widely investigated over the past twenty years for varying photodetection applications[65]. Two-terminal HPTs have demonstrated satisfactory performance in amplification and sensitivity, however, compared to avalanche photodiodes (APDs), HPTs are not as good in terms of sensitivity[66]. Also, the high speed performance of two-terminal HPTs varies according to the input optical power intensity, which makes it less attractive for optical communications. However, in the fields of optoelectronic integrated circuit (OEIC) [67-69], biochip[70], sensing [71]and spectroscopy [72], HPTs still find a wide range of application. With the incorporation of a resonant cavity, the functionality of HPTs can be enhanced due to added wavelength selectivity [29]. In order to make HPTs more practical for general detection use, the non-constant current-gain characteristic must be fully understood and modeled. In this section, we formulate the optical gain and current characteristics, which can then be adapted for various levels of illumination. Previously Chand [73] did a similar analysis, which covers the higher illumination range very well. On the other hand, the constant gain region observed under low illumination, which is an important operating region for optical receivers, has not been addressed. There are numerous experimental results under the low illumination, but without quantitative formulation [74-76]. We have developed a model based on the floating-base-configuration and excellent agreement is obtained for both our devices and published measurements referred above.

The current components of a Npn HPT are shown in Figure 6.6. Light is incident from the collector side and is absorbed in the reverse-biased base-collector region. The photo-generated electron-hole pairs are separated by the external electrical field inside the base-collector region. Because of the floating base, the external base current, I_B , component is zero. We can then write down the following equations:

$$\begin{aligned} I_c &= I_{nc} + I_{gc} \\ I_e &= I_{ne} + I_{pe} + I_{re} \\ I_{gc} &= I_{pe} + I_{re} + I_{br} \end{aligned} \tag{6-5}$$

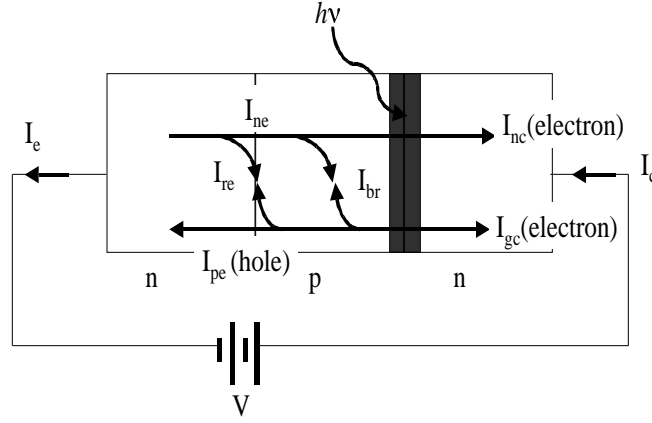


Fig. 6.6: Schematic diagram of a heterojunction phototransistor. The input photon and current components are also depicted. The shaded region is the quantum well absorbing region.

where I_c is the collector current, I_e is the emitter current, and I_{gc} is the photo-generated current. I_{re} is the recombination current in the emitter-base depletion region, and I_{br} is the recombination current in the neutral base region. I_{ne} and I_{pe} are the component electron and hole currents in the emitter and base junction, respectively. For a heterojunction device, we can write the ratio of I_{ne} to I_{pe} :

$$\frac{I_{ne}}{I_{pe}} = A = \frac{D_n L_p N_d}{D_p L_n N_a} \frac{m_{np}^* m_{pp}^*}{m_{nN}^* m_{pN}^*}^{3/2} \times \exp \frac{E_{gN} - E_{gp}}{kT} \gg 1 \quad (6-6)$$

Since the base is floating, the collector and emitter currents must be equal. I_{br} is negligible in modern narrow-base HPTs. Hence the generated photocurrent, I_{gc} , will be equal to $(I_c + A \times I_{re})$ so that the optical gain of the HPT can be defined as the following:

$$\frac{I_c}{I_{gc}} = \frac{I_c \times (A + 1)}{I_c + A \times I_{re}} = \frac{I_e \times (A + 1)}{I_e + A \times I_{re}} = \frac{(I_{ne} + I_{pe} + I_{re}) \times (A + 1)}{I_{ne} + I_{pe} + I_{re} \times (A + 1)} \quad (6-7)$$

In resonant cavity devices, the generated photocurrent, I_{gc} can be related to the incident power through the following: (assuming every absorbed photon generates one electron-hole pair) [29]:

$$\frac{P_{absorbed}}{P_{incident}} = \eta = \frac{(1 + R_2 e^{-\alpha d})}{1 - 2\sqrt{R_1 R_2} e^{-\alpha d} \cos(2\beta L + \varphi_1 + \varphi_2) + R_1 R_2 e^{-2\alpha d}} \times (1 - R_1)(1 - e^{-\alpha d}) \quad (6-8)$$

where R_1 , R_2 are the reflectivity for top and bottom mirrors in the device, α is the absorption coefficient of the quantum wells, d is the total thickness of the quantum wells, L is the cavity length, φ_1 and φ_2 are the phase added by top and bottom mirrors respectively and β is the propagation constant. Using the quantum efficiency of the device, η and the incident power intensity, we can derive the generated current from the equation (6-9):

$$I_{gc} = \text{Resp} \times \eta \times P_{incident} \quad (6-9)$$

where the Resp is the responsivity at that wavelength.

Considering the thermionic emission and generation-recombination equations in standard p-n junctions, one can postulate that $I_{np} + I_{ne} = I_f = I_{f0}(e^{qV_{BE}/kT} - 1)$ and $I_{re} = I_{r0}(e^{qV_{BE}/nkT} - 1)$ where n is the diode ideality factor in the emitter-base junction. The factor n is nominally between 1 and 2 for homojunctions but can be larger than 2 in a heterojunction [77]. I_{r0} will be slightly dependent on V_{BE} via depletion width modulation, which can be taken into account if a term $\sqrt{V_{bi} - V_{BE}}$ is included where V_{bi} is the built-in potential. Using this formula, one can immediately identify three regions of operation:

- (a) when the illumination is low, V_{BE} is small, $qV_{BE} \ll kT$, thus expanding the exponential gives: $I_f = I_{f0} \times qV_{BE}/kT$, and $I_{re} = I_{r0} \times qV_{BE}/nkT$. Substituting these two expressions into equation (6-7):

$$\frac{I_c}{I_{gc}} = \frac{(I_f + I_{re}) \times (A + 1)}{I_f + I_{re} \times (A + 1)} = \frac{(I_{f0} \frac{qV_{BE}}{kT} + I_{r0} \frac{qV_{BE}}{nkT})(A + 1)}{I_{f0} \frac{qV_{BE}}{kT} + (A + 1) \times I_{r0} \frac{qV_{BE}}{nkT}} = \frac{(I_{f0} + \frac{I_{r0}}{n})(A + 1)}{I_{f0} + \frac{(A + 1)}{n} I_{r0}} \quad (6-10)$$

Equation (6-10) will have a constant value, independent of the magnitude of collector current, I_c , flowing through the device in this low illumination regime.

(b) when illumination is in the intermediate regime, $I_f > I_{re}$, but $I_f < A \times I_{re}$, then

$$\frac{I_c}{I_{gc}} = \frac{(A+1)I_f}{AI_{re}} = \frac{I_{f0}}{I_{r0}} \times \left(e^{\frac{qV_{BE}}{kT} \left(1 - \frac{1}{n}\right)} - 1 \right) \quad I_c^{(1-\frac{1}{n})} \quad (6-11)$$

This is the general relationship observed most often in the literature [73].

(c) when illumination is high, such that $I_f \gg A \times I_{re}$, then

$$\frac{I_c}{I_{gc}} = \frac{(A+1)I_f}{I_f} = (A+1) = h_{FE} + 1 \quad (6-12)$$

Usually HPTs seldom operate in this region. Because I_{pe} will dominate the current, the ratio of I_{ne} to I_{pe} is actually the maximum current gain of the device. These three operating regimes have been described qualitatively elsewhere [76]. With the above formulation, we can fit the actual data and extract the diode ideality factor and I_{f0} , I_{r0} . [65].

A small signal model can be deduced directly from the AC current components in equation (1). If the intensity of the incident light is modulated with a small AC variation, the potential across the emitter-base junction will change correspondingly. If the small signal components are denoted as lower case variables, we can write the following expressions (the variation of I_{r0} can be neglected to first order):

$$\begin{aligned} i_c &= I_{C,total} - I_{C,DC} = I_{f0} \left(e^{\frac{q(V_{BE} + v_{be})}{kT}} - e^{\frac{qV_{BE}}{kT}} \right) + I_{r0} \left(e^{\frac{q(V_{BE} + v_{be})}{nkT}} - e^{\frac{qV_{BE}}{nkT}} \right) \\ &= I_{f0} e^{\frac{qV_{BE}}{kT}} \left(e^{\frac{qv_{be}}{kT}} - 1 \right) + I_{r0} e^{\frac{qV_{BE}}{nkT}} \left(e^{\frac{qv_{be}}{nkT}} - 1 \right) \\ &\quad (I_f + I_{f0}) \times \frac{qV_{be}}{kT} + (I_{re} + I_{r0}) \times \frac{qV_{be}}{nkT} \end{aligned} \quad (6-13)$$

Similarly,

$$i_{gc} = (I_f + I_{f0}) \times \frac{qV_{be}}{kT} + (I_{re} + I_{r0}) \times \frac{qV_{be}}{nkT} \times (A+1) \quad (6-14)$$

$$h_{fe} = \frac{i_c}{i_{gc}} = \frac{I_f + I_{f0} + \frac{(I_{re} + I_{r0})}{n} (A + 1)}{I_f + I_{f0} + \frac{(I_{re} + I_{r0})}{n} (A + 1)} \quad (6-15)$$

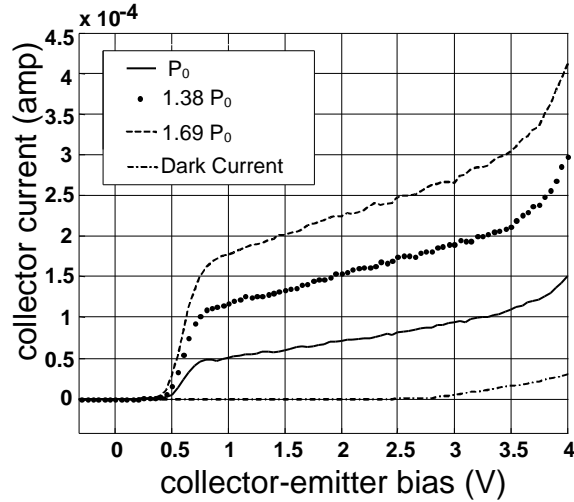


Fig. 6.7: The collector current vs. V_{CE} of a phototransistor.

Figure 6.7 shows typical I-V characteristics of our resonant cavity HPT devices with various incident optical powers. The resonant cavity HPT was originally designed for tunable devices. The detailed structure and fabrication can be found elsewhere[33]. The solid line in Figure 6.8 shows the DC gain and the dashed line gives the AC gain fitted by this model. The scattering of the data at lower collector currents is likely caused by a larger measurement error for the weak signal since our laser source is not well power stabilized. A second reason is because the dark current is of the same order of magnitude as the photogenerated current. The values of I_{f0} and I_{r0} determined from this model are 3.0628×10^{-9} and 7.812×10^{-9} Amp, respectively. The diode ideality factor, n , is 2. The lowest incident optical power the device can detect is 15 nW. Figure 6.9 shows the fit using our model to data extracted from other paper[74;76]. Excellent agreement in fitting similar data to devices fabricated by other groups and of different dimensions suggests that our model is widely applicable to describe the current gain as a function of optical power in HPTs.

To sum up, we have developed a simple, yet powerful model for HPT devices. This model can be used to evaluate the parameters, such as ideality factor, I_{f0} and I_{r0} in phototransistors. The excellent agreement between our model and experimental results of several groups demonstrates the accuracy and generality of our theory. This theory is

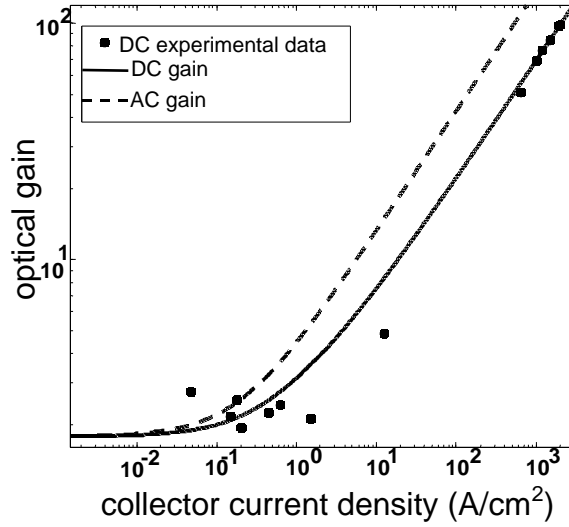


Fig. 6.8: The measured and fitted AC and DC optical gain vs. J_C plot.

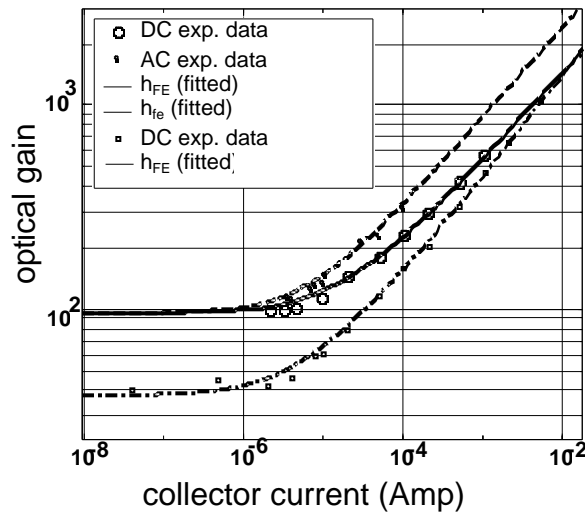


Fig. 6.9: The fitting curves with experimental results of other research group.

very helpful when we need to determine the operating point of the device and the expected operating optical gain.

6.2.4 Tunable phototransistor

From the previous section, we see that the phototransistor can provide electronic gain to the photodetection process. Although the gain is related to the input signal power, this feature can be exploited for fabricating tunable devices. Since the optical field can be smaller than a generic PIN diode, we can design this device possessing a cavity formed by an air gap between the top structure and bottom substrate [58]. The resulting design is as follows: the top mirror consists of λ_0 GaAs, $0.674 \lambda_0$ Si₃N₄, and 1500Å gold. The bottom mirror is 9.5 pairs of n-doped AlAs/GaAs DBR. The absorbing region is formed by two 80Å In_{0.24}Ga_{0.78}As/GaAs quantum wells. The emitter-base junction is graded from Al_{0.3}Ga_{0.7}As to GaAs. The graded region can distribute the bandgap change at the junction between the conduction and the valence band edges and increase the difference of the transportation between two carriers (electrons and holes) and lower the contact resistance. The whole transistor is a N⁺-p⁺-n⁻ type, and only two terminals, emitter and collector require electrical contacts. The air gap is 10,500Å thick and the design of this device is an air-coupled cavity configuration, where the air gap forms the main cavity and the semiconductor layers are treated as DBR mirror pairs [19].

The mechanical design of the device is the same as the tunable VCSEL/PIN diode mentioned before. With bias, an electric field builds up between top membrane and substrate, the resonant cavity length can be reduced by pulling the top mirror towards the bottom substrate. Photons are absorbed by the InGaAs quantum wells and the generated electron-hole pairs are detected by current through the electrodes. The spectral response is shown in Fig. 6.10. The tuning characteristics are shown in Fig. 6.11. The linewidth of the device is generally very wide due to the extra absorption of free carriers and the low finesse resonant cavity. The tuning range is 25.5 nm (from 926.5 nm to 952 nm). The measured DC gain, β , is above 100 if the input power is high. The high-speed performance of this tunable phototransistor is poor because of the large Base-Collector

junction area. This can be alleviated by fabricating a base electrode or extra mesa etch of the devices to increase the frequency modulation efficiency.

6.3 OXIDE TOP MIRROR TUNABLE DEVICES

Although the prior dielectric mirror pairs serve the tunable purpose fine, there is still room for improvement. One of the problems in dielectric mirror fabrication is that

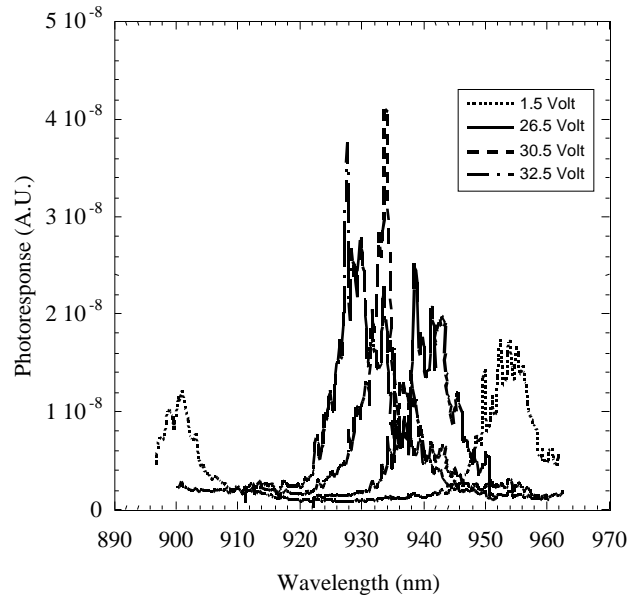


Fig. 6.10: The tuning spectral response of photocurrent of tunable HPT.

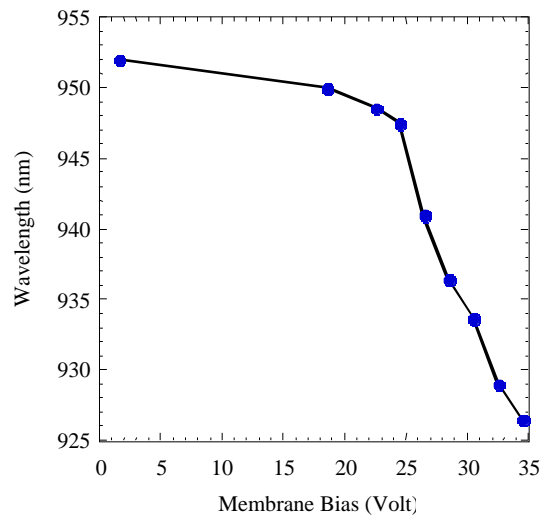


Fig. 6.11: The resonant wavelength vs. membrane tuning voltage of the

tunable HPT.

the deposition rate of PECVD system is relatively unpredictable. Thus matching the quarter wavelength requirement is not an easy task. Another more detrimental factor for the structure is that the silicon dioxide is compressive while the silicon nitride is tensile. There are several ways to release the overhanging structure including chemical wet etching, dry etching, or critical point drying (CPD). The dry release steps may produce a better yield, but usually wet etching is the easiest one in terms of fabrication. Since we need the supporting legs to survive the wet-etch releasing step, the structure has to be under tensile-strain to overcome the pulling force from the surface tension of water. The stress-matching between silicon dioxide and silicon nitride is not trivial because the compressive stress of silicon dioxide can easily suppress the tensile stress of silicon nitride if the PECVD conditions are poor. It is difficult to control the stiffness or even release rate in the resulting structure. These difficulties bring the need for a semiconductor top mirror approach in which it is easy to control the optical thickness and stress because the layers are grown by MBE. The best candidate is using $\text{Al}_2\text{O}_3/\text{GaAs}$ as the DBR pairs where the Al_2O_3 is formed by wet oxidation of AlGaAs MBE grown layers [53]. This combination provides a comparable refractive index contrast to the dielectric material while the growth is monolithic and the volume shrinkage of the AlGaAs from oxidation is predictable. In the following sections, we demonstrate a tunable filter using the $\text{Al}_2\text{O}_3/\text{GaAs}$ DBR pairs.

6.3.1 Wavelength tunable filter using $\text{Al}_2\text{O}_3/\text{GaAs}$ DBR as top mirror

Wavelength tunable filters are very important components in DWDM systems. Filters are used to separate different wavelength channels of signal and transmit them to broadband photodetectors. With increasing data and communication traffic, more channels are necessary to accommodate this need. The linewidth of each channel must then be narrower due to the limited total available optical fiber bandwidth. The oxide / semiconductor mirror approach provides a much higher reflectivity than the traditional all-semiconductor DBR. In addition, the fabrication processes are less tedious than the dielectric mirror stack approach.

The ultimate design of the tunable filters is based upon the previous discussion of mechanical response and optical diffraction loss. The flatter the central plate, the less the optical diffraction loss. To make the central plate flat and also less stiff, the redundant parts of DBR layers have to be etched away from the supporting legs. The resultant design can be seen in Fig. 6.12. There are 23 pairs of AlAs/GaAs bottom DBR of

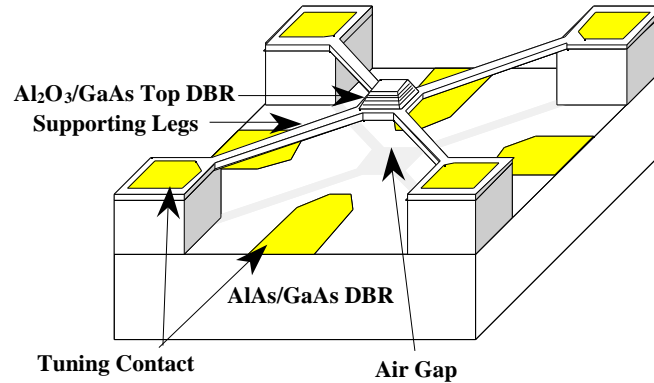


Fig. 6.12: Schematic diagram of tunable filter with $\text{Al}_2\text{O}_3/\text{GaAs}$ top mirror

thickness $801\text{\AA}/670\text{\AA}$ and 3 pairs of $\text{Al}_{0.97}\text{Ga}_{0.03}\text{As}/\text{GaAs}$ of thickness $1756\text{\AA}/670\text{\AA}$. The top $\text{Al}_{0.97}\text{Ga}_{0.03}\text{As}$ layers will later be oxidized to form the top oxide/semiconductor DBR in this device. The air gap of the filter is 9800\AA long, and forms the main resonant cavity. The device is designed to operate in the 950 nm range. After the device is finished processing, mechanical and optical measurements are made to characterize the devices. These measurements are discussed in the next two sections.

6.3.2 Mechanical Measurement

The mechanical measurements of these tunable structures concentrate on two aspects: first, the surface profile of the top membrane under electrostatic actuation; second, displacement of the top membrane versus applied voltage to identify the effective spring constant. These measurements provide a comparison between different top structure designs. The mechanical analysis of membrane deformation is first compared to experimental results. Fig. 6.13(a) shows the surface profile extracted from Dehe, et al. [23]. The membrane itself possesses a large central plate with short supporting legs. Although this geometry might be expected to exceed the limitations of our approach, in

fact, the curve is still fitted with reasonable accuracy. The second case comes from our own devices [60]. This micromachined structure has thinner supporting legs and a thicker center, due to the addition of a distributed Bragg reflector (DBR). Using the area moment method described in section 3.5.4. The thickness of the beam can also be taken into account through the moment of inertia term ($I_z = bh^3/12$). The membrane profile was

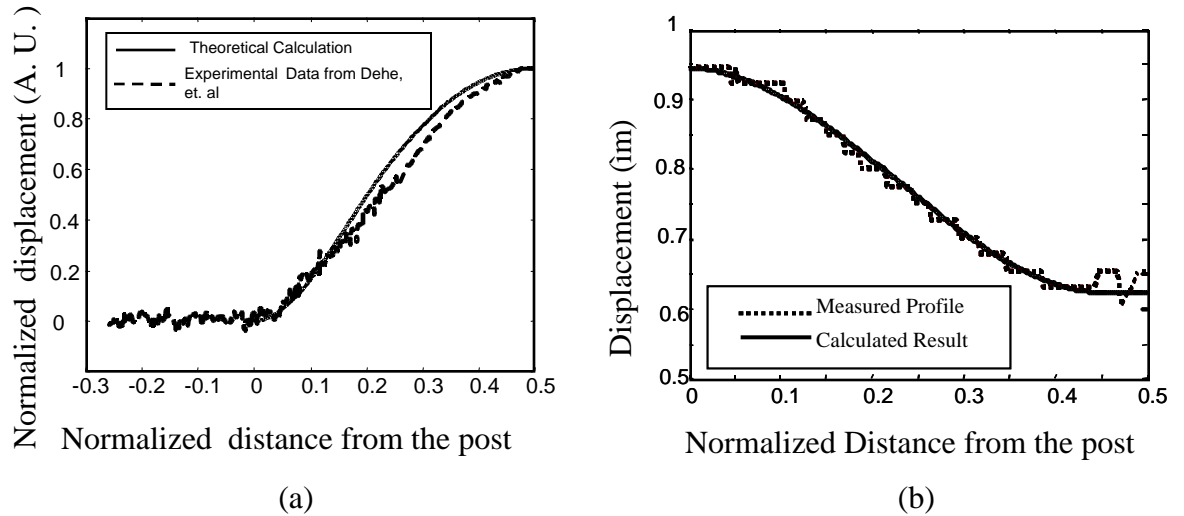


Fig. 6.13: The comparison between the area moment method calculation and the mechanical deformation profile measurement.

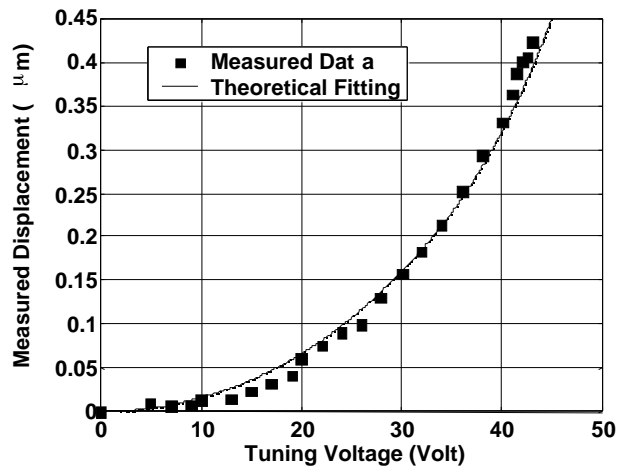


Fig. 6.14: The one dimensional model and the measured displacement vs. tuning voltage.

measured using a Zygo NewView 5000 interferometer system. This interferometer system measures the amplitude and phase of reflected white light from the device surface and calculates the profile of the device based on this information. The vertical resolution of the measurement is 0.1 nm while the lateral resolution is objective lens dependent, but 0.64 μm is the minimum. The measurable reflectivity of the surface is from 4% to 100%. The whole station is vibration-isolated. Fig. 6.13(b) shows both the simulated curve and

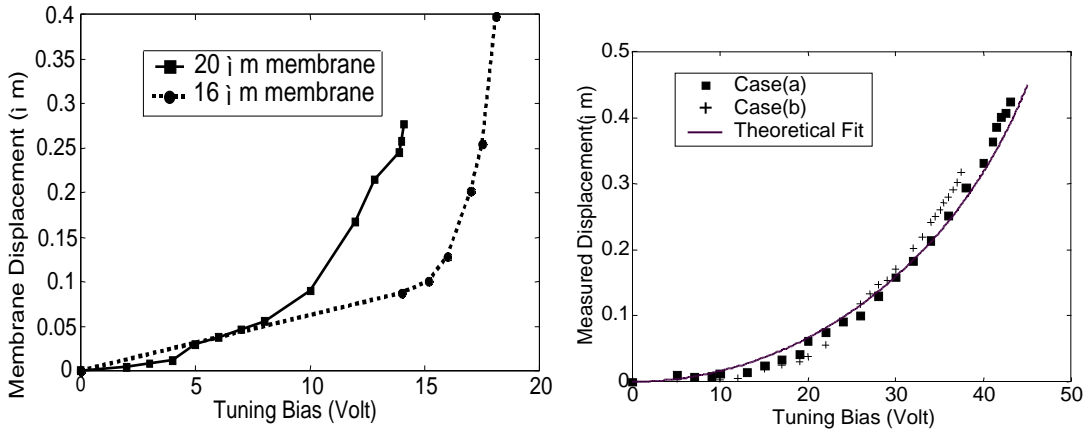


Fig. 6.15: The effect of different size of DBR: (a) the uniform thickness in everywhere of the structure; (b) the central plate thicker than the leg due to DBR. The dimension of the supporting leg is 120 μm by 5 μm .

measured data (the DBR thickness has been subtracted). The theoretical calculation has already taken into account the thickness of the DBR region. Note that the central part is flat during actuation. We observe a near-perfect match between theory and experiment.

Next, we measure displacement versus applied voltage to find the effective spring constant. Fig. 6.14 shows both the measured data and calculated result. The fit demonstrates very good description of the system using one-dimensional Hooke's law. The spring constant is 14.881 N/m and the corresponding nitride stress is 250 MPa. The top membrane design is also an important processing issue. From the previous discussion, we believed that extra internal stress could result from two sources: one from the junction between the plate and supporting legs, and the other from the pure bending of the uncovered area of the base plate. If only considering from the plate theory, we think the larger DBR covering the whole GaAs base plate provides less internal stress and thus is a better choice. However, this theory can not rule out the possibility of having extra internal stress from the junction of the structure with different thickness. From the

experimental results, we can observe which factor dominates the existing structure. In Fig. 6.15(a), the displacement versus tuning voltage of the two membranes with uniform thickness demonstrates that the larger the central area, the larger the displacement under the same tuning voltage. This is supported by the theory discussed in Chapter 3. In equation (3.4), the electrostatic force is proportional to the area of the central plate in the first order: $F = ku \frac{A\epsilon_0 V^2}{2(g_0 - u)^2}$ A , where A is the area of the central plate and u is the

displacement. So the larger the area is , the larger the force is and so is the displacement. However, in Fig. 6.15(b), we can clearly observe a significant abnormality between the two membranes with different DBR sizes. Case (a) is a tunable structure with 30 _m diameter GaAs base plate and 20 _m diameter DBR while case(b) is 20 _m diameter for both DBR and base plate. The larger central area does not display a larger displacement due to the extra internal stress caused by the partially covered DBR structure.

Another special feature of this device is the ability to adjust the tuning characteristics. Because the topmost layer of the deformable membrane is tensile silicon nitride, it is possible to dry-etch some part of this layer after release. Fig. 6.16 demonstrates this phenomenon by comparing two tuning voltage vs. displacement results on the same device. We can clearly observe that after a 10 minutes etch, a device with greater tunable range and lower tuning voltage is produced. The significance of this arrangement is that we can intentionally deposit a thicker silicon nitride film to improve the wet-releasing steps due to larger tensile stress. Afterward, we can put the device back into a dry-etching chamber to adjust the stiffness of the structure.

While we have demonstrated this general approach, this process still needs to be calibrated. According to the equation (3.5), the effective spring constant, k_{eff} , should be proportional to the thickness of the silicon nitride

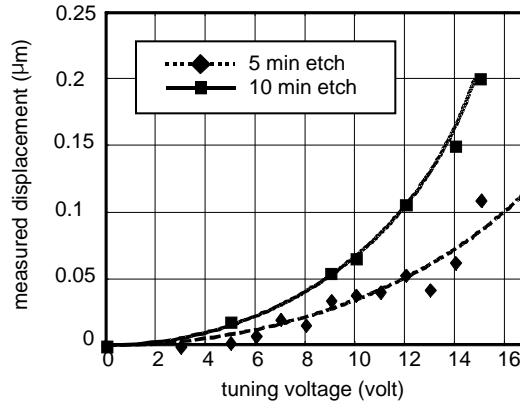


Fig. 6.16: The displacement vs. tuning voltage after different etching time of silicon nitride. The solid and dash lines are from one-dimensional theory.

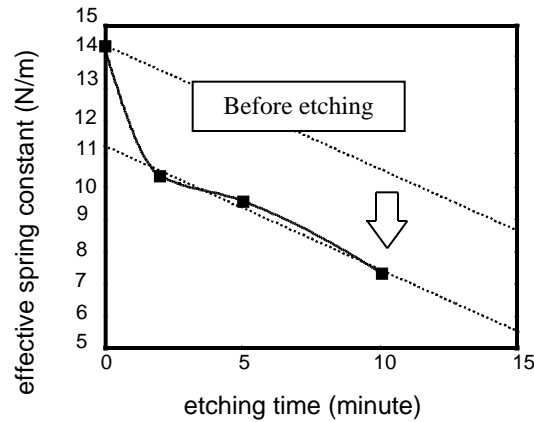


Fig. 6.17: Measured spring constant versus etching time. The dash lines are the linear extrapolation of the data points. A downshift of the linear extrapolation shows possible nitride damage during the etch.

($k_{\text{eff}} = N_{l_b_h} / l$). Thus if the etch rate of the silicon nitride is constant, the spring constant will decrease proportionally to the etching time. Fig. 6.17 shows the measured spring constants vs. etching time. From this plot, we can clearly observe a strong nonlinearity in the data at the very beginning of the etching. Possible explanations of this situation can be reasoned as follows [78]: (a) the plasma damage to the bonding of the silicon nitride material, or (b) direct ion bombardment during the dry etch. The plasma damage can produce dangling silicon bonds throughout the bulk material and reduce

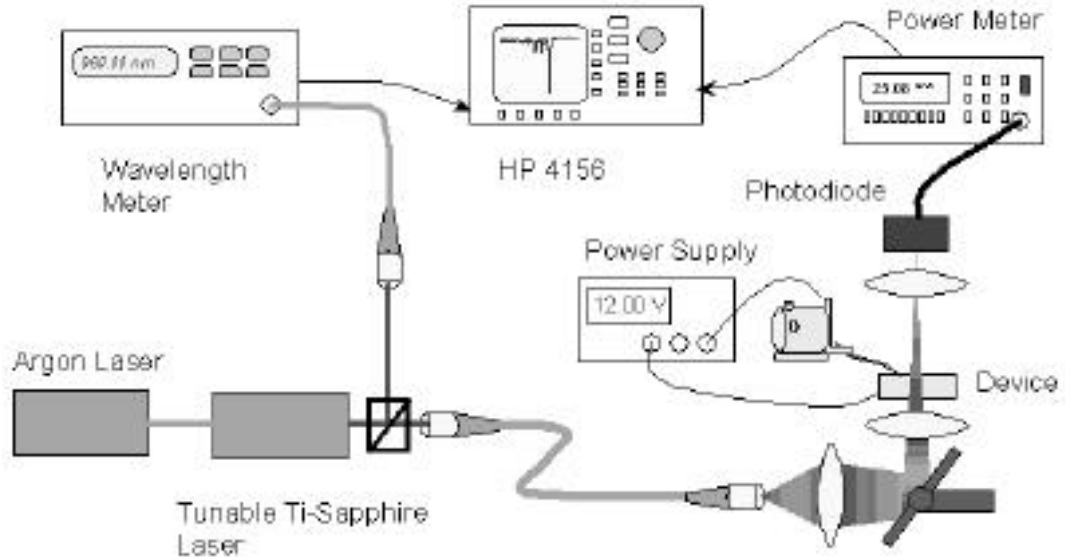


Fig. 6.18: The experimental setup of the optical measurement.

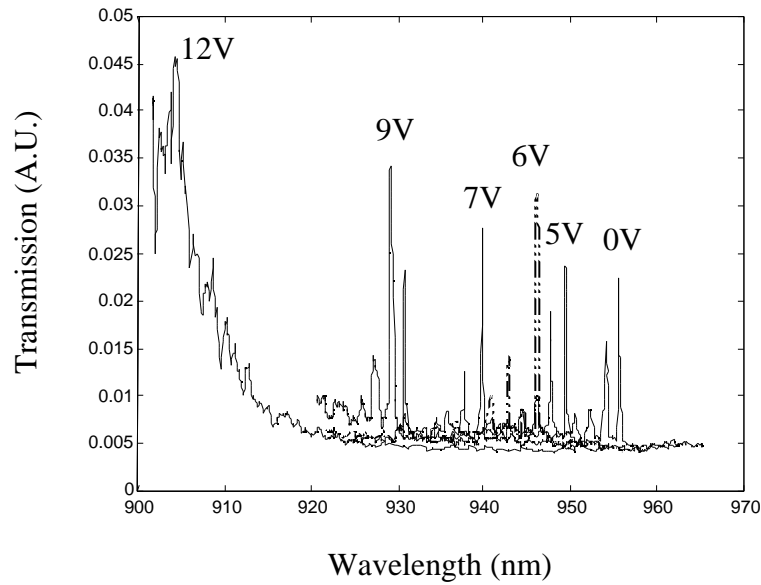


Fig. 6.19: The measured tuning spectrum of the 30 mm by 30 mm device for 10 minutes Si_3N_4 etching. Multiple peaks due to the backside reflection can be clearly observed. The last measurement (12V) possesses the largest linewidth because of the worse DBR reflectivity in that wavelength range.

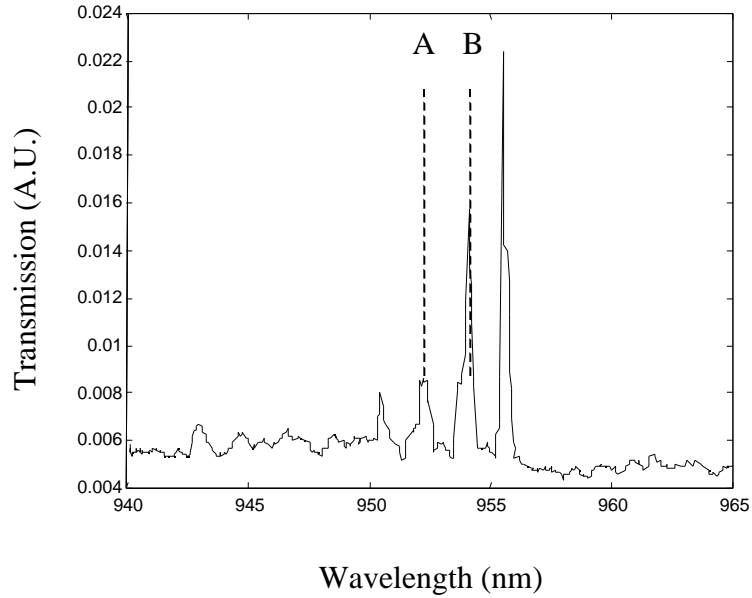


Fig. 6.20: A detailed spectrum for a tunable filter. One can observe the periodicity of the multiple peaks.

the tensile stress of the nitride directly; second, the damaged surface caused by ion bombardment will form a compressive, porous silicon oxynitride after exposing to the air.

6.3.3 Optical Measurement

After fabrication, the device is optically measured. We use an Argon laser pumping a tunable Ti-sapphire laser which is fiber-coupled to the device and wavelength meter. The light travels through a focusing microscope objective and reflecting mirrors to reach the backside of the wafer. The device is DC-biased by micromanipulator probes with proper grounding. The transmitted laser beam is then detected with a calibrated Si photodetector. Fig. 6.18 shows the general setup of the measurements. The output of an Advantest wavelength meter and Newport photodetector are fed into a HP4156 semiconductor parameter analyzer. The final spectrum of the transmission is displayed by the HP4156. Fig. 6.19 shows a typical transmission spectrum of a device with a $30 \times 30 \mu\text{m}$ top membrane. The linewidth of the spectrum is less than 1 nm across most of the tuning range. From Fig. 6.20, a detailed spectrum is shown and the distance between multiple peaks is constant. Changing from wavelength to frequency, we find that the f

between peaks is 4.98×10^{11} Hz. Considering the general etalon effect, we find out there is an etalon around 100 μm range existing inside the system. The best conclusion we can draw is thus: multiple peaks are due to some backside reflection, a result of a poor AR coating. This imperfection couples the whole GaAs substrate (around 500 μm) into the original vertical cavity and introduces more reflection peaks than we expected.

Another important feature of this device is that, as mentioned previously, the tuning characteristics of the device can be adjusted by etching away the tensile nitride layer. From the optical transmission measurements, we also observe that the same voltage swing produces different tuning ranges. Comparing the transmission data for 0-7 V bias with different etching time, we find the tuning range increasing from 6.8 nm, 10.3 nm, 14.4 nm, to 15.67 nm for the sample as grown, etched for 2 minutes, 5 minutes, and 10 minutes, respectively. To maximize this improvement, we etch samples for a total of 10 minutes and take the final measurements. We did try to remove more silicon nitride by etching the sample for 12 minutes. However, this resulted in failed devices. Most of the membranes collapse after this longer etching process, which suggests the nitride damage hypothesis for the nonlinear decrease of the effective spring constants at the beginning of the etch. Fig. 6.21 is a plot of resonant wavelength vs. tuning voltage. Because the Ti-sapphire laser can only tune from 971.5 nm to 900 nm, we can not measure the resonant peak at zero bias. Within the normal operation range of the Ti-sapphire laser, the device tunes over for 64 nm (from 971 nm to 907 nm) with 12 volts bias. Compared to similar devices in Table. 6.1, this device has much better tuning characteristics and requires lower driving force. The insertion loss of the device is measured by comparing the power

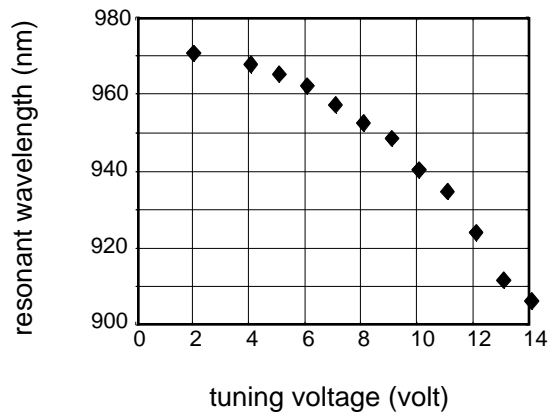


Fig. 6.21: The tuning characteristics of the 20 μ m by 20 μ m device.

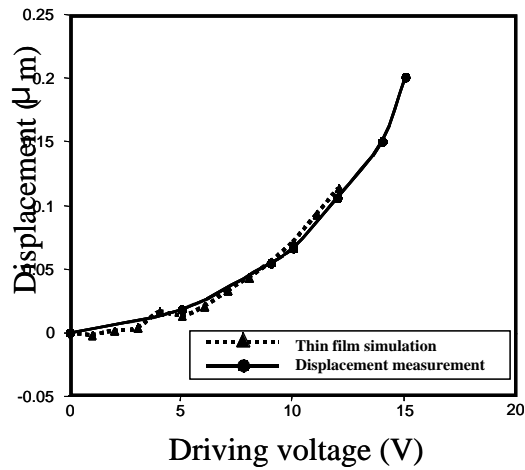


Fig. 6.22: The comparison between the optical and mechanical measurement results.

received in the photodetector with and without passing through the filter. The actual input/transmitted signal ratio is pretty poor because of the heavily doped substrate and bottom mirror and the difference is 12.1dB. After correcting for free carrier absorption in the substrate and bottom mirror and the diffraction of the laser beam, we find the insertion loss of the device to be 1.8 dB. Such a correction is reasonable since the device draws no DC current and a more lightly doped or thinned substrate would eliminate the free carrier loss, but not otherwise effect device performance.

6.3.4 Comparison between optical and mechanical measurement

Once the optical spectral response is measured, we can calculate the tuning curve as a function of air gap thickness using the transmission matrix method described in Chapter 4. The actual displacement versus tuning voltage can be obtained

Author	/ center	Tuning Voltage
M.C. Larson	3.47%	14
Tayebati	5.41%	13.1
This Work	6.82%	12

Table. 6.1: Comparison to other previous reports.

	good (ratio)		fair (ratio)		bad (ratio)		SUBTOTAL
Round	33	0.733333	7	0.155556	5	0.111111	45
Square	75	0.789474	11	0.115789	9	0.094737	95
Self-Align	0	0	7	0.148936	40	0.851064	47
Big Square	22	0.488889	6	0.133333	17	0.377778	45
TOTAL	130	0.560345	31	0.133621	71	0.306034	232

Table 6.2: The yield chart of the tunable filter with different top mirror shape.

from the Zygo NewView 5000 measurement. We can then compare these two sets of data for the same device to examine the correctness of our simulation software. In Fig. 6.22, we demonstrate both data sets versus tuning voltage. As we observe, the two sets match each other quite well. This agreement validates a number of assumptions in the calculation, which were used in the projected tuning range and VCSEL parameter extraction theory.

6.3.5 Yield of the process

The yield of the whole process including the 10 minutes of etching, is comparably high according to Table. 6.2. The number of good devices for both the circular and square shaped membranes can reach as high as 75-78%. The large square membranes (30 μ m \times 30 μ m) are more difficult to make because the release etch time takes longer and this causes more undercut in the posts region. Larger undercut in the posts make the structure easier to collapse. The success rate for these larger membranes is around 50% as shown in the table. The self-aligned pattern did not generate any good devices because of a design flaw in the mask, such that the bottom contact metal covered part of the central plate and made the releasing-etch step impossible. From the statistics, the general

releasing-etch step is very robust compared to our previous design due to the larger tensile stress developed in the structure.

6.4 SUMMARY

In this chapter, we discussed the results of both dielectric and oxide top DBR structures that have been successfully applied to wavelength tunable optoelectronic devices. The dielectric material approach was our first generation structure and utilized for a wide range of applications, such as, VCSEL parameter extraction, integrated laser/PIN devices and filters. However, the newly developed oxide-semiconductor DBR devices exhibit better performance in both mechanical and optical parameters. The semiconductor-oxide tunable filter tunes over a greater range with a lower tuning voltage swing than previously reported [5;7;79]. Also the linewidth is kept narrow across the tuning range. These special features demonstrate that the oxide-semiconductor DBR is a very attractive approach for a variety of tunable devices that will be utilized in future WDM communications systems.

Chapter 7 Future work and summary

7.1 FUTURE WORK

Surface micromachined tunable optoelectronic devices have demonstrated excellent properties that make them candidates to enhance the architectures and performance of future WDM communications systems. This thesis has focused on two areas: (1) developing a sounder scientific understanding and modeling of tunable optoelectronic devices and (2) implementation of the $\text{Al}_2\text{O}_3/\text{GaAs}$ materials system membrane for the top mirror. Using the mature dielectric top mirror structure, several models were developed and verified for these devices. Using these models, a new oxide-semiconductor mirror technology was successfully developed and applied to a tunable filter design. In the future, research on this topic will become more and more important because of the increasing demands on bandwidth and transmission speed. Several questions and problems should be investigated to improve device performance and achieve systems level acceptance:

1. *Reliability of the tunable structure*: The movable membrane has not been tested for the number of actuation cycles that might occur in the lifetime of an optical system. Whether this structure can sustain millions of tuning cycles is still unknown. For a reliable communication component and systems level acceptance, this lifetime test is very crucial.
2. *Oxide mirror lifetime*: Besides the mechanical properties of the microstructure, the lifetime of the $\text{Al}_2\text{O}_3/\text{GaAs}$ DBR is another issue. The interface between oxide and semiconductor might introduce defects and strain in the whole DBR stack. These defects and strain could degrade the DBR slowly, causing layer peeling-off or a change in the optical thickness. This will require long term testing as well as suitable accelerated aging protocols.
3. *2-D array fabrication of the tunable devices*: One of the benefits that vertical cavity devices bring is the potential for two-dimensional integration of devices on the same chip. This allows convenient on-wafer testing and a more compact fiber coupling design scheme. The layout of the array of the tunable

devices has to be reconfigured. Another issue is the electrical contact of the tuning electrodes. Because of the non-planarity of these devices, wire-bonding is the easiest way to connect an array of tunable devices using standard electronic packaging. However, vibration of the bonding action might cause damage to the overhanging membranes. Research has to be done to examine the influence on the whole performance of the system. An alternate means of making electrical contacts to these devices is to planarize the whole device structure to avoid wire-bonding. This method is better than the previous one in terms of shock to the device. However, far more process integration is needed to be able to planarize these devices without affecting the tunable membranes.

4. *Packaging device arrays*: The final goal of fabricating tunable optoelectronic devices is to produce a completed device with readily available plastic or ceramic cases. The packaging problem is one of the biggest problems for all optoelectronic devices.
5. *Refinement of optical transmission measurement*: A better measurement setup for measuring the transmission spectra of tunable filters is important to fully characterize these devices. The laser beam size can be reduced further to decrease diffraction loss. The transmitted light should be collected by a fiber close to the surface to increase the signal level. The fluctuation in laser output power also causes problems during measurement. Using a solid-state diode pumped laser can solve this problem. Another approach is to use a broadband light source, such as a white light source or LED, to measure the device performance.

After these issues are solved, we can integrate the oxide mirror technology into the full range of active devices, such as tunable VCSELs, detectors or LEDs. Because of the potential two oxidation procedures, more process integration must be considered.

The working wavelength is another major challenge for tunable devices. Due to prior processing limitations of InP based vs. GaAs based devices, almost all research has focused on GaAs based devices working in the 950 nm range. Since GaAs and Al₂O₃ are transparent at 1.55 μm, a GaAs based filter design can be easily extended to that range easily. However, a tunable VCSEL covering the longer wavelength communications band

must have quantum well material which will provide optical gain in this region. Fortunately, a new material, GaInNAs, possesses a very close-matched lattice constant to GaAs and already shown promising VCSELs at 1.3 μm [80] and edge emitting lasers at 1.5 μm [81]. Using this GaNAs/GaInNAs as the quantum well material, the other semiconductor layers in the tunable devices can be kept identical to those for the tunable 950 nm devices (only the thickness has to be changed) and longer wavelength tunable lasers can be achieved. The metro area network will need 1.3 μm lasers for future deployment and the surface micromachined tunable VCSELs developed at 950 nm in this thesis can be extended to 1.3 μm to provide an excellent candidate for a cheap, agile and integrated system.

7.2 SUMMARY

Surface micromachined technology has been very successful in integrating traditional optical components, such as mirrors and lenses, with novel optoelectronic devices. This technology enables a greater range of device designs, but increases the fabrication difficulties. The improvement of yield and ease of fabrication are very crucial topics in addition to enhancing the performance of integrated optoelectronic devices. In addition to performance enhancements, movable components in the device structure bring possibilities for determining some important device parameters that were originally difficult to measure. In this thesis, we first utilized the original dielectric top mirror design of the tunable VCSELs and phototransistors to investigate the internal operating parameters of these semiconductor devices. These parameters, such as internal quantum efficiency of VCSELs and characteristic forward/reverse biased current density of phototransistors, are very important to understand device operation. The traps or defects of the materials can often be detected by these measurements. The tunable scheme that is provided by the movable component gave a non-intrusive and also easy characterization approach during the measurement. The idea of using the same device to finish this kind of measurement is not only unprecedented, but also easy to implement.

On the other hand, the dielectric top mirror tunable devices are difficult to make due to complicated fabrication processes. Difficult processes always mean lower yield and poor performance of the tunable devices. $\text{Al}_2\text{O}_3/\text{GaAs}$ materials systems have thus

been introduced for better top mirror performance. From previously reported work [7;79], we found that the mechanical design of movable components greatly affected the tuning voltage and deformation of devices. However, little analysis had been done on this specific issue. I first proposed the area moment method as an efficient approach to estimate the deformation of the central membrane. The internal stress of different top structures was also analyzed by generalized plate theory. From these calculations, a thicker central plate with four thinner supporting legs was suggested to achieve lower tuning voltages and minimum central plate deformation. Experimental measurements verified our concerns about the structural design. The extra diffraction loss caused by the mechanical deformation of the central membrane was also discussed in this thesis. The Fox-Li model with second order perturbation correction was applied to the tunable cavity structure to give a good understanding of optical diffraction loss. It is the first time that mechanical and optical theories have been combined to evaluate a MEMS optoelectronic device.

In addition to the above theoretical work, a new integration process was introduced for the new $\text{Al}_2\text{O}_3/\text{GaAs}$ materials systems. A special arrangement of top layers of metal and tensile-stressed silicon nitride enables us to adjust the tuning voltage characteristics of tunable structures even after the release etching. However, the partially-removed silicon nitride exhibits the non-linear phenomenon of tuning voltage reduction due to extra damage caused by the RIE etching process. The adjustable feature, nevertheless, enhances the yield of tunable devices by intentionally increasing the initial tension of the structure to survive through a wet release etch.

Then the $\text{Al}_2\text{O}_3/\text{GaAs}$ top DBR is successfully combined with a bottom AlAs/GaAs DBR mirror to produce a high-performance tunable filter. This tunable filter demonstrated a 64 nm wide tuning range with a very narrow linewidth. A low actuation voltage is recorded and the flatness of the central plate is guaranteed by the surface profile measurement. The match between the experimental and theoretical results demonstrates the effectiveness of our model.

To summarize, I discussed a wide range of applications of surface micromachined technology on wavelength tunable optoelectronic devices in this thesis. I successfully incorporated a new material system into the existing structure and the device application

is also shown. Further research on these surface micromachined tunable devices, such as packaging, dynamic measurement and communication band light emission, will be expected to become very active in the future. Surface micromachined wavelength tunable devices will play an important role in future DWDM communications systems.

Appendix A Detailed Process Flow

Basic Process:

Photolithography:

1. Spray 3612 Photoresist on the wafer
2. Spin the wafer in 3000 rpm for 40 seconds
3. Wipe the photoresist in the backside of the wafer
4. Bake the wafer on the hotplate for 10 minutes under 85 °C.
5. Expose for 22 seconds on OAI aligner for edge-beak removal.
6. Use KarlSuss MA-6 mask aligner to align the wafer and expose at 2 seconds.
7. Develop the exposed photoresist in LDD26W for 2 minutes.
8. Bake the wafer on the hotplate for 10 minutes under 85 °C.

Drytek RIE chamber O₂ plasma photoresist strip:

Pressure: 150 mtorr

RF Power: 100 Watts

Gas: O₂ 20sccm, Argon.

Drytek RIE chamber Silicon nitride etch:

Pressure: 150 mtorr

RF power: 20 Watts

Gas: SF₆, Argon.

PlasmaQuest anisotropic etch:

Chamber Pressure: 5 mtorr

Gas: Argon: 75 sccm, BCl₃: 50 sccm, Cl₂: 5 sccm.

Chuck temperature: 20 °C.

ECR power: 400 Watts.

RF power: 50 Watts

STS tensile silicon nitride deposition:

Chamber pressure: 550 mtorr

Base pressure : 12 mtorr

Gas: SiH₄: 2000 sccm, NH₃: 35 sccm

APC automatic

Process temperature:350 °C

High-Frequency RF: Match load 35%, tune: 60% Automatic matching,

Process power 11 Watts.

Wafer layer structure: (for Al₂O₃/GaAs top mirror tunable filters)

All thickness in Å

GaAs 717.007 ← repeat for
Al_{0.97}Ga_{0.03}As 1741.9 ← 3 times

Al_{0.97}Ga_{0.03}As 3483.9

GaAs 97.37 (Doped with Be: $1.1 \times 10^{19} \text{ cm}^{-3}$)

GaAs 570.1

GaAs 670.1

GaAs 670.1

GaAs 9

Al_{0.85}Ga_{0.15}As 9800.0

GaAs 100.0

GaAs 570.1

GaAs 670.1

GaAs 9

GaAs 673.1 ← repeat for 13

AlAs 805.2 ← times

GaAs 703.605 ← repeat for

AlAs 841.26 ← 10 times

GaAs substrate

Doped with Si : $0.7 \text{ to } 4 \times 10^{18} \text{ cm}^{-3}$

Process flow:

1. Central mask:
 - a. pattern the wafer using 3612 photoresist
 - b. use H_2SO_4 : H_2O_2 : H_2O =1:8:40 etch down to $\text{Al}_{0.97}\text{Ga}_{0.03}\text{As}$ layer
 - c. use HCl : H_2O =1:10 selective etch to remove the remaining $\text{Al}_{0.97}\text{Ga}_{0.03}\text{As}$
 - d. Oxidize @ 440 °C (H_2O vapour @ 95 °C/ N_2 mixture) flow rate: 5 L/min
2. MembraneD mask
 - a. Evaporate 1000 Å Au and 250 Å Ti
 - b. Lift-off the metal in acetone solvent.
 - c. High tensile silicon nitride deposition in STS PECVD
3. MembraneL mask
 - a. Remove the unwanted silicon nitride using Drytek
 - b. PlasmaQuest dry etch to expose $\text{Al}_{0.85}\text{Ga}_{0.15}\text{As}$
4. Contact mask
 - a. HCl : H_2O =1:1 recess etch to remove the $\text{Al}_{0.85}\text{Ga}_{0.15}\text{As}$ in the n-contact region
 - b. Lift off the metal in acetone solvent.
5. Top contact mask
 - a. Drytek RIE etch for silicon nitride to open a contact window.
 - b. Remove the photoresist.
6. Preetch2 mask
 - a. use H_2SO_4 : H_2O_2 : H_2O =1:8:40 etch the trench around the supporting posts.
7. Undercut mask
 - a. Encapsulate the overhanging structure with photoresist.
 - b. Release the membrane using HCl : H_2O =2:1.
 - c. Remove the photoresist using Drytek RIE etch.

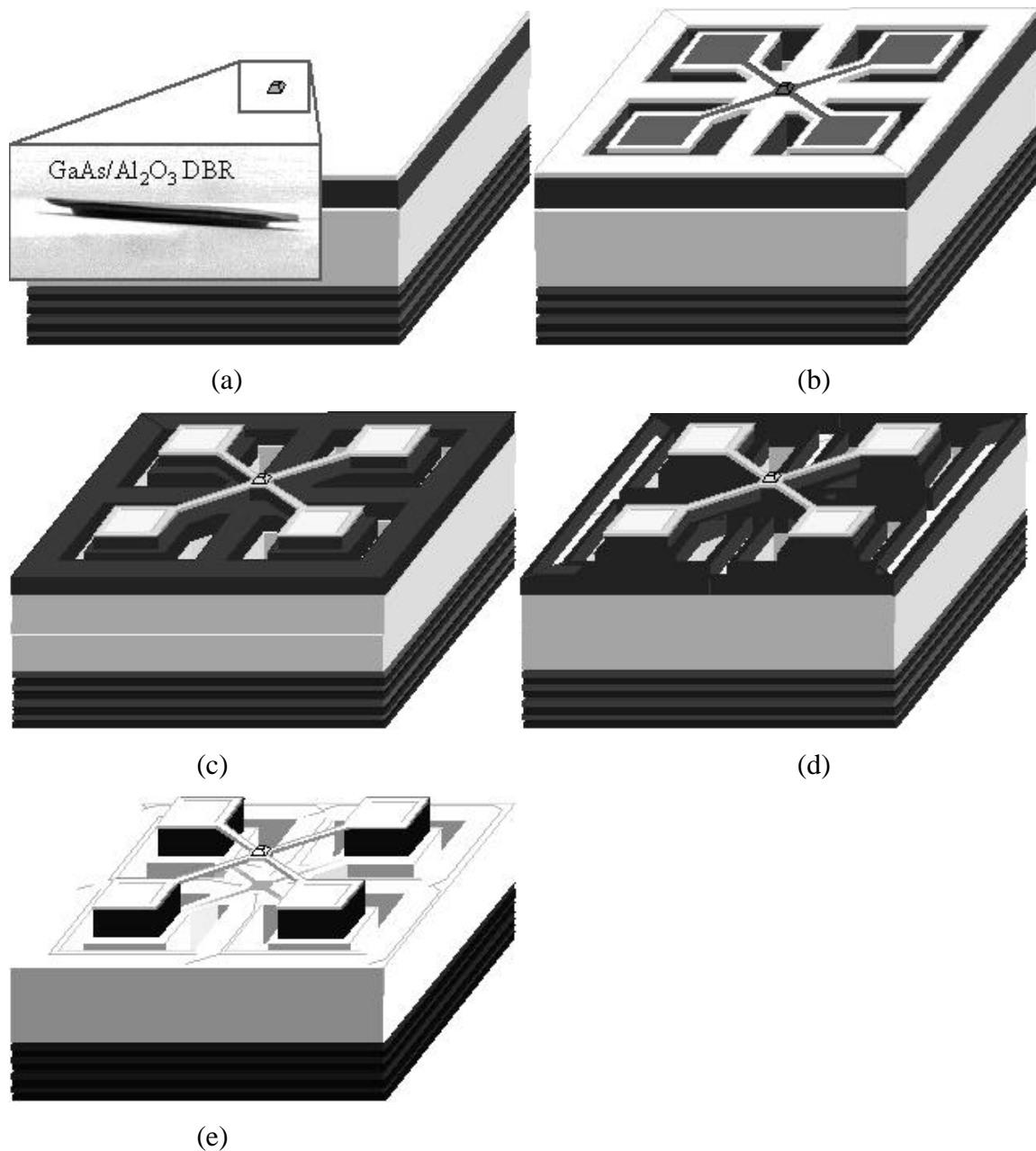


Fig. A-1: The process flow of the tunable devices: (a) After Central mask, the blow up is the SEM image (b) Deposit the silicon nitride and use MembraneL to pattern it (c) Use MembraneL to partially remove the Al_{0.85}Ga_{0.15}As (d) Use Contact mask and evaporate metal for bottom contact (e) Final release of the device.

Bibliography

- [1] Dan Sadot and Efraim Boimovich, "Tunable optical filters for dense WDM networks," *IEEE Communications Magazine*, vol. 36, no. 12, pp. 50-55, 1998.
- [2] J.Y.Liu and K.M.Johnson. "Analog smectic C* ferroelectric liquid crystal Fabry Perot optical tunable filter". *IEEE Photonics Technology Letters*, vol. 7, no. 11, pp. 1309-1311. 1995.
- [3] J.Stone and L.W.Stulz. "Pigtailed high finesse tunable FP interferometer with large, medium, and small FSR". *Electronics Letters*, vol. 23, no. 15, pp. 781-783. 1987.
- [4] J.Peerlings, A.Dehe, A.Vogt, M.Tilsch, C.Hebeler, F.Langenhan, P.Meissner, and H.L.Hartnagel, "Long Resonator Micromachined Tunable GaAs-AlAs Fabry-Perot Filter," *IEEE Photonics Technology Letters*, vol. 9, no. 9, pp. 1235-1237, 1997.
- [5] M.C.Larson, B.Pezeshki, and J.S.Harris, Jr., "Vertical coupled-cavity microinterferometer on GaAs with deformable- membrane top mirror," *IEEE Photonics Technology Letters*, vol. 7, no. 4, pp. 382-384, 1995.
- [6] E.C.Vail, M.S.Wu, G.S.Li, L.Eng, and C.J.Chang-Hasnain, "GaAs micromachined widely tunable Fabry-Perot filters," *Electronics Letters*, vol. 31, no. 3, pp. 228-229, 1995.
- [7] P.Tayebati, P.D.Wang, D.Vakhshoori, and R.N.Sacks, "Widely tunable Fabry-Perot filter using Ga(Al)As-AlO_x deformable mirrors," *IEEE Photonics Technology Letters*, vol. 10, no. 3, pp. 394-396, 1998.
- [8] S.E.Harris and R.W.Wallace, "Acousto-Optic tunable filter," *Journal of The Optical Society of America*, vol. 59, no. 6, pp. 744-747, 1969.
- [9] H.Herrmann, K.Schafer, and W.Sohler. "Polarization Independent, integrated optical, acoustically tunable wavelength filters/switches with tapered acoustical directional coupler". *IEEE Photonics Technology Letters*, vol. 6, no. 11, pp. 1335-1337. 1994.
- [10] David A.Smith, Rohini S.Chakravarthy, Zhuoyu Bao, Jane E.Baran, Janet L.Jackel, Antonio d'Alessandro, Daniel J.Fritz, S.H.Huang, X.Y.Zou, S.-M.Hwang, Alan E.Willner, and Kathryn D.Li, "Evolution of the Acousto-Optic wavelength routing switch," *IEEE Journal of Lightwave Technology*, vol. 14, no. 6, pp. 1005-1019, 1996.
- [11] R.C.Alferness and R.V.Schmidt, "Tunable optical waveguide directional coupler filter," *Applied Physics Letters*, vol. 33, no. 2, pp. 161-163, 1978.

- [12] W.Warzenskyj, F.Heismann, and R.C.Alferness, "Polarization-independent electro-optically tunable narrow-band wavelength filter," *Applied Physics Letters*, vol. 53, no. 1, pp. 13-15, 1988.
- [13] B.H.Verbeek, C.H.Henry, N.A.Olsson, K.J.Orlowsky, R.F.Kazarinov, and B.H.Johnson. Integrated four-channel Mach-Zehnder Multi/Demultiplexer Fabricated with Phosphorous doped SiO₂ waveguides on Si. *IEEE Journal of Lightwave Technology* 6[6], 1011-1015. 1998.
- [14] Ed L.Wooten, Russell L.Stone, Ed W.Miles, and Eric M.Bradley, "Rapidly tunable narrowband wavelength filter using LiNbO₃ unbalanced Mach-Zehnder Interferometers," *IEEE Journal of Lightwave Technology*, vol. 14, no. 11, pp. 2530-2536, 1996.
- [15] M.Adrian Michalicek, Victor M.Bright, and John H.Comtois. Design, fabrication, modeling, and testing of a surface-micromachined micromirror device. T.E.Alberts. 57-2, 981-988. 1995. ASME International Mechanical Engineering Congress and Exposition. 1995.
- [16] M.S.Wu, E.C.Vail, G.S.Li, W.Yuen, and C.J.Chang-Hasnain, "Widely and continuously tunable micromachined resonant cavity detector with wavelength tracking," *IEEE Photonics Technology Letters*, vol. 8, no. 1, pp. 98-100, 1996.
- [17] M.C.Larson and J.S.Harris, Jr., "Wide and continuous wavelength tuning in a vertical-cavity surface-emitting laser using a micromachined deformable-membrane mirror," *Applied Physics Letters*, vol. 68, no. 7, pp. 891-893, 1996.
- [18] Edward Chan, "Characterization and modeling of electrostatically actuated polysilicon micromechanical devices." Ph. D. Stanford University, 2001.
- [19] M.C.Larson, "Microelectromechanical wavelength-tunable vertical-cavity light-emitters and lasers." Ph. D. Stanford University, 1996.
- [20] W.-H.Juan and S.W.Pang, "High-aspect-ratio Si vertical micromirror arrays for optical switching," *IEEE Journal of Microelectromechanical Systems*, vol. 7, no. 2, pp. 207-213, 1998.
- [21] K.Aratani, P.J.French, P.M.Sarro, D.Poenar, R.F.Wolffenbuttel, and S.Middelhoek, "Surface Micromachined Tunable Interferometer Array," *Sensors and Actuators A Physical*, vol. 43, no. 1-3, pp. 17-23, 1994.
- [22] Stephen Timoshenko and S.Woinowsky-Krieger, *Theory of plates and shells* New York: McGraw-Hill, 1999, pp. 1-580.
- [23] A.Dehe, J.Peerlings, J.Pfeiffer, R.Riemenschneider, A.Vogt, K.Streubel, H.Kunzel, P.Meissner, and H.L.Hartnagel, "III-V Compound semiconductor micromachined actuators for long resonator tunable Fabry-Perot detectors," *Sensors and Actuators A Physical*, vol. 68, no. 1-3, pp. 365-371, 1998.

- [24] Stephen Timoshenko, *Strength of materials, Part I: elementary theory and problems*, 3rd ed. Huntington, New York: Robert E. Krieger Publishing Company, 1958, pp. 1-442.
- [25] F.Sugihwo, M.C.Larson, and J.S.Harris, Jr., "Simultaneous optimization of membrane reflectance and tuning voltage for tunable vertical cavity lasers," *Applied Physics Letters*, vol. 72, no. 1, pp. 10-12, 1998.
- [26] L.A.Coldren and Scott W.Corzine, *Diode lasers and photonic integrated circuits*, 1st ed. New York: John Wiley & Sons, Inc., 1995, pp. 1-594.
- [27] H.Soda, K.Iga, C.Kitahara, and Y.Suematsu, "GaInAsP/InP surface emitting injection lasers," *Japanese Journal of Applied Physics*, vol. 18, no. 12, pp. 2329-2330, 1979.
- [28] B.Demeulenaere, P.Bienstman, B.Dhoedt, and R.G.Baets, "Detailed study of AlAs-oxidized Apertures in VCSEL cavities for optimized modal performance," *IEEE Journal of Quantum Electronics*, vol. 35, no. 3, pp. 358-367, 1999.
- [29] M.Selim Unlu and Samuel Strite, "Resonant cavity enhanced photonic devices," *Journal of Applied Physics*, vol. 78, no. 2, pp. 607-639, 1995.
- [30] Sadao Adachi, "Optical properties of Al_xGa_{1-x}As alloys," *Physical Review B*, vol. 38, no. 17, pp. 12345-12352, 1988.
- [31] Sadao Adachi, "GaAs, AlAs, and Al_xGa_{1-x}As: Material parameters for use in research and device applications," *Journal of Applied Physics*, vol. 58, no. 3, pp. R1-R29, 1999.
- [32] S.Gehrsitz, F.K.Reinhart, C.Gourgou, N.Herres, A.Vonlanthen, and H.Sigg, "The refractive index of Al_xGa_{1-x}As below the band gap: Accurate determination and empirical modeling," *Journal of Applied Physics*, vol. 87, no. 11, pp. 7825-7837, 2000.
- [33] Frank Stern, "Dispersion of the Index of Refraction Near the Absorption Edge of Semiconductors," *Physical Review*, vol. 133, no. 6A, pp. A1653-A1664, 1964.
- [34] L.A.Vainshtein, "Open Resonators for Lasers," *Soviet Physics JETP*, vol. 17, no. 3, pp. 709-719, 1963.
- [35] A.G.Fox and Tingye Li, "Resonant Modes in a Maser Interferometer," *The Bell System Technical Journal*, vol. 40, no. 1, pp. 453-488, 1961.
- [36] A.G.Fox and Tingye Li, "Modes in a maser interferometer with curved and tilted mirrors," *Proceedings of the IEEE*, vol. 51 pp. 80-89, 1963.
- [37] S.R.Barone, "Perturbed Open Resonators," *Applied Optics*, vol. 10, no. 4, pp. 935-938, 1971.

- [38] John L.Remo, "Second-order Perturbation Theory for Fabry-Perot Resonators," *Optics Letters*, vol. 3, no. 5, pp. 193-195, 1978.
- [39] John L.Remo, "Nonsymmetric perturbations of Fabry-Perot resonators," *Applied Optics*, vol. 22, no. 4, pp. 517-518, 1983.
- [40] John L.Remo, "Diffraction losses for symmetrically perturbed curved reflectors in open resonators," *Applied Optics*, vol. 20, no. 17, pp. 2997-3002, 1999.
- [41] Fredy Sugihwo and Chien-chung Lin. Widely tunable phototransistor. 1998.
- [42] A.Madhukar, "Far from equilibrium vapour phase growth of lattice matched III-V compound semiconductor interfaces: some basic concepts and Monte-Carlo computer simulations," *Surface Science*, vol. 132, no. 1-3, pp. 344-374, Sept.1983.
- [43] Eric C.Larkins and J.S.Harris, Jr., "Molecular beam epitaxy of high-quality GaAs and AlGaAs," in Robin F.C.Farrow (ed.) *Molecular beam epitaxy: applications to key materials* 1 ed. Park Ridge, New Jersey: Noyes Publications, 1995, pp. 114-274.
- [44] P.Enquist, G.W.Wicks, L.F.Eastman, and C.Hitzman, "Anomalous redistribution of beryllium in GaAs grown by molecular beam epitaxy," *Journal of Applied Physics*, vol. 58, no. 11, pp. 4130-4134, 1985.
- [45] Y.C.Pao, J.Franklin, and J.S.Harris, Jr., "Influence of As₄/Ga flux ratio on Be incorporation in heavily doped GaAs grown by molecular beam epitaxy," *Journal of Crystal Growth*, vol. 95 pp. 301-304, 1989.
- [46] Takeshi Tomioka, Toshio Fujii, Hideaki Ishikawa, Shigehiko Sasa, Akira Endoh, Yasuo Bamba, Kazuaki Ishii, and Yuji Kataoka, "Suppression of Beryllium Diffusion by Incorporating Indium in AlGaAs for HBT Applications using Molecular Beam Epitaxy," *Japanese Journal of Applied Physics, Part 2 (Letters)*, vol. 29, no. 5, pp. L716-L719, May1990.
- [47] Kazuhiro Mochizuki, Shigeo Goto, and Chuushiro Kusano, "(311)A substrates suppression of Be transport during GaAs molecular beam epitaxy," *Applied Physics Letters*, vol. 58, no. 25, pp. 2939-2941, June1991.
- [48] K.Bacher, B.Pezeshki, S.M.Lord, and J.S.Harris, Jr. Molecular beam epitaxy growth of vertical cavity optical devices with in situ corrections. *Applied Physics Letters* 61[12], 1387-1389. 1992.
- [49] W.Yuen, G.S.Li, K.I.Ioakimidi, and C.J.Chang-Hasnain. Location-resolvable optical monitored growth of multiple-wavelength vertical-cavity laser arrays. *Electronics Letters* 31[21], 1840-1842. 1995.

- [50] G.S.Li, W.Yuen, K.Toth, L.E.Eng, S.F.Lim, and C.J.Chang-Hasnain. Accurate molecular beam epitaxial growth of vertical-cavity surface-emitting laser using diode laser reflectometry. *IEEE Photonics Technology Letters* 7[9], 971-973. 1995.
- [51] F.Sugihwo, M.C.Larson, Chien-chung Lin, Wayne A.Martin, and J.S.Harris, Jr. 25 nm wavelength range tunable vertical cavity lasers. 108-109. 1997. IEEE. 1997 55th Annual Device Research Conference Digest.
- [52] M.C.Larson, A.R.Massengale, and J.S.Harris, Jr., "Continuously tunable micromachined vertical cavity surface emitting laser with 18nm wavelength range," *Electronics Letters*, vol. 32, no. 4, pp. 330-332, 1996.
- [53] J.M.Dallessasse, N.Holonyak, Jr., A.R.Sugg, T.A.Richard, and N.El-Zein, "Hydrolyzation oxidation of $\text{Al}_x\text{Ga}_{1-x}\text{As-AlAs-GaAs}$ quantum well heterostructures and superlattices," *Applied Physics Letters*, vol. 57, no. 26, pp. 2844-2846, 1990.
- [54] K.W.Goossen, J.A.Walker, and S.C.Arney, "Silicon modulator based on mechanically-active anti-reflection layer with 1Mbit/sec capability for fiber-in-the-loop applications," *IEEE Photonics Technology Letters*, vol. 6, no. 9, pp. 1119-1121, 2001.
- [55] M.S.Wu, E.C.Vail, G.S.Li, W.Yuen, and C.J.Chang-Hasnain, "Tunable micromachined vertical cavity surface emitting laser," *Electronics Letters*, vol. 31, no. 19, pp. 1671-1672, 1995.
- [56] Parviz Tayebati, Peidong Wang, Daryoosh Vakhshoori, Chih-Cheng Lu, Masud Azimi, and Robert N.Sacks, "Half-symmetric cavity tunable microelectromechanical VCSEL with single spatial mode," *IEEE Photonics Technology Letters*, vol. 10, no. 12, pp. 1679-1681, 1998.
- [57] F.Sugihwo, Chien-chung Lin, J.-C.Bouteiller, M.Larson, and J.S.Harris, Jr. Micromachined tunable vertical cavity lasers as wavelength selective tunable photodetectors. 561-564. 1998. IEEE. Proceedings of the IEEE Twenty-Fourth International Symposium on Compound Semiconductors.
- [58] F.Sugihwo, Chien-chung Lin, L.A.Eyres, M.M.Fejer, and J.S.Harris, Jr. Broadly-tunable narrow-linewidth micromachined laser/photodetector and phototransistor. 665-668. 2000. Technical Digest of International Electron Devices Meeting 1998.
- [59] P.Tayebati, P.Wang, M.Azimi, L.Maflah, and D.Vakhshoori, "Microelectromechanical tunable filter with stable half symmetric cavity," *Electronics Letters*, vol. 34, no. 20, pp. 1967-1968, 1998.
- [60] Chien-chung Lin, Wayne A.Martin, Edward Chan, and J.S.Harris, Jr. A New $\text{Al}_2\text{O}_3/\text{GaAs}$ deformable mirrors for tunable optoelectronic devices . A.Lee, J.Simon, N.Narayana Aluru, V.Bright, C.Cetinkaya, J.Chung, T.Hirano, T.Kenny,

- C.-J.Kim, L.Lin, T.Saif, and C.C.Wong. **2**, 431-436. 2000. New York, NY, ASME. Micro-Electro-Mechanical Systems (MEMS) 2000 in ASME International Mechanical Engineering Congress and Exposition.
- [61] Gye Mo Yang, M.H.MacDougal, V.Pudikov, and P.D.Dapkus, "Influence of mirror reflectivity on laser performance of very-low-threshold vertical-cavity surface-emitting lasers," *IEEE Photonics Technology Letters*, vol. 7, no. 11, pp. 1228-1230, 1995.
- [62] D.L.Huffaker, D.G.Deppe, K.Kumar, and T.J.Rogers, "Native-oxide defined ring contact for low threshold vertical-cavity lasers," *Applied Physics Letters*, vol. **65**, no. 1, pp. 97-99, 1994.
- [63] T.A.DeTemple and C.M.Herzinger, "On the semiconductor laser logarithmic gain-current density relation," *IEEE Journal of Quantum Electronics*, vol. **29**, no. 5, pp. 1246-1252, 1993.
- [64] F.Sugihwo, "Design and fabrication of wavelength tunable optoelectronic devices." Ph. D. Stanford University, 1998.
- [65] J.C.Campbell, "Phototransistors for lightwave communications," in W.T.Tsang (ed.) *Semiconductors and semimetals* Orlando, FL: Academic, 1985, pp. 389-447.
- [66] K.Tabatabaie-Alavi and C.G.Fonstad, Jr. Performance comparison of heterojunction phototransistors, p-i-n FET's, and APD-FET's for optical fiber communication systems. *IEEE Journal of Quantum Electronics* 17[12], 2259-2261. 1981.
- [67] Leo J.Irakliotis, Patrick J.Stanko, Carl W.Wilmsen, and Pericles A.Mitkas. Demonstration of a VCSEL-based optoelectronic look-up table. *IEEE Photonics Technology Letters* 9[4], 502-504. 1997.
- [68] Bo Lu, Ping Zhou, Yin-Chen Lu, Julian Cheng, R.E.Leibenguth, A.C.Adams, J.L.Zilko, J.C.Zolper, K.L.Lear, S.A.Chalmers, and G.A.Vawter. Reconfigurable binary optical routing switches with fan-out based on the integration of GaAs/AlGaAs surface-emitting lasers and heterojunction phototransistors. *IEEE Photonics Technology Letters* 6[2], 222-226. 1994.
- [69] J.A.Lott, Hyun-Kuk Shin, and Yong-Hee Lee. Deep red vertical cavity surface emitting lasers with monolithically integrated heterojunction phototransistors for output power control. 185-186. 1996. Piscataway, NJ, IEEE. 15th International Semiconductor Laser Conference.
- [70] T.Vo-Dinh, J.P.Alarie, N.Isola, D.Landis, A.L.Wintenberg, and M.N.Ericson. DNA biochip using a phototransistor integrated circuit. *Analytical Chemistry* 71[2], 358-363. 1999.

- [71] Eduardo Ramos, P.Parmananda, Guillermo hernandez-Cruz, and Mihir Sen. Dynamics of boiling from a short capillary tube. *Experimental Heat Transfer* 10, 273-290. 1997.
- [72] D.I.Hoult and C.M.Preston. Inexpensive plasma discharge source for molecular emission spectroscopy with application to ^{15}N analysis. *Review of Scientific Instruments* 63[3], 1927-1931. 1992.
- [73] Naresh Chand, Peter A.Houston, and Peter N.Robson. Gain of a heterojunction bipolar phototransistor. *IEEE Transactions on Electron Devices* 32[3], 622-627. 1985.
- [74] J.C.Campbell, Andrew G.Dentai, Charles A.Burrus, Jr., and John F.Ferguson. InP/InGaAs heterojunction phototransistors. *IEEE Journal of Quantum Electronics* 17[2], 264-269. 1981.
- [75] J.C.Campbell, Andrew G.Dentai, Gin-Jong Qua, and John F.Ferguson. Avalanche InP/InGaAs heterojunction phototransistor. *IEEE Journal of Quantum Electronics* 19[6], 1134-1138. 1983.
- [76] J.C.Campbell, C.A.Burrus, Andrew G.Dentai, and K.Ogawa. Small-area high-speed InP/InGaAs phototransistor. *Applied Physics Letters* 39[10], 820-821. 1981.
- [77] Sandip Tiwari and David J.Frank. Analysis of the operation of GaAlAs/GaAs HBT's. *IEEE Transactions on Electron Devices* 36[10], 2105-2121. 1989.
- [78] Y.Kuo and M.S.Crowder, "Reactive Ion Etching of PECVD n^+ a-Si:H: Plasma damage to PECVD silicon nitride film and application to thin film transistor preparation," *Journal of Electrochemical Society*, vol. 139, no. 2, pp. 548-552, Feb.1992.
- [79] P.Tayebati, P.Wang, D.Vakhshoori, and R.N.Sacks, "Microelectromechanical tunable filters with 0.47 nm linewidth and 70 nm tuning range," *Electronics Letters*, vol. 34, no. 1, pp. 76-78, 1998.
- [80] J.F.Klem, D.K.Serkland, O.Blum, K.M.Geib, A.W.Jackson, R.I.Naone, M.D.Dalberth, and J.Smith. 1.3 μm InGaAsN VCSELs on GaAs substrates. 1, 134-135. 2001. Technical Digest of the Conference on Lasers and Electro-Optics, 2001.
- [81] W.Ha, V.Gambin, M.Wistey, S.Bank, H.Yuen, S.Kim, and J.S.Harris, Jr. Long wavelength GaInNAsSb/GaNAsSb multiple quantum well lasers. *Electronics Letters* 38[6], 277-278. 2002.